

**TECHNICAL REPORT
NATICK/TR-12/011**



AD _____

NOVEL BONDING PROCESS FOR CBW PROTECTIVE ELECTROSPUN FABRIC LAMINATES PHASE II

**by
Michael A. Costolo
John D. Lennhoff
and
Jeffrey W. Bacon**

**Physical Sciences Inc.
Andover, MA 01810-1077**

December 2011

**Final Report
April 2002-January 2006**

Approved for public release; distribution is unlimited.

**Prepared for
U.S. Army Natick Soldier Research, Development and Engineering Center
Natick, Massachusetts 01760-5020**

UNCLASSIFIED

DISCLAIMERS

The findings contained in this report are not to be construed as an official Department of the Army position unless so designated by other authorized documents.

Citation of trade names in this report does not constitute an official endorsement or approval of the use of such items.

DESTRUCTION NOTICE

For Classified Documents:

Follow the procedures in DoD 5200.22-M, Industrial Security Manual, Section II-19 or DoD 5200.1-R, Information Security Program Regulation, Chapter IX.

For Unclassified/Limited Distribution Documents:

Destroy by any method that prevents disclosure of contents or reconstruction of the document.

UNCLASSIFIED

REPORT DOCUMENTATION PAGE					Form Approved OMB No. 0704-0188	
Public reporting burden for this collection of information is estimated to average 1 hour per response, including the time for reviewing instructions, searching existing data sources, gathering and maintaining the data needed, and completing and reviewing this collection of information. Send comments regarding this burden estimate or any other aspect of this collection of information, including suggestions for reducing this burden to Department of Defense, Washington Headquarters Services, Directorate for Information Operations and Reports (0704-0188), 1215 Jefferson Davis Highway, Suite 1204, Arlington, VA 22202-4302. Respondents should be aware that notwithstanding any other provision of law, no person shall be subject to any penalty for failing to comply with a collection of information if it does not display a currently valid OMB control number.						
PLEASE DO NOT RETURN YOUR FORM TO THE ABOVE ADDRESS.						
1. REPORT DATE (DD-MM-YYYY) 29-12-2011		2. REPORT TYPE Final		3. DATES COVERED (From - To) April 2002 – January 2006		
4. TITLE AND SUBTITLE NOVEL BONDING PROCESS FOR CBW PROTECTIVE ELECTROSPUN FABRIC LAMINATES—PHASE II				5a. CONTRACT NUMBER DAAD16-02-C-0033		
				5b. GRANT NUMBER		
				5c. PROGRAM ELEMENT NUMBER		
6. AUTHOR(S) Michael A. Costolo, John D. Lennhoff, and Jeffrey W. Bacon				5d. PROJECT NUMBER		
				5e. TASK NUMBER		
				5f. WORK UNIT NUMBER		
7. PERFORMING ORGANIZATION NAME(S) AND ADDRESS(ES) Physical Sciences Inc. 20 New England Business Center Andover, MA 01810-1077				8. PERFORMING ORGANIZATION REPORT NUMBER PSI-1379/TR-2057		
9. SPONSORING / MONITORING AGENCY NAME(S) AND ADDRESS(ES) U.S. Army Natick Soldier Research, Development and Engineering Center ATTN: RDNS- WSC-C (H. Schreuder-Gibson) Kansas Street, Natick, MA 01760-5020				10. SPONSOR/MONITOR'S ACRONYM(S) NSRDEC		
				11. SPONSOR/MONITOR'S REPORT NUMBER(S) NATICK/TR-12/011		
12. DISTRIBUTION / AVAILABILITY STATEMENT Approved for public release; distribution is unlimited..						
13. SUPPLEMENTARY NOTES DFARS SBIR Data Rights contained in this report (date discovery 7 April 2006) expired on 7 April 2011.						
14. ABSTRACT <i>Report developed under Small Business Innovation Research contract.</i> Electrospun membranes for CBW protective fabric were modeled, developed, and tested. Theoretical models for gas permeation, as well as filtration efficiency, were developed as functions of fiber diameter. The effects of varying the process variables on the fiber morphology were also explored. The mechanical properties of the electrospun nonwoven fabrics were tested, as well as the filtration efficiency of electrospun Estane membranes. Bead-free Estane membranes were evaluated for filtration efficiency using custom fabricated test equipment and showed filtration efficiencies in excess of 98.5% against 1 micron polystyrene-latex spheres.						
15. SUBJECT TERMS						
FIBERS	FILTRATION	TENSILE STRENGTH	NONWOVEN FIBERS			
ESTANE	SBIR REPORTS	PROTECTIVE CLOTHING	BARRIER MATERIALS			
FABRICS	LIGHTWEIGHT	MECHANICAL PROPERTIES	ADHESIVE BONDING			
TEXTILES	PERMEABILITY	ELECTROSPUN MEMBRANES				
LAMINATES	BREATHABILITY	CHEMICAL WARFARE AGENTS				
DIAMETERS	FIBER DIAMETER	BIOLOGICAL WARFARE AGENTS				
MEMBRANES	ELECTROSPINNING	SPINNING(INDUSTRIAL PROCESSES)				
16. SECURITY CLASSIFICATION OF:			17. LIMITATION OF ABSTRACT	18. NUMBER OF PAGES	19a. NAME OF RESPONSIBLE PERSON	
a. REPORT	b. ABSTRACT	c. THIS PAGE			Heidi L. Schreuder-Gibson	
U	U	U	SAR	92	19b. TELEPHONE NUMBER (include area code) 508-233-5487	

UNCLASSIFIED

This page intentionally left blank

UNCLASSIFIED

TABLE OF CONTENTS

Section	Page
1.0 Executive Summary	1
2.0 Introduction.....	2
3. Phase I Results Summary.....	2
4. Phase II Approach and Goals.....	5
5. Electrospun Estane Membranes.....	6
6. Theoretical Understanding of Non-woven Membrane Strength.....	11
6.1 Properties of Polyurethane Elastomeric Fibers.....	12
6.2 Mechanical Properties of Elastomers.....	12
6.3 Mechanical Properties of Non-Woven Fabrics.....	15
6.4 Combined Model for Elastomeric Non-Woven Fabrics	17
6.5 Experimental Results	18
6.6 Summary and Conclusions	19
7. Process Parameter Effects.....	20
7.1 Formulations	21
7.2 Multi-Nozzle Arrays	26
8. Issues Affecting Scaleup.....	40
8.1 Develop ESD-safe Syringe Pump.....	40
8.2 Optimize Electrospinning Nozzle Diameter	41
8.3 Evaluate Alternative Pumping Method.....	48
8.4 Evaluate Effect of Electrical Conductivity	50
8.5 Quantified Relationship Between Pressure, Flow Rate and Droplet Concentration	52

TABLE OF CONTENTS (Continued)

Section	Page
8.6 Produced Samples for Moisture Permeability Testing	54
8.7 Perform Mechanical Testing on Electrospun Membranes.....	63
8.8 Summary	a64
9. Gas Permeation and Particle Filtration	65
9.1 Gas Permeation	65
9.2 Filtration Model	66
9.3 Summary	75
10. Filtration Efficiency Testing	76
10.1 Experimental Apparatus.....	76
10.2 Device Operations.....	77
10.3 Filtration Efficiency Testing	80
10.4 Summary	83
11. References	83

LIST OF FIGURES

Figure		Page
1	Moisture permeability of fabric laminates	3
2	Optical image (left) and SEM (right) of patterned electrospun adhesive	4
3	Summary chart of the breathability and permeability of several fabrics tested at the U.S. Army Natick Soldier Center	4
4	Tensile strength versus % Estane 58245 in DMF	9
5	Maximum load/mass versus % Estane 58245 in DMF	9
6	Tensile strength versus relative humidity	10
7	Average fiber diameter versus % Estane 58245 in DMF	10
8	Effect of NMP on tensile strength	11
9	The calculated elastic modulus of an elastomeric fiber (Estane 58245 TPU) as a function of true strain	14
10	The calculated ratio of the fabric modulus (E_f) to the fiber modulus (E_f) for an isotropic, non-woven fabric under uniaxial tension.....	16
11	The calculated modulus as a function of strain for a non-woven elastomeric fabric under a uniaxial tensile stress	17
12	A comparison between measured and calculated stress-strain curves for a non-woven fabric synthesized at PSI by electrospinning Estane 58245 TPU	18
13	Stress Strain Plot for Estane Film (black) and Electrospun Estane	18
14	SEM Images of Electrospun Estane at 15 cm (left) and 25 cm offset	19
15	(a) Standard and (b) Parallel Plate (PP) electrospinning configurations	20
16	Photographs depicting a solidified Taylor cone formed during electrospinning.....	21
17	Division between dry and wet electrospun deposits	21
18	Applied voltage variation for a standard electrospinning system.....	22
19	Estane in various combinations of THF, NMP, and DMF	23
20	18% Estane in THF/NMP	24

LIST OF FIGURES (Continued)

Figure		Page
21	Visual confirmation of moisture in Estane pellets	24
22	SEM images at 500x for electrospun material at a flow rate of 10ml/hour	25
23	Effects of conductivity enhancement additives on an 18%Estane in a 90% DMF / 10% NMP solution.....	26
24	Deposition characteristics for conductivity modifiers	26
25	Parallel plate showing numbering sequence for multiple nozzles and geometry	27
26	Effect of (a) deposition time, (b) flow rate, and	28
27	Effect of (a) nozzle position/plate separation and of (b) nozzle position/extension on the precision of depositing the electrospun material	29
28	Voltage variation with position for a single nozzle system	30
29	Diagram used to define the overlap ratio for a two-nozzle system.....	30
30	A two-nozzle system with two dummy nozzles	31
31	Various characteristics of a two-nozzle electrospinning system	32
32	Triangular nozzle array	33
33	Top view of nozzle arrangements for (a) linear and	34
34	Various characteristics of a three-nozzle system	35
35	Capillary height vs time for 0.5 mm diameter capillary	37
36	Comparison of capillary height vs time for a 1.35 mm and 0.5 mm diameter capillary.....	38
37	Time to reach 1 cm height in a 0.5 mm ID capillary	38
38	SEM images of electrospun Estane showing effect of nozzle diameter	42
39	Relationships between nozzle, fiber and droplet diameters.....	43
40	Samples 1 through 6.....	45
41	Samples 7 through 12.....	46

LIST OF FIGURES (Continued)

Figure		Page
42	Samples 13 through 18.....	47
43	Relationships between field strength, droplet diameter, and fiber diameter.....	48
44	Low droplet concentration at very low flow rate.....	49
45	Effect of electrospinning jet initiation shape	50
46	Electrospun Estane-PANi solution	52
47	Deposition rate versus solution pressure.....	53
48	Droplet diameter versus solution pressure.....	53
49	Droplet deposition rate versus solution pressure	53
50	Tensile sample preparation	63
51	Coating tensile strength versus area density	64
52	Percent elongation of coatings versus area density.....	64
53	Ratio of effective hydrodynamic diameter to fiber diameter as a function	66
54	Diffusion coefficient as a function of particle size	68
55	Generalized comparison of the contribution to total filter efficiency due to diffusion and to interception (Ref. 2).....	69
56	E-folding penetration distances into 500 nm fiber diameter filters; 1 cm/s face velocity.....	69
57	E-folding penetration distances into 500 nm fiber fabrics; 50% fabric porosity	70
58	E-folding penetration distances in fabric; 500 nm fiber, 50% porosity	71
59	99.99% capture penetration depths; 50% porosity, 1 cm/s face velocity for varying particle diameters.....	72
60	Pressure drop across filter bed of varying fiber diameters	72
61	Energy required to transport gas across filters of varying fiber sizes: 10 cm/s velocity, 80% porosity, and 99.99% removal of 1 micron particles.....	73
62	Pressure drop across filter beds of varying fiber diameters particles	74

LIST OF FIGURES (Continued)

Figure	Page
63	Pressure drop across filter beds of varying fiber diameters74
64	Energy required to transport gas across filters of varying fiber sizes, 10 cm/s velocity, 50% porosity and 99.99% removal of 1 μm particles.....75
65	Energy required to transport gas across filters of varying fiber sizes, 100 cm/s velocity, 50% porosity and 99.99% removal of 1 μm particles.....75
66	a) Cutaway view of a Collison nebulizer from BGI, b) Schematic of apparatus.....76
67	a) Droplets per particle vs. particle dilution. b) Particles per minute vs. particle dilution78
68	Histograms of “object size” on collection filter to look for the presence of multiple particles per droplet78
69	Plot of the log of the observed particle density vs. the log of the dilution ratio showing the linear fit with slope of -1.279
70	a) Areal particle density of particles on the collection filter and b) a surface view of the Gaussian fit to the mean data80
71	Fluorescence microscope images of a) the front (incident) and b) the back of the fabric after testing81
72	a) Areal particle density of particles on the collection filter and b) a surface view of the Gaussian fit to the mean data81
73	Images of electrospun Estane films after filtration testing. a) 500x SEM image and b) 50x fluorescence microscope image82
74	Areal particle density of particles on the collection filter for the three electrospun filters tested82
75	Surface plots of Gaussian fits to the mean values for a) 5 min deposition, b) 10 min deposition, and c) 20 min deposition electrospun samples82

LIST OF TABLES

Table		Page
1	Labeling System used to Describe Experimental Results.....	21
2	Vapor Pressure of Solvents	23
3	Nozzle Gauges and Diameters	41
4	Conditions of Sample Production	41
5	Process Optimization Sample Conditions.....	44
6	Comparison of Electrical Conductivity	51
7	Description of Samples	52
8	List of Samples Prepared for Moisture Permeability Testing.....	54
9	Tensile Testing Samples	63
10	Summary of Electospun Estane Membrane Filtration Efficiency Results.....	82

1.0 Executive Summary

Executive Summary

The U.S. Army Natick Soldier Center has developed a polyurethane (PU) based electrospun nanofiber non-woven fabric that has excellent CBW barrier properties. These electrospun membranes hold promise as barrier materials for biological warfare agents and chemical aerosols, and as high surface area carriers for chemical warfare agent deactivating chemistries. Physical Sciences Inc. (PSI) has completed a Phase II SBIR program entitled “Novel Bonding Process for CBW Protective Electrospun Fabric Laminates”. During this program PSI developed a wide range of electrospinning expertise focused on the fabrication of lightweight, electrospun, Chem-Bio Warfare (CBW) barrier membrane laminate fabrics. The laminate construction includes a non-woven liner, a barrier membrane, and a fabric outer layer. An adhesive bonding layer holds the three fabrics together. Barrier membranes were electrospun from polyurethane elastomers and examined for mechanical properties, breathability, permeability, and particle filtration efficiency as a function of areal density and fiber diameter. PSI developed patterned electrospinning on an internally funded research program and applied that technology to produce a breathable adhesive layer for the CBW barrier laminate. Mathematic models of the electrospun materials were used to better understand the mechanical integrity of the membranes.

The Phase II program efforts were focused on developing components of this laminate, including:

1. An electrospun barrier membrane, made from 200 nm diameter polyurethane nanofiber, that is mechanically robust (>5 ksi). The mechanical properties will be enhanced through enhanced fiber to fiber bonding without a loss in laminate breathability.
2. A barrier membrane fabric composite assembly with permeability of 0.5 inches of water at 10 ft³/m²/minute.
3. The bonded multi-layer CBW agent barrier fabric will retain 90% of the moisture transmission of the three components (fabric, membrane, non-woven) measured without the adhesive layer addition.
4. A method to adhesively bond conventional soldier uniform fabric with an electrospun CBW barrier layer while retaining excellent fabric laminate breathability and drape, and developing a plan for the scale-up of production of the laminate fabric.
5. The adhesive layers will be tailored to fail at 90% of the tensile failure of the barrier membrane. This failure point will ensure a strong interlaminar bond, reducing the opportunity for the electrospun barrier membrane to be ruptured.
6. An electrospinning scale-up strategy and path.

This document describes the efforts associated with each element of the program plan in detail.

2.0 Introduction

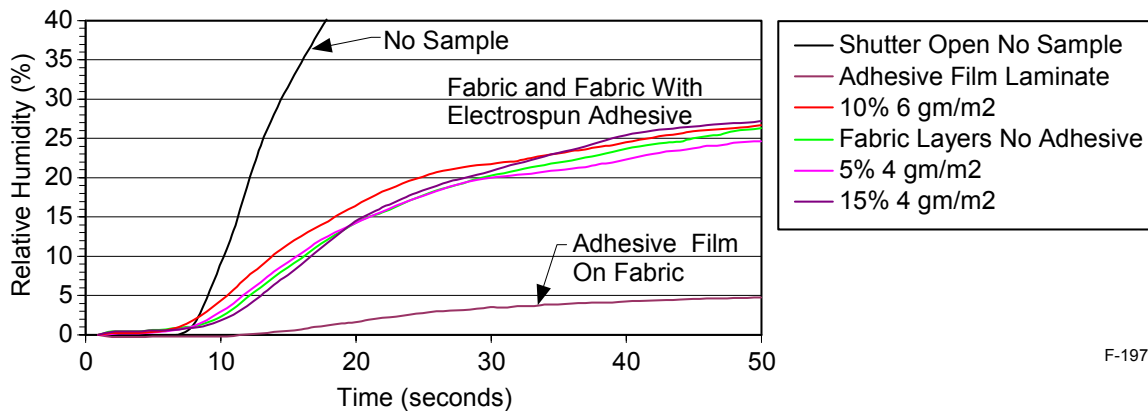
The motivation for developing new techniques of incorporating chemical and biological weapon (CBW) barriers into fabrics is to improve the breathability and drape of the fabric while maintaining or improving its CBW resistance. This affords soldiers wearing uniforms sewn from such fabric greater comfort and enables them to wear the uniforms for longer lengths of time than conventional CBW suits. These CBW barriers are incorporated as layers in a laminate structure which the layers must be held together in some way. Conventional film adhesive techniques dramatically reduce the breathability of the fabric; this program addresses that issue.

The key technology in the PSI approach is the technique used to apply the adhesive. Electrospinning is a technique whereby a polymer solution is drawn from a fine metal nozzle in a strong electric field. This technique can create very fine polymer fibers which, when used with a polymeric adhesive, creates a more breathable adhesive layer resulting in improved overall breathability in the laminate structure. PSI has adapted the electrospinning process to allow for control over the deposition area (patterned electrospinning). Additionally, PSI has developed the ability to electrospin the CBW barrier polymer directly onto fabric. This removes some complexity from the laminate and provides a filtration efficiency of >99% against 1 micron particles.

3. Phase I Results Summary

Physical Sciences Inc. (PSI) has developed a method to adhesively bond conventional soldier uniform fabric with an electrospun Chem-Bio Warfare (CBW) barrier layer while retaining excellent fabric laminate breathability and drape. The U.S. Army Natick Soldier Center has developed a polyurethane (PU) based electrospun nanofiber non-woven fabric that has excellent CBW barrier properties. These electrospun membranes hold promise as barrier materials for biological warfare agents and chemical aerosols, and as high surface area carriers for chemical warfare agent deactivating chemistries. In this effort a laminate construction of woven fabric with an electrospun PU barrier layer and a non-woven liner was studied for different adhesive bonding scenarios. When this layered structure is laminated with conventional film adhesive methods, the fabric loses breathability and is more rigid. On the completed Phase I program, PSI demonstrated the electrospun deposition of a strong, fiberized adhesive that enables the construction of a CBW laminate fabric.

In Phase I, PSI proposed to formulate a moisture cured polyurethane adhesive that could be electrospun to achieve uniform deposition over a wide area or to deposit in specific patterns. PSI would vary adhesive areal density, formulation, and fiber diameter to optimize the bond to the laminate textile while retaining fabric breathability and drape. The Phase I effort successfully demonstrated the formation of a nanofibrous adhesive bond of tunable bond strength that did not affect fabric breathability and drape. Figure 1 shows the change in Relative Humidity across a fabric laminate constructed with electrospun adhesive, film adhesive, and fabric without any adhesive. The legend lists the adhesive areal density in grams of adhesive/meter² of fabric and the solids content of the spinning solution.



F-1977

Figure 1. Moisture permeability of fabric laminates

The slope of these lines at early times in the exposure is a measure of water vapor transport rates across the membrane. The data shows no measurable decrease in the transport rate when the fiberized adhesive is used.

An optical image of the patterned electrospun adhesive on a camouflage fabric is shown in Figure 2, along with a 2000X magnification Scanning Electron Microscope (SEM) image of the nanofibers. This image demonstrates the ability to pattern the adhesive, another critical Phase I objective. The diamond pattern in the left image is 2.5 by 5 cm. spacing across. PSI has provided the electrospinning deposition of the desired Worthen Industries moisture cure PU adhesive that has:

- No detectable loss in breathability of the fabric with electrospun adhesives, both patterned and not, at areal densities to over 10 gm/m² for a range of fiber diameters,
- A trend to higher bonding strengths for patterned electrospun adhesives at the same areal density as uniform (not patterned) electrospun adhesives,
- Bond strengths for electrospun adhesive equivalent to the solid film adhesive fabric laminate,
- No detectable loss in fabric drape,
- Full curing of the isocyanate adhesive exhibited by no detectable isocyanate peak by infrared spectroscopy for the electrospun samples.
- Achieved bond cohesive failure at high areal density loadings indicating exceptional adhesive cured strength.

Figure 3 shows the results of breathability and permeability tests on PSI nonwoven fabrics along with other fabrics tested at the U.S. Army Natick Soldier Center.

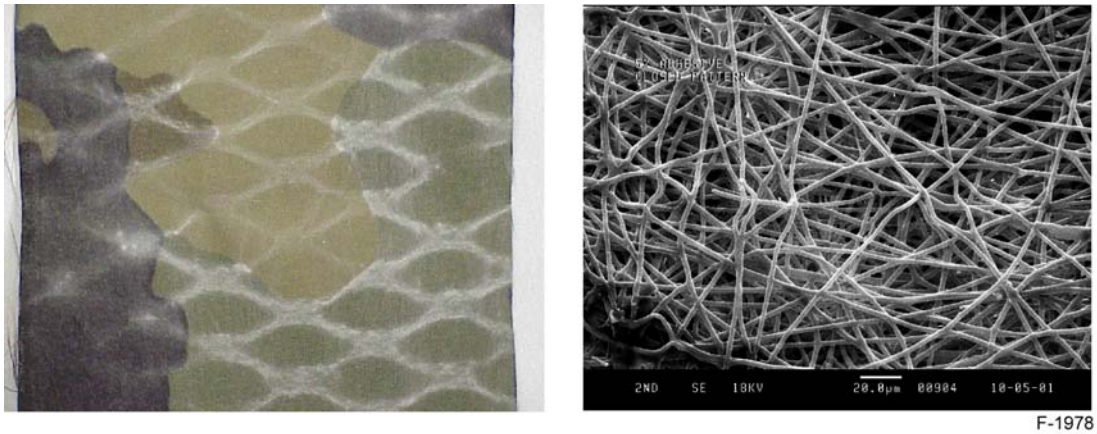


Figure 2. Optical image (left) and SEM (right) of patterned electrospun adhesive

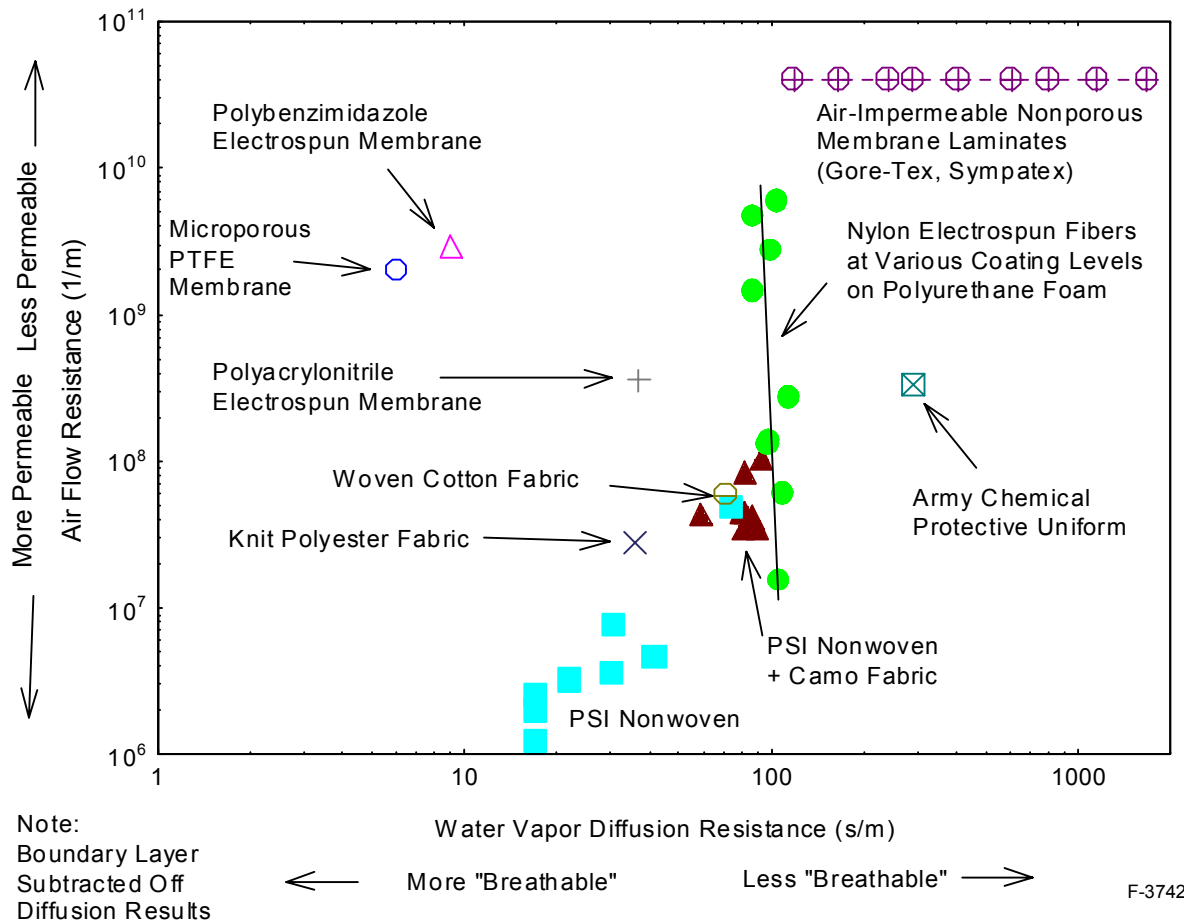


Figure 3. Summary chart of the breathability and permeability of several fabrics tested at the U.S. Army Natick Soldier Center

4. Phase II Approach and Goals

On the Phase II Program, PSI will continue to optimize and enhance the CBW barrier fabric laminate construction and scale-up the process to produce the optimized materials at enhanced rates. The major Technical Objectives of the proposed program are:

1. Enhance the tensile strength of the Natick Soldier Center PU CBW barrier membrane by an order of magnitude, while retaining 90% breathability and drape.
2. Ensure that the barrier membrane is not compromised during mechanical stress.
3. Demonstrate that the breathability and drape of the laminate textile will be maintained at 90% of the fabric value tested without the adhesive to ensure user acceptance.
4. Demonstrate the scale-up of the production of the electrospinning process by at least two orders of magnitude in deposition rate.
5. Incorporate the enhanced electrospinning production into a CBW textile pilot plant.

PSI will accomplish these objectives through the following specific means.

1. The tensile strength of the PU CBW barrier membrane will be enhanced by an order of magnitude through addition of high boiling solvent during the electrospinning fabrication and a cold rolling process step of the membrane that will enhance fiber to fiber bonding.
2. The adhesion of the PU membrane to the fabric will be tuned to fail at 90% of the membrane tear strength. This ratio will ensure that the barrier is not compromised during mechanical distortion. The adhesion will be tuned by controlling the electrospun adhesive extent of curing at the time of fabric lamination, the concentration of non-adhesive polymers, the adhesive areal density and electrospun nanofiber diameter.
3. PSI has demonstrated the breathability and drape of the laminate fabric were maintained at 90% of the fabric values tested without the adhesive on the Phase I program due to the excellent properties of the electrospun materials. These properties should be easily retained.
4. A single electrospinning nozzle typically deposits 1 gram/hour. PSI will demonstrate a production of electrospun material at 100 grams/hour using jets formed from a planar film initiated by added energy either through laser, ultrasonics or field concentration. At an adhesive areal density of 5 gm/m², this process will deposit adhesive for 20 m²/hr of textile.
5. Adapt the pilot plant technology that is being developed for electrospun reinforcement of thin space durable films for NASA.

In addition, PSI will be assisted on the proposed Phase II effort through the use of the expertise and insight of others:

- Tex-Shield, Inc. (Laurel, NJ) will assist the proposed Phase II effort to provide fabric samples, materials testing support and end user manufacture support. Tex-Shield is the

prime supplier of fabric for the Joint Service Lightweight Integrated Suit Technology (JSLIST) CBW agent protective garments.

Professor Gregory Rutledge (MIT) is a leader in modeling of the electrospinning process. Professor Rutledge will assist with the scale-up of the electrospinning process through insight gained from his modeling efforts.

5. Electrospun Estane Membranes

Estane 58245, a thermoplastic polyurethane provided by Noveon, was dissolved in dimethylformamide (DMF) solvent. Solutions of 16, 18, 20, and 22% Estane 58245 by mass were prepared. In addition, solutions of 20% Estane 58245 by mass in 75, 85, and 90% DMF relative to N-Methylpyrrolidone (NMP) were prepared. The solutions were mechanically shaken to increase the rate of dissolution until the Estane 58245 pellets were fully dissolved in solution. Each solution's density was approximated by tarring a 1-mL disposable pipette and then measuring the weight when filled with 1-mL of solution.

Each solution was pumped from a 5-mL plastic syringe, using a syringe pump, to a thin metal tube held horizontally and attached to a positive electrode lead from a current limited DC power supply. As a droplet of polymer solution formed at the tip, the voltage from the power supply was adjusted to create a Taylor cone, thereby spraying a fine polymer fiber towards a grounded aluminum weighing pan. The electrospinning was monitored until a steady jet was achieved, at which point samples were collected.

Numerous variables were monitored during each electrospun trial. There included the polymer solution flowrate (mL/h), applied voltage (kV), distance from tip to surface (cm), time spinning (min), temperature (F), percent relative humidity, and the diameter of the circular deposited membrane (cm). The above parameters were varied in order to see their effect on tensile strength and fiber diameter.

All samples were then dried in an oven with vacuum capability at approximately 135 °C and 30 in. Hg vacuum for 4 hours. Following heating, the samples were allowed to slowly cool to room temperature with the oven off and door open.

Tensile testing was performed using an Instron 4400 Series mechanical strength testing system with flat face grips. Identical strips, 1 in. x 0.38 in., were cut from the center of the membrane deposit with a razor blade and aluminum template. The strips were then mounted in the grips using tweezers. Upon failure, the following parameters were recorded: maximum displacement (mm), maximum load (N), break displacement (mm), break load (N), .2% yield strength (MPa), modulus (MPa), and energy at break (J).

In order to calculate the tensile strength for a sample, the thickness of the sample had to be known. This posed an interesting problem because the deposited membrane varied in thickness. The center was the thickest section, with the height decreasing as one progressed outward in the radial direction.

Numerous methods were employed to analyze this situation. A Dektak Bench-Top Surface Profiler was used on various regions of a sample to detect height variance, but measurements were inaccurate due to interactions of the probe tip and the fibrous material and the fact that the membrane could not be removed from the aluminum weighing pan for measurement, thereby adding in its surface variation.

Fourier transform infrared spectroscopy was also attempted, using the interferogram output from a vertically mounted membrane. The porous nature of the membrane disallowed accurate readings.

A ZYGO Phase-Measurement Interface Microscope was used to measure the surface topology. This method is still the most promising, but more measurements will be required to confirm its applicability.

Ultimately a mathematical model was created and used to calculate approximate values for tensile strength. The variation in the height was assumed to be negligible, therefore creating a cylindrical membrane-deposit shape. Thus, the underlying calculation of height was based on the volume of a cylinder:

$$h = \frac{4V}{\pi d^2}$$

where:

h = sample height
V = volume of a cylinder
d = deposited diameter

The volume was then evaluated for each sample using parameters recorded during experimentation. The equation is as follows:

$$V = \frac{Qt\rho_{\text{sol}}x}{\rho_{\text{mem}}}$$

where:

Q = solution flowrate during electrospinning
t = time electrospinning
 ρ_{sol} = solution density
x = percent Estane 58245 in solution
 ρ_{sol} = approximate fiber membrane density

The membrane density was taken as 40% of the Estane 58245 film density, which was $0.4 \times 1.21 \text{ g/cm}^3$. This porosity was estimated from the electron micrographs of the samples with a common appearance. Only samples deposited very wet deviated from this appearance. It was assumed that volume fraction porosity was independent of fiber size.

The tensile strength could then be evaluated as follows:

$$\text{TensileStrength} = \frac{F}{hw}$$

where:

F = maximum load
h = calculated height
w = width of strip = 0.38 in.

Select membrane deposits were viewed using scanning electron microscopy (SEM). At a magnification of 10,000 times, the average fiber diameter was calculated by loading the image into RF Designer and randomly measuring 15-20 fibers. At lower levels of Estane 58245 content or low flowrates, a beading effect occurred. These beads were disregarded, and only adjoining fibers were measured.

Experiments

A total of 211 samples were electrospun successfully, and from those, 149 successful tensile tests were performed. Tensile test attempts were made on all 211 electrospun samples, but some tore or folded up before mounting in the Instron grips. Based on previous research, the parameter with the most bearing on tensile strength was believed to be the dependence on the mass percent of Estane 58245 in solution. Therefore the plot of all results of tests from solutions with 100% DMF solvent is as follows, using the estimated thickness to calculate the tensile strength. These data are shown in Figure 3.

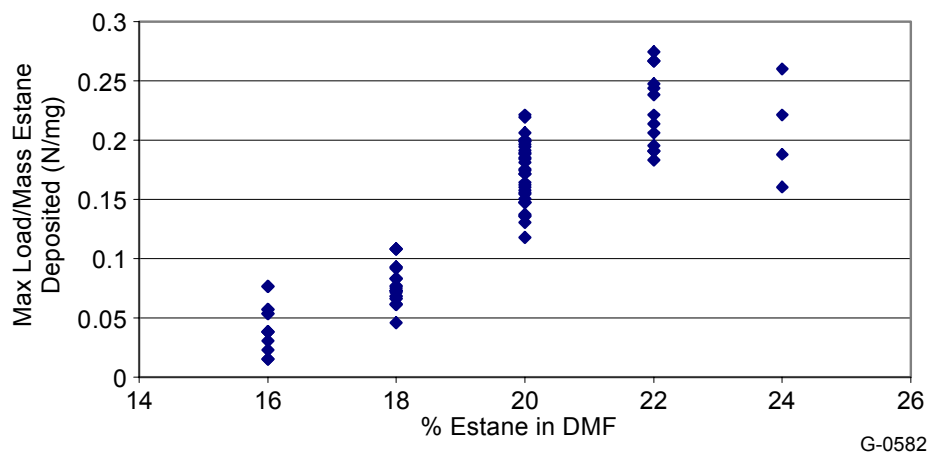


Figure 4. Tensile strength versus % Estane 58245 in DMF

In a similar manner, the data can be plotted without the use of the thickness estimate to reveal a similar trend in terms of the ratio of load over mass deposited as a function of percent Estane 58245, and are shown in Figure 4.

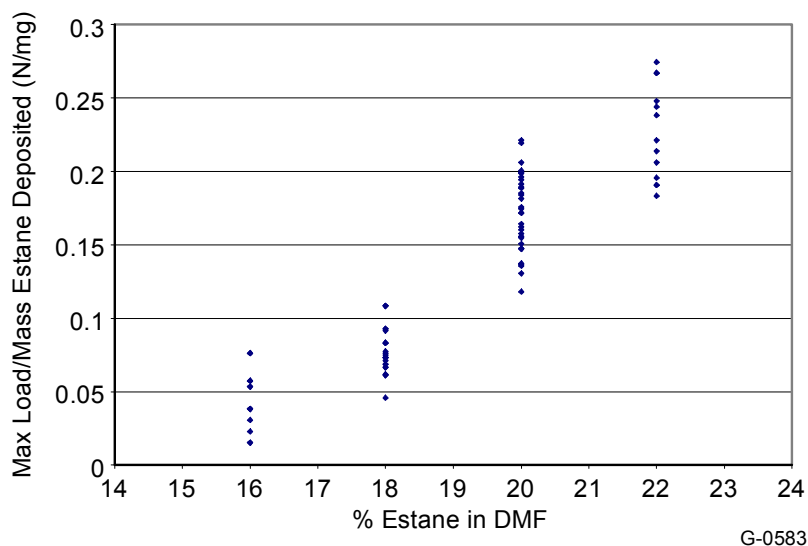


Figure 5. Maximum load/mass versus % Estane 58245 in DMF

The room relative humidity contributed to observed day-to-day variations in electrospinning and appears that it may affect the tensile strength of the membrane, potentially affecting fiber to fiber bonding. Figure 5 shows membrane tensile strength as a function of relative humidity. It is not clear why more humid days seemed to enhance mechanical properties and additional studies, in a controlled espin setup, are under way. It is expected that high humidities would encourage moisture uptake in the DMF and precipitate the Estane, reducing fiber to fiber bonding. Additional study is needed.

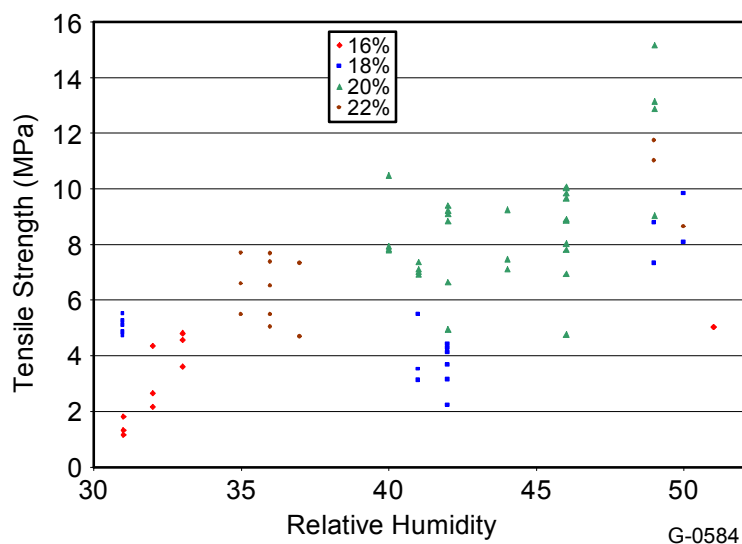


Figure 6. Tensile strength versus relative humidity

The analysis of average fiber diameter using SEM was completed on 10 samples of varying percent Estane 58245 in DMF, and is shown in Figure 6. The results show an increasing linear trend of diameter to percent polymer.

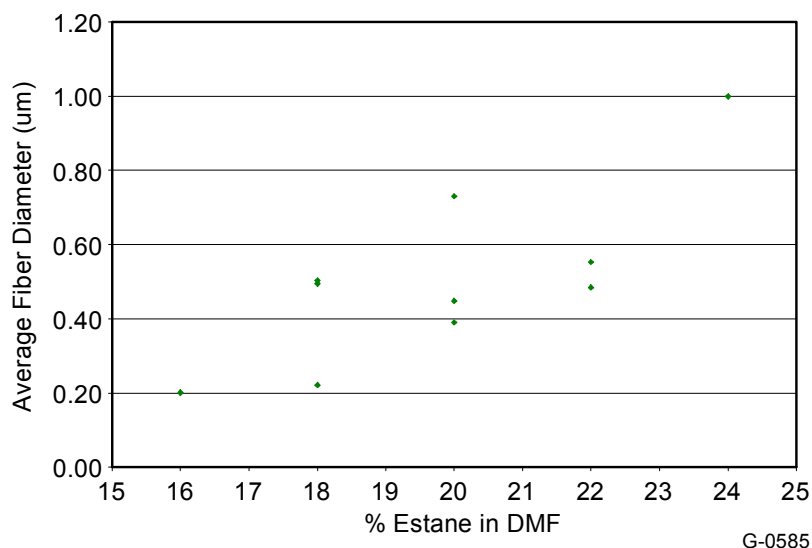


Figure 7. Average fiber diameter versus % Estane 58245 in DMF

An average of the tensile strength of 32 samples of 20% Estane 58245 in 100% DMF were compared to 11 samples in 10/90% by mass NMP/DMF, 6 samples in 15/85% by mass NMP/DMF, and 3 samples in 25/75% by mass NMP/DMF. The results from this study on NMP/DMF solvent usage are as in Figure 7. It appears that some higher boiling NMP solvent (bp203 C) added to the DMF (bp 153 C) enhanced mechanical strength of the membrane due to better fiber to fiber bonding. However excess solvent inhibits strength. SEM images of the samples may help explain the trend.

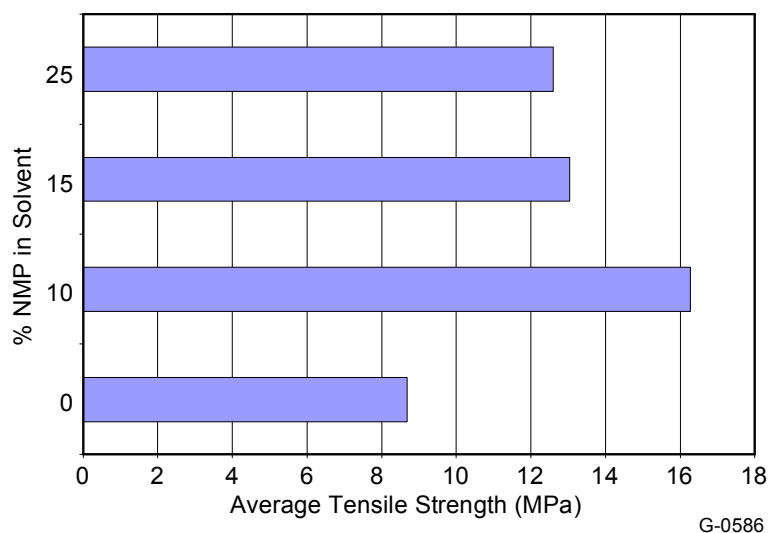


Figure 8. Effect of NMP on tensile strength

It is clear that the tensile strength of the electrospun membrane is dependant on the percent of Estane 58245 in solution. It is also evident that the average fiber diameter increases with increasing percent of Estane 58245 in solution. It appears that other variables are a factor in the overall tensile strength of the membrane, and based on the ranges studied this summer, such possible parameters may be applied voltage and relative humidity. Further investigation of the parameter space is suggested for future work.

Based on the mathematical model for calculating the tensile strength, the goal value was not attained, which was to reach 90% of the tensile strength of the Estane 58245 film. Based on the Novean specifications, that would be $0.9 \times 27.6 = 24.8$ MPa. The highest tensile strength reached out of all experimental trials was 15.2 MPa. Therefore since this goal was not achieved, the sieve diameter or breath-ability was not studied on any samples. Remember, though, that the tensile strength was based on a mathematical model for determining the height of the sample. This model could be flawed, since the surface is assumed to be flat, which is known not to be the case. A promising area for analysis of this was using the ZYGO microscope, which should be investigated further.

Finally, the study of NMP/DMF solutions may be another area to examine. It appears as though low amounts of NMP in solution increased the overall tensile strength of the membrane compared to the 100% DMF solutions that were electrospun.

6. Theoretical Understanding of Non-woven Membrane Strength

PSI is investigating the synthesis of polyurethane elastomer membrane materials via an electrospinning route. These membranes must have pore sizes $< 1 \mu\text{m}$ and retain 90% of the mechanical strength of the bulk material. While controlling the pore size of these membranes is relatively straight forward, obtaining the necessary mechanical strength has proven more difficult. The purpose of the present study is to provide an understanding for the deformation

mechanisms of elastomeric non-woven fabrics in an attempt to identify ways in which these materials may be strengthened.

6.1 Properties of Polyurethane Elastomeric Fibers

Handbook of Fiber Science and Technology: Volume III, High Technology Fibers Part A, M. Lewin and J. Preston editors, Marcel Dekker Inc, 1985, pp. 51-85.

Thermoplastic polyurethane (TPU) elastomeric fibers are widely used in the textile industry because of their rapid, forceful and nearly complete recovery upon release from large (>400%) displacements. In addition, TPU's are generally stable to 200°C for short times and have good tensile strengths. These properties stem from the block copolymer structure that is formed during the polymerization process. Polymerization of TPU's generates alternating block copolymers (A-B)_n, in which "soft" segment domains provide a coilable, alignable material that can accommodate high strains, and "hard" segment domains give long-range intermolecular attractions that provide rapid shape recovery upon release.

Soft segment domains (SSD's) in TPU's are randomly coiled aliphatic polyethers or copolyesters. The SSD phase is continuous and comprises 65-90% by weight of the fiber. In an unstressed, relaxed fiber, these coiled molecules are unoriented; however, they begin to uncoil and align as the fiber is stretched. X-ray diffraction of TPU's during deformation has shown that regions of the SSD begin to crystallize as these coiled molecules align themselves. This crystallinity stiffens and strengthens the fiber as it is being strained. When the stress is removed, the crystallites "melt" and the chains recoil with a force that is primarily due to entropy changes.

Permanent deformation due to intermolecular flow is inhibited by the hard segment domains (HSD's). The HSD's form near the end of polymerization from aromatic diisocyanates that are located in the regions between the SSD phases. HSD's are typically aromatic-aliphatic polyureas and are attached to the SSD phase by urethane linkages. The HSD's are very small, 30-100Å, and act as very effective "tie-points" to keep the SSD molecules from flowing during deformation.

The primary advantage of TPU's over natural rubbers is that the latter relies on a high concentration of cross-linking to obtain a high elasticity. The ordered, discontinuous HSD phases provide good interchain attachments that results in a higher elasticity with a lower modulus than that found in most natural rubbers. It is important to note that TPU's for applications other than fibers are commonly cross-linked to increase the modulus and the strength of the material, at a cost of reduced elasticity.

6.2 Mechanical Properties of Elastomers

L.R.G. Treloar, "Thermodynamics of Rubber Elasticity", chapter in Applied Fiber Science Volume 2, F. Happey editor, Academic Press, 1979.

F.W. Billmeyer, Textbook of Polymer Science, 3rd ed., Wiley-Interscience, 1984, pp. 308-311.

T.H. Courtney, Mechanical Behavior of Materials, McGraw-Hill, 1990, pp. 60-65.

Elastic strain of most materials is limited to a few tenths of a percent and results in the stretching of primary atom-atom bonds (one notable exception is the "superelastic" effect

observed in some shape-memory alloys that can result in recoverable displacements up to 10%). In contrast, elastomeric materials can experience recoverable strain of up to 1000%. These enormous strains are accommodated by the uncoiling and straightening of long polymeric molecules. These molecules are kept from flowing by intermolecular cross-linking or a finely dispersed second phase (i.e. HSD for TPU's). Since most of the displacement in elastomers is accommodated by chain uncoiling and not primary bond stretching, the elastic modulus for elastomers is typically several orders of magnitude lower than most inorganic materials. As the elastomer is stretched, the molecular chains align, which results in a reduction of the elastomer's entropy. This reduction in entropy is the primary cause of free energy increase for low to moderate levels of strain in elastomeric materials.

Consider the retractive force f of an elastomer that has undergone a displacement of dl . For a system free energy G :

$$f = \left(\frac{\partial G}{\partial l} \right)_{T,p} = \left(\frac{\partial H}{\partial l} \right)_{T,p} - T \left(\frac{\partial S}{\partial l} \right)_{T,p}$$

The elastomer can effectively be treated as an ideal gas, where:

$$\left(\frac{\partial U}{\partial V} \right)_T = T \left(\frac{\partial P}{\partial T} \right)_V - P$$

For an ideal gas, $PV = nRT$, $(\partial P/\partial T)_V = R/V$ and $P = RT/V$:

$$\left(\frac{\partial U}{\partial V} \right)_T = T \left(\frac{R}{V} \right) - \frac{RT}{V} = 0$$

Since $(\partial U/\partial V)_T$ for a gas is equivalent to $(\partial H/\partial l)_{T,p}$ for an ideal elastomer:

$$f = -T \left(\frac{\partial S}{\partial l} \right)_{T,p}$$

Where dS is the entropy change of the polymer chains from their most probable conformations in the unstretched material. The distribution of these conformations is Gaussian, and the probability of finding a chain end in a unit volume of space defined by x , y and z at a distance r from the other chain end has been calculated based on the random flight model and found to be:

$$W(x, y, z) = \left(\frac{b}{\sqrt{\pi}} \right)^3 e^{-b^2 r^2} \quad (\text{Rayleigh, 1919})$$

where $b^2 = (3/2) x/l^2$, x being the number of links with length l in a polymer chain. From statistical thermodynamics:

$$S = k \cdot \ln[W(x,y,z)] = \text{Constant} - kb^2r^2$$

Where k is Boltzmann's constant. Then, for the extension of a single polymer molecule by dr , the retractive force can be found by:

$$f = -T \left(\frac{\partial S}{\partial r} \right)_{T,p} = 2kTb^2r$$

The stress required to strain a network of these polymer chains can be shown to be:

$$\sigma = \frac{\rho RT}{M_c} \left(\lambda - \frac{1}{\lambda^2} \right)$$

where σ is stress in MPa, R is the gas constant (J/mol·K), ρ is the bulk density (kg/m³), M_c is the molecular weight of the polymer chain, λ is the extension ratio (l/l_0). The elastic modulus of the elastomer fiber (E_f) can then be given by:

$$E_f = \frac{d\sigma}{d\lambda} = \frac{\rho RT}{M_c} \left(1 + \frac{2}{\lambda^3} \right)$$

The above relationships works quite well under the condition that the deformation is accommodated by the uncoiling of polymeric chains (typically <300% strain). Beyond this amount of deformation, primary bond stretching and chain sliding can occur, which results in a higher elastic modulus than that predicted above. E_f is shown graphically as a function of true strain in Figure 8.

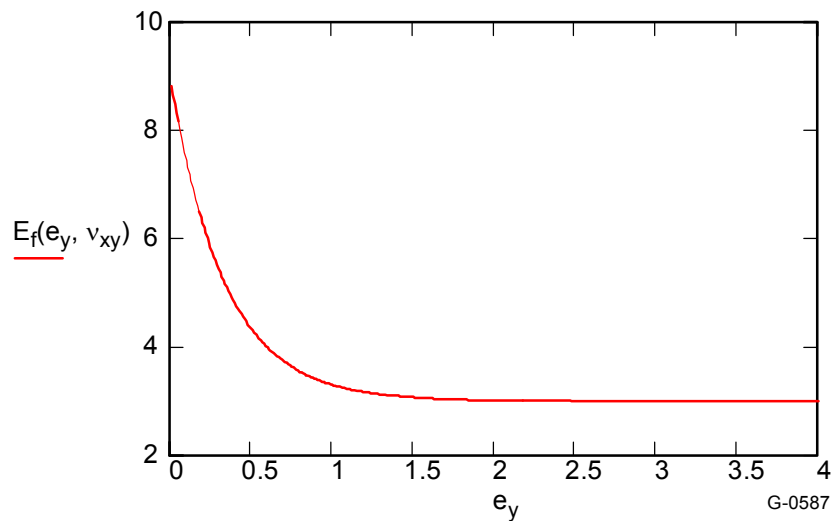


Figure 9. The calculated elastic modulus of an elastomeric fiber (Estane 58245 TPU) as a function of true strain. In real systems, the elastic modulus reaches a minimum near strains of 2-3, and increases at higher strains as the bonds are stretched along the backbone of the polymer chains.

6.3 Mechanical Properties of Non-Woven Fabrics

D.R. Petterson, "On the Mechanics of Non-Woven Fabrics", Ph.D. Dissertation, MIT, 1959

It has been shown by Petterson that the mechanical properties of any 2-dimensional, non-woven orthotropic fabric can be calculated if the following are known: the mechanical properties of the individual fibers, the orientation distribution of the fibers, the relative fiber-fiber bond strength. The last factor can be related to Poisson's ratio of the fabric. Effectively, the stress on a fabric under uniaxial tension at any given strain can be predicted by summing the transformed stresses on all of the fibers, and then transforming this summed stress back into the tensile direction, y :

$$\sigma_y = \sum_{i=1}^n \sigma_f \cos^2(\theta + \beta) \Phi(\beta) = \int_{-\pi/2}^{\pi/2} \sigma_f \cos^2(\theta + \beta) \Phi(\beta) d\beta$$

where σ_f is the fiber stress, $\Phi(\beta)$ is the fiber orientation distribution function, θ is the angle between the tensile axis y and the fiber orientation axis L , and β is the angle between the individual fibers and axis L . σ_f is calculated assuming that all of the strain is elastic: $\sigma_f = E_f \cdot \epsilon_f$.

Petterson calculates the stress on the fabric in the following way. For a given fabric strain, the strain on the individual fibers can be calculated:

For small strains where β is constant:

$$\epsilon_f = \epsilon_y (\cos^2(\theta + \beta)) - \nu_{yx} (\sin^2(\theta + \beta))$$

For large strains where β is a function of ϵ_y :

$$\epsilon_f = (\cos^2(\theta + \beta)(1 + \epsilon_y)^2 - \nu_{yx} (\sin^2(\theta + \beta)(1 + \frac{\epsilon_y}{\nu_{yx}})^2)^{\frac{1}{2}} - 1$$

For an elastomer, we are concerned with very large strains. In other words, the fibers become oriented in the direction of the tensile axis at large strain values. Unfortunately, Petterson does not solve the integral for this condition. The integral that must be solved is:

$$\frac{E_y}{E_f} = \frac{1}{\epsilon_y} \int_{-\pi/2}^{\pi/2} \cos^2(\theta + \beta) \left(\cos^2(\theta + \beta)(1 + \epsilon_y)^2 + \sin^2(\theta + \beta)(1 + \frac{\epsilon_y}{\nu_{yx}})^2 \right)^{\frac{1}{2}} - 1 \Phi(\beta) d\beta$$

If we assume that the fabric of interest is isotropic, then $\Phi(\beta) = 1$. In addition, the solution is independent of θ , therefore we can set $\theta = \pi/2$ to simplify the equation further. The simplified integral is still difficult to solve analytically, therefore, Mathcad was used to estimate the solution to this integral using the Trapezoidal Rule and increments of $\pi/64$. This solution is

shown graphically in Figure 9 as a function of ε_y for three different values of ν_{yx} ranging from 0.2 to 0.46.

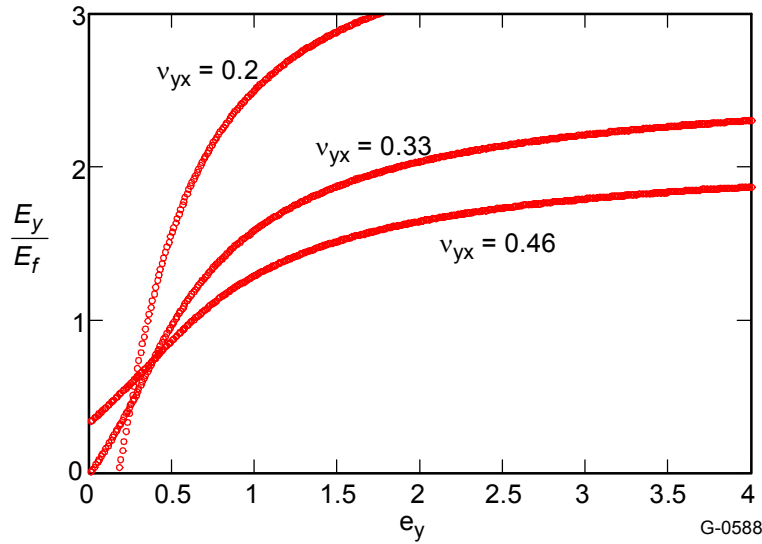


Figure 10. The calculated ratio of the fabric modulus (E_y) to the fiber modulus (E_f) for an isotropic, non-woven fabric under uniaxial tension

Since the fibers are aligning towards the tensile axis during deformation, one would expect that the ratio of E_y/E_f would increase with increasing strain and approach a value of 1 at high strains. We see from Figure 4 that the ratio E_y/E_f does indeed increase with increasing strain; however, we also see two abnormalities. First, E_y/E_f is negative at very low values of ν_{yx} and ε_y . Second, E_y/E_f is larger than 1 at high values of ε_y . These abnormalities are believed to be artifacts of the Trapezoidal Rule estimation used to solve the integral. Indeed, it was observed that these artifacts were much more severe when an interval of $\pi/16$ was used rather than $\pi/64$. While the specific values calculated for E_y/E_f may not be accurate, the general trend can still be appreciated. The fabric becomes stiffer as ε_y increases and ν_{yx} decreases.

It can be seen that the value of E_y/E_f is very sensitive to ν_{yx} . Petterson found that ν_{yx} is affected strongly by the fiber-fiber bond strengths. He showed experimentally that increasing the binder content of his fabric from 1% to 2% by weight resulted in a corresponding decrease in ν_{yx} from 0.4 to 0.15. Therefore, fiber-fiber bond strengths are extremely important in the stiffness and strength of non-woven fabric materials. It should be noted that Petterson calculated that the value of ν_{yx} for a perfectly bonded fabric would be $1/3$. Values of ν_{yx} larger than $1/3$ are the result of insufficient fiber-fiber binding, while smaller values are likely due to the resistance of a stiff binder phase to contraction in the x direction. Since no binders are used in PSI's non-woven elastomeric fabrics, we would expect $\nu_{yx} \geq 1/3$ for these materials.

6.4 Combined Model for Elastomeric Non-Woven Fabrics

It was shown in Section 6.3 that the elastic modulus of an elastomer can be calculated by considering the change in entropy of the material during deformation:

$$E_f = \frac{d\sigma}{d\lambda} = \frac{\rho RT}{M_c} \left(1 + \frac{2}{\lambda^3} \right)$$

In addition, Petterson's model for large strains in non-woven, isotropic fabrics has been solved to provide a value for the elastic modulus of a fabric in terms of the fiber modulus and fabric strain. It is a trivial matter to substitute for E_f in Petterson's model so that the change in E_f as a function of strain due to the decrease in entropy is accounted for. By doing so we obtain a function for the elastic modulus of the elastomeric fabric as a function of strain. This relationship is shown graphically in Figure 10. Similarly, the stress can be calculated as a function of strain since $\sigma_y = E_y \cdot \epsilon_y$. This relationship is shown graphically in Figure 11 as a function of true strain. A comparison between the measured and calculated stress-strain curves for an electrospun elastomeric fabric are shown in Figure 11.

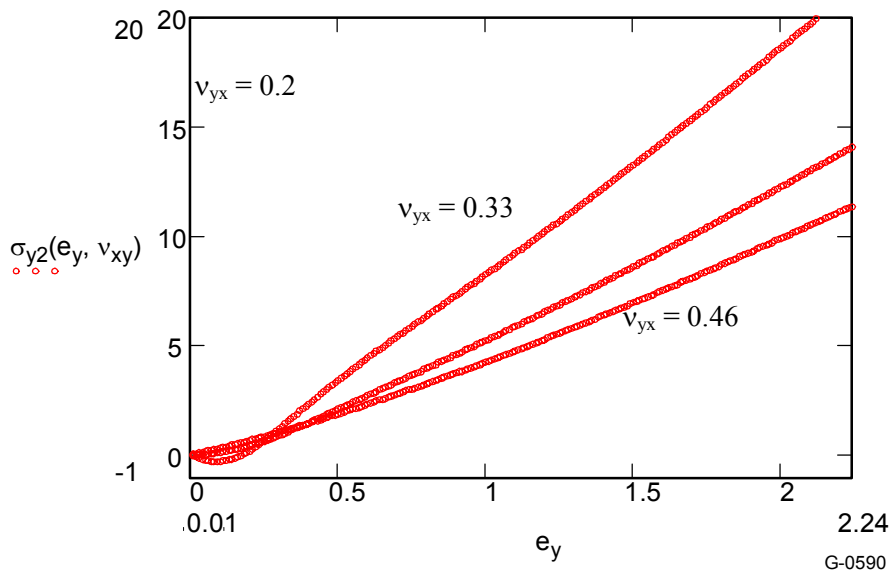


Figure 11. The calculated modulus as a function of strain for a non-woven elastomeric fabric under a uniaxial tensile stress

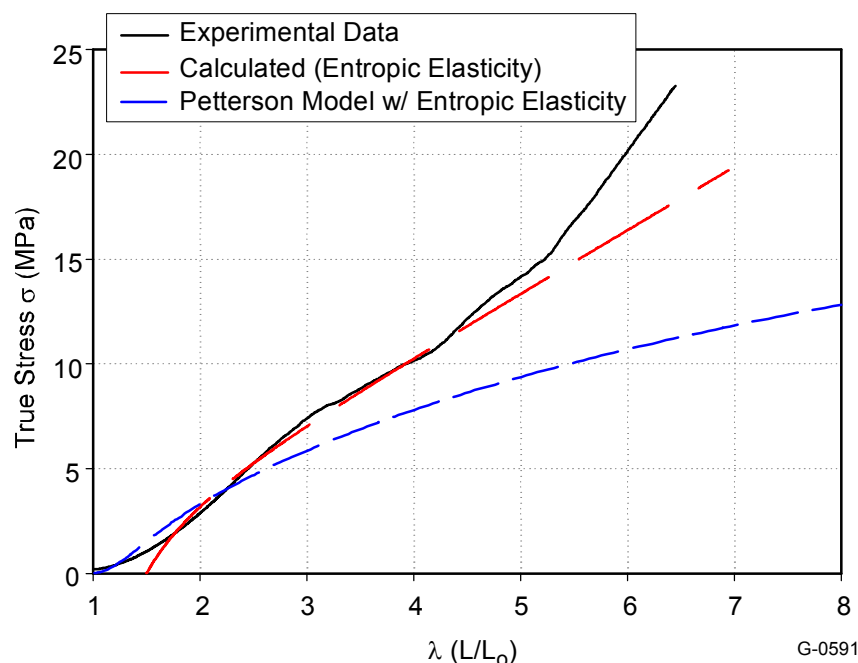


Figure 12. A comparison between measured and calculated stress-strain curves for a non-woven fabric synthesized at PSI by electrospinning Estane 58245 TPU

6.5 Experimental Results

Estane membranes were electrospun using two different spinning distances and examined for morphology by SEM and mechanical properties by tensile strength measurement. Figure 12 show the stress strain plot for electrospun Estane at 15 cm (blue, high elongation) and 25 cm (red, low elongation) offset, and a solid Estane film sample (black). SEM Images of the electrospun samples is shown in Figure 13. The SEM images show excellent fiber to fiber bonding for the sample spun at short spinning distances. This sample corresponds to the sample with stronger mechanical strength. At shorter spinning distances the fibers hit the substrate with more residual solvent due to shorter flight times. The fiber to fiber bonding is enhanced due to a solvent welding effect.

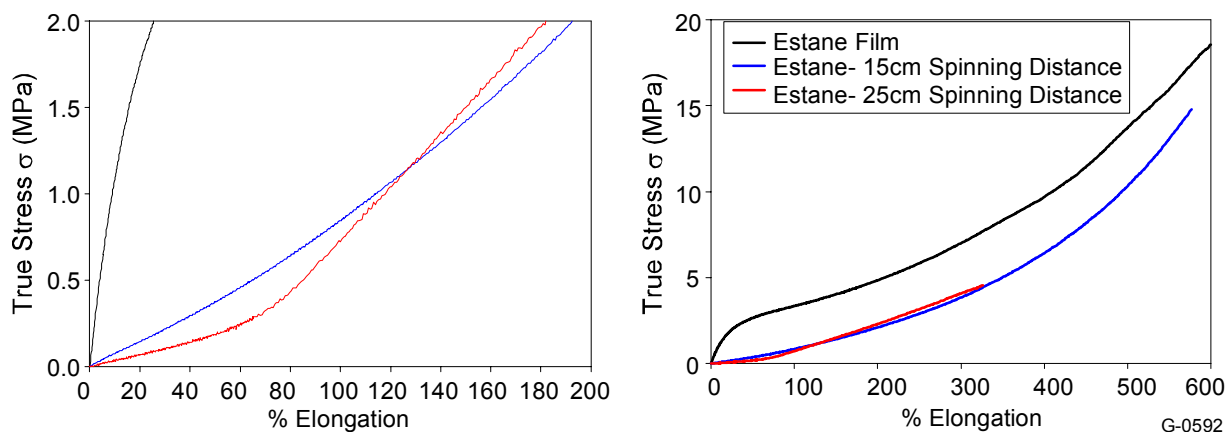


Figure 13. Stress Strain Plot for Estane Film (black) and Electrospun Estane

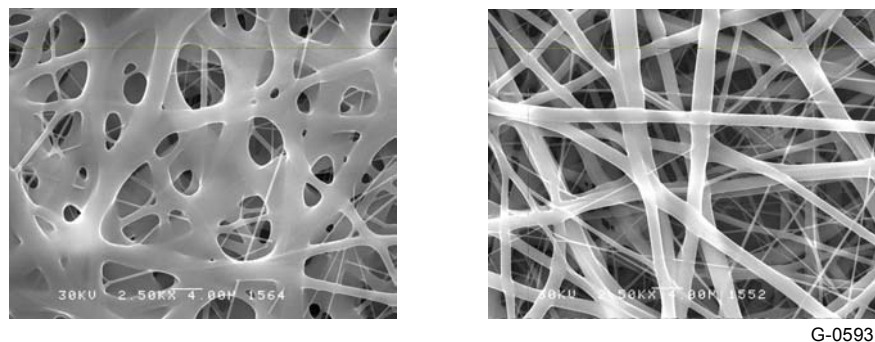


Figure 14. SEM Images of Electrospun Estane at 15 cm (left) and 25 cm offset

6.6 Summary and Conclusions

A review of the mechanical behavior of elastomeric in non-woven fabrics was presented. In general, it has been shown that the elastic modulus of these fabrics is highly dependent upon both ϵ_y and ν_{yx} . Petterson showed that the strength of the fabric increased as ν_{yx} decreased, and that ν_{yx} decreased as the fiber-fiber bonding increased. It is important to note that for a single phase fabric, $\nu_{yx} \geq 1/3$. It is also important to note that fiber size does not affect the strength of the fabric, provided that the fibers are long compared to distance between fiber-fiber bonds.

From this review, three strategies for increasing the strength of TPU non-woven fabrics have been identified:

1. The strength of a fabric is directly proportional to the strength and modulus of the fibers. Therefore, the strength of the fabric can be increased by simply increasing the strength of the TPU raw material. The strength and modulus of TPU's can be controlled by cross-linking, where an increase in the cross-link density will result in a higher strength and modulus, but a lower elasticity.
2. The modulus of a fabric has been shown to be very sensitive to Poisson's ratio, ν_{yx} . Petterson showed experimentally that ν_{yx} of a fabric could be reduced significantly by improving the number and strength of fiber-fiber bonds in the fabric. Therefore, the modulus and strength of the elastomeric non-woven membranes should increase significantly if the fiber-fiber bonding is improved. PSI has already seen evidence of this effect empirically.
3. Woven elastomeric fabrics incorporate strong, non-elastic fibers to control the strength and elasticity of the fabric. Non-woven elastomeric fabrics could similarly incorporate strong fibers to improve the strength of the fabric. The fibers would have to be configured in such a way that the impact on elasticity is minimized. This may be possible by bonding the non-elastic fibers to the elastomeric fibers, but not to each other. In this way, the non-elastic fibers will "uncoil" at low strains and will not support a stress until they are aligned at higher strains.

7. Process Parameter Effects

There were two general types of electrospinning configurations that were utilized during this reporting period, the standard (Std) or the parallel plate (PP) method. The main difference being the two systems is the inclusion of a metal plate through which the electrospinning nozzle would protrude (PP). Figure 14 illustrates the difference between the two systems.

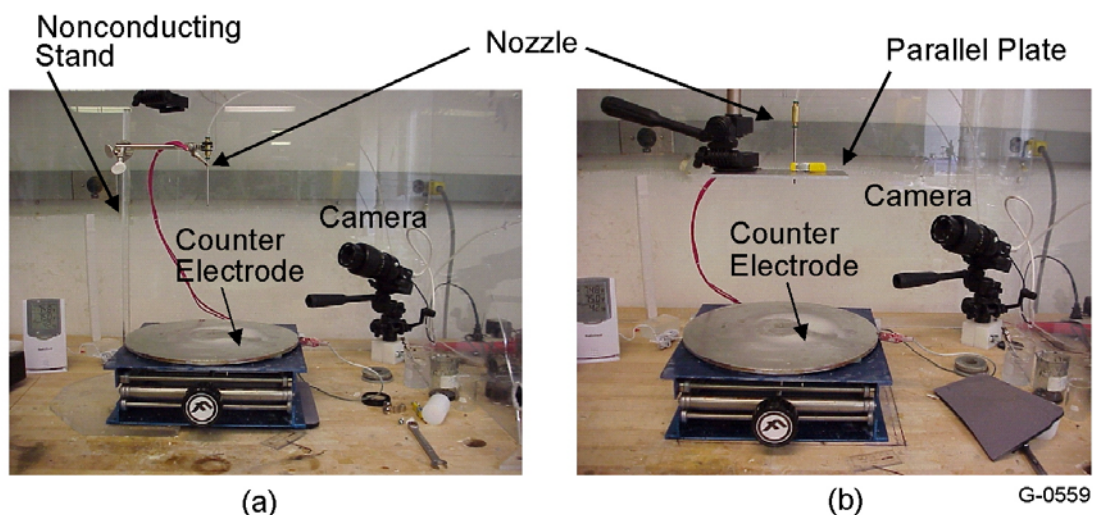


Figure 15. (a) Standard and (b) Parallel Plate (PP) electrospinning configurations

In the PP system, the metal plate in combination with the counter electrode act to simulate a parallel plate capacitor. This configuration improves upon the linearization of the electric field within the electrospinning system, resulting in a more collimated deposition path towards ground. The standard configuration on the other hand, emits a cone-shaped deposition pattern towards ground, covering a larger area with a lower average membrane thickness.

Materials deposited in either configuration were classified using a qualitative labeling system developed to describe the experimental results. Initially the deposits were labeled as being either dry (D) or wet (W) as determined visually (dry deposits were characteristically a whitish coloration, wet deposits appeared more as transparent films). However, it was noticed that during the deposition process the Taylor cone (at the tip of the electrospinning nozzle) sometimes would dry up and solidify during deposition. This led to a further classification to describe the electrospinning process stability resulting in the addition of the letter “S” to the sample label. An example of this behavior is shown in Figure 15.

Finally, the letter “V” was used to denote a formulation with a viscosity too high to allow electrospinning of the material. Table 1 shows a summary of the classifications developed:

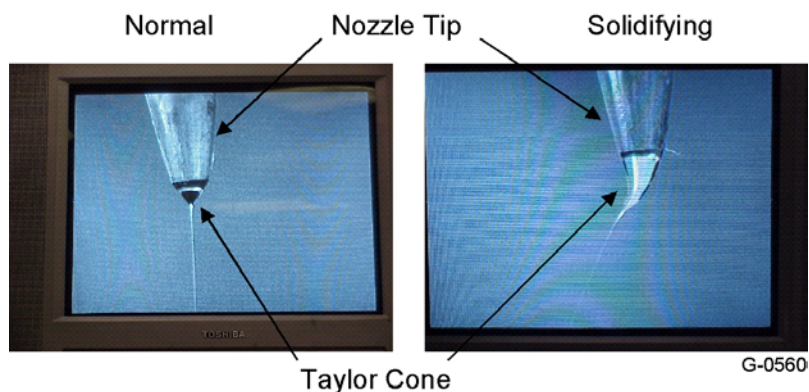


Figure 16. Photographs depicting a solidified Taylor cone formed during electrospinning

Table 1. Labeling System used to Describe Experimental Results

Label	Description
D	Dry deposit
W	Wet deposit
DS	Dry deposit / Cone solidified
WS	Wet deposit / Cone solidified
V	Material too viscous to electrospin

7.1 Formulations

7.1.1 Solvent/Polymer Blends

Estane may be dissolved using either Dimethyl Formamide (DMF) or N-methyl - 2-Pyrrolidone (NMP) as the solvent. It was found however that blending DMF with a small amount of NMP resulted in a higher tensile strength for electrospun Estane membranes. Specifically a 90%DMF/10%NMP mix was found to be optimal. A 15% loading of Estane in this solvent blend was used for our initial work. This concentration previously indicated an average fiber diameter below 200 nm. The results of our first experiments are shown in the Figure 16.

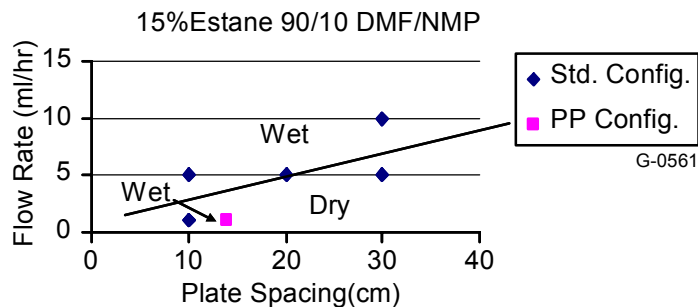


Figure 17. Division between dry and wet electrospun deposits

For reasonable plate separations, dry fiber formation could not be achieved above flow rates of 5 to 10ml/hour for this solution (far lower than that achieved for the Worthen adhesive). Additionally, the use of the parallel plate configuration had constrained the fiber whipping action that occurs during electrospinning to a very small diameter. This small path length from the nozzle tip to the substrate did not allow the electrospun fiber to have the opportunity to dry adequately before hitting the substrate. This resulted in wetter deposits as compared to that seen for the standard configuration at equivalent fluid flow rates.

Arcing of the applied voltage is another limiting factor that was seen in these experiments. As the nozzle-to-plate separation increases, the applied voltage must also increase to support a stable electrospinning condition. A point eventually is reached where the electric field becomes significant enough to breakdown the air at various points in the system leading to a rapid increase in current and an unstable process condition. This was reached at an electric field intensity of approximately 0.7kV/cm for the system studied in Figure 17.

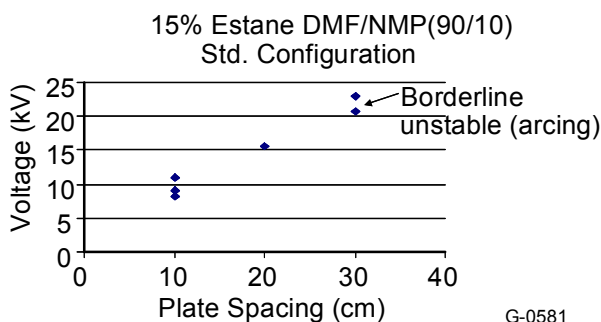


Figure 18. Applied voltage variation for a standard electrospinning system

From Figures 16 and 17 it appears that electrospinning of the present Estane formulation has two limitations:

1. High flow rates cause wet deposits
2. Longer deposition distances produce electrical system instabilities.

We believed that higher vapor pressure solvents could produce dryer deposits due to faster solvent evaporation during the deposition process. We contacted Noveon (manufacturer of Estane) and they indicated the use of tetrahydrofuran (THF) as possibly a good solvent for our application. Additionally, they also recommended the use of acetone as a diluent if needed. The vapor pressures of the various solvents/diluents being considered in our formulations are listed below in Table 2.

Table 2. Vapor Pressure of Solvents

Solvent	Vapor Pressure (mm Hg)
NMP	0.3
DMF	2.7
THF	162
Acetone	185

We formulated several blends of solvents to evaluate their effects on the morphology of the deposited material. Figure 18 shows our results.

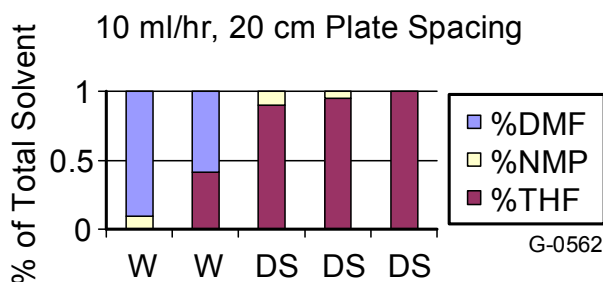


Figure 19. Estane in various combinations of THF, NMP, and DMF

As expected, the increase in concentration of THF resulted in dryer deposits. However, at these levels of higher vapor pressure solvent blends, the Taylor cone eventually solidifies, allowing only short deposition times.

At this point we decided to improve testing efficiency by increasing the Estane concentration to 18%. The increased Estane concentration would allow for a heavier deposit during an equivalent time period allowing easier optical observations of the material for shorter test periods. Additionally, we fixed the deposition time at 15 min and used 10ml/hour as a standard flow rate. When the Taylor cone solidified it always happened in less than 10 min from the start of the deposition. The rate of 10 ml/hour was at a flow rate just higher than that seen to produce dry deposits using the unmodified formulations (see Figure 16).

With the new test methodology in place, we focused on the NMP/THF solvent system. Noveon had indicated that NMP had the best solvating properties for Estane.

Figure 19 shows the results of these experiments.

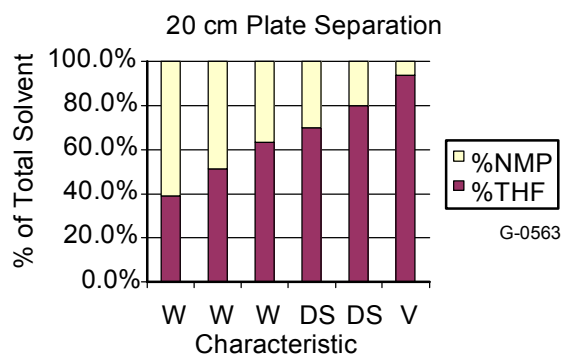


Figure 20. 18% Estane in THF/NMP

The results are similar to those of Figure 18. In this case the addition of THF eventually lead to a solution too viscous to electrospin. We additionally looked at various additions of acetone to the blends with no success. The same trends from wet to dry/solidified to viscous were seen. Further work on solvent blends was halted at this point in the development process.

7.1.2 Humidity Effects

One other aspect of these experiments was an apparent dependency on ambient humidity levels. Below about 25% RH, no fiber formation was seen with solution concentrations up to 20% Estane, only electrospayed droplets. Fibers returned at levels above 32%RH. This led us to look further into the Estane material. Figure 20 is a picture of the Estane pellets as received from the manufacturer and then subjected to a vacuum bake.

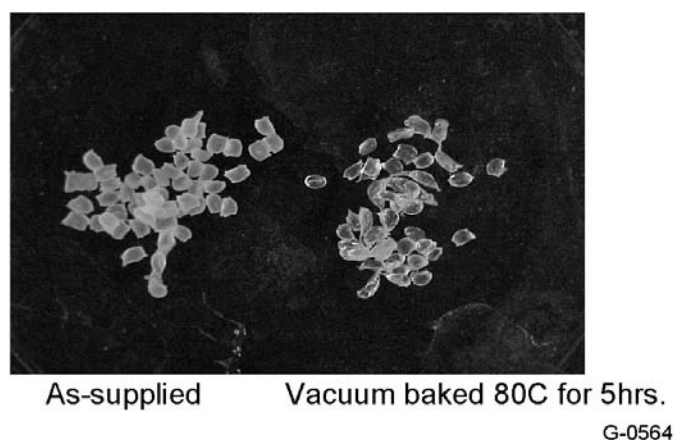


Figure 21. Visual confirmation of moisture in Estane pellets

The translucency of the as-supplied material is indicative of moisture absorption of the polyurethane compound. We ran several experiments pre-drying the Estane before formulation. These appeared to have no effect on solution preparation, fiber formation, or deposit morphology. It is possible though that the ambient humidity level is interacting with the electrospun fiber during the deposition process and must not be overlooked.

We also discovered that at the higher flow rates (>5 ml/hour) that the material is also being sprayed (the actual flow rate this occurs at appears to depend on the humidity level). Higher flow rates generally necessitate the use of higher electric fields. These fields may produce additional strain on the fiber as it is being formed, pulling it apart while still wet, then allowing surface tension to redistribute the material into a droplet. Examples of the deposit are shown below in Figure 21.

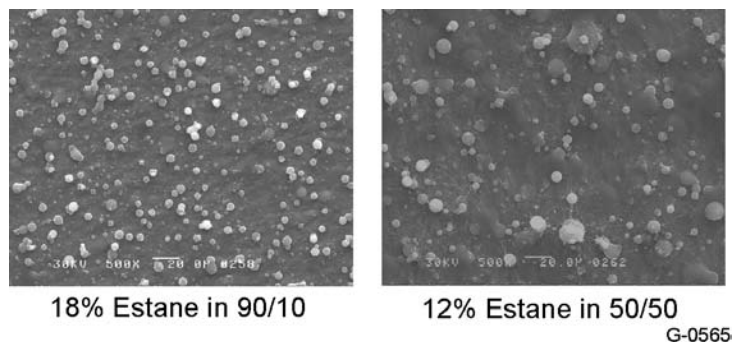


Figure 22. SEM images at 500x for electrospun material at a flow rate of 10ml/hour

Summary

- Various combinations of THF, NMP, DMF and Acetone solvents alone did not increase the deposition rate of an 18% Estane solution above 5ml/hour.
- Estane solution is humidity sensitive.
- Non-fibrous deposits can result when depositing Estane at low humidity levels or at fluid flow rates of approximately 10ml/hour or greater.

7.1.3 Enhanced Conductivity

The effect of electrical conductivity on the rate of deposition was evaluated. Additives included iron (II) chloride and tetrabutylammonium hexafluorophosphate (TBAHFP) introduced at 0.2 w/o and 0.02 M concentrations respectively. Figure 22 below shows the variation of conductivity and viscosity with the different additives.

TBAHFP showed little effect on the solution viscosity but about a 100:1 effect on increasing the conductivity. Alternately the iron (II) chloride increased the solution viscosity by about 40% while increasing the conductivity by 80:1. These two solutions were electrospun using the standard configuration. The results are indicated in Figure 23.

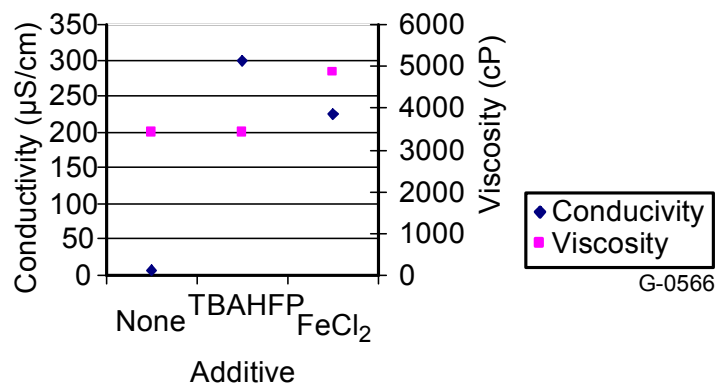


Figure 23. Effects of conductivity enhancement additives on an 18% Estane in a 90% DMF / 10% NMP solution

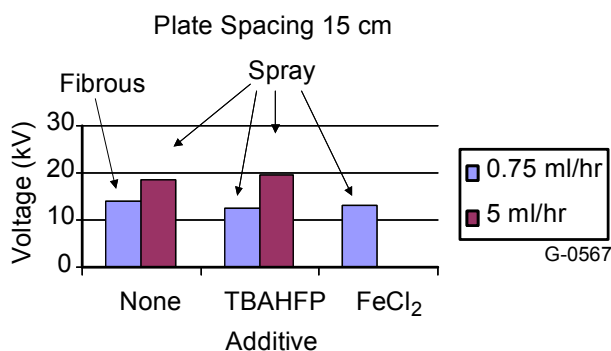


Figure 24. Deposition characteristics for conductivity modifiers

The conductivity enhancement of the Estane solution appears to produce spray droplets of the material, especially noticeable at higher flow rates. Additionally, the more conductive solution containing the TBAHFP material was difficult to electrospin due to the high current carrying capability of the solution. This led to arcing and an unstable electrospinning jet. We therefore decided to halt this effort and feel it is not the appropriate path for improving the deposition rate of the Estane material.

7.2 Multi-Nozzle Arrays

To date, the electrospinning rate of Estane has been limited to 1-5 ml/hr regardless of solvent composition and presence of conductivity modifiers. The use of solvents or conductivity enhancements has limited the electrospinning rate of Estane to between 1 and 5 ml/hour. The development of a multiple nozzle array could increase the deposition rate to acceptable levels. Utilizing the parallel plate design, a multi-element nozzle holder was developed as shown in Figure 24.

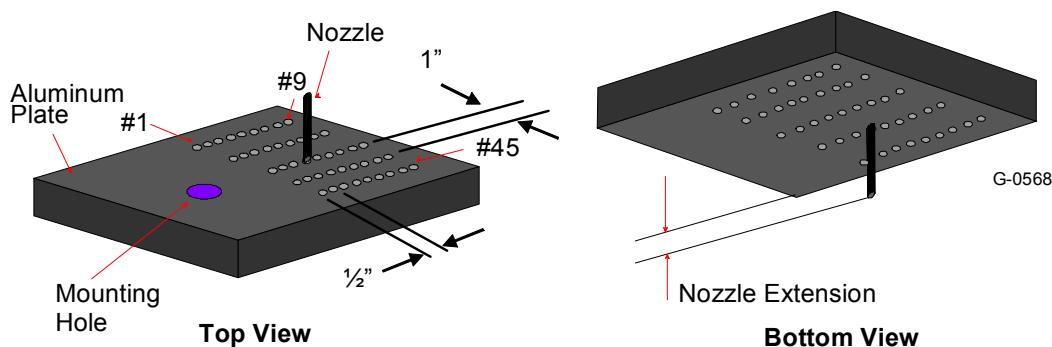


Figure 25. Parallel plate showing numbering sequence for multiple nozzles and geometry

The PP method is attractive due to the columnar-like deposition path from the nozzle tip to the counter electrode. This feature should limit electrostatic interaction between adjacent nozzles, allowing closer spacing of nozzle tips and provide some latitude in plate spacing over the standard electrospinning configuration. The hole-numbering scheme was used to identify locations for experimental purposes. The formulation used in all experiments was 18% Estane in 90%DMF/10%NMP. The deposition time was limited to 20 seconds (long enough to visually see the deposition area) and the flow rate set at 1 ml/hour (intermediate deposition rate for Estane).

7.2.1 Single Element

The effect of nozzle position was categorized using the numbering designation shown in Figure 24. A nozzle was placed at one of five locations: front (#40), left (#19), center (#22), right (#27), or rear (#4). Initial work was intended to draw a baseline from which future experiments in increasing the nozzle count across the array would benefit. The first trials evaluated spot size of the deposited material as a function of several process parameters. Figures 25 (a), (b), and (c) depict the trends found.

The trends for a single nozzle were as expected. Large diameter spots grow with time. As the area directly beneath the nozzle becomes less conductive due to the fibrous deposit, the most direct path to ground for the electrospinning process expands to the circumference of the deposit. This effect is also responsible for producing a “hill-like” thickness distribution of fiber.

We also found the spot size to increase with flow rate for a given period of time. The higher flow rates deposit more material per unit time, quickly building up an insulating layer beneath the nozzle tip. Again this pushes the fiber deposit outward to more conductive regions of the sample.

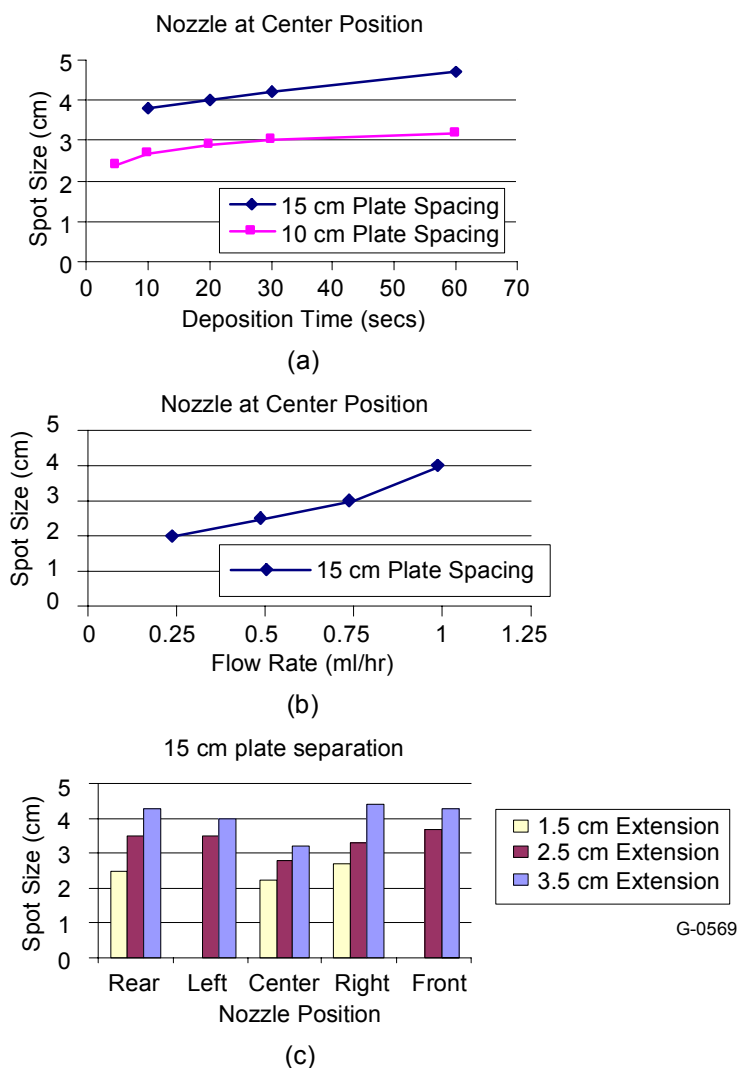


Figure 26. Effect of (a) deposition time, (b) flow rate, and (c) nozzle position/extension on spot size

Finally, the nozzle position/extension plot of Figure 25(c) shows a few interesting trends. The deposit produced from the center nozzle is obviously the narrowest of all positions evaluated. Since the other positions are at or near the edge of the parallel plate, the electric field lines will tend to separate further at those locations similar to the fringing fields of a capacitor. The internal electric field lines will be extremely linear terminating at almost perpendicular angles with the top and bottom electrode surfaces. This linear field constrains the electrospun polymer and focuses the deposition pattern at the center position. From Figure 25(c) it can also be seen that as the nozzle extends further from the plate towards the substrate, the more distorted the electric field lines become in the region of the nozzle, and therefore the wider the deposition area.

Figure 26 shows the next set of experimental data illustrating the deposition precision of a single nozzle system. The precision was determined by assuming that the center of any deposit would fall directly underneath the center of the nozzle depositing the material. Movement in any direction from this center point would indicate an error in material placement as is noted as a “deviation from target”.

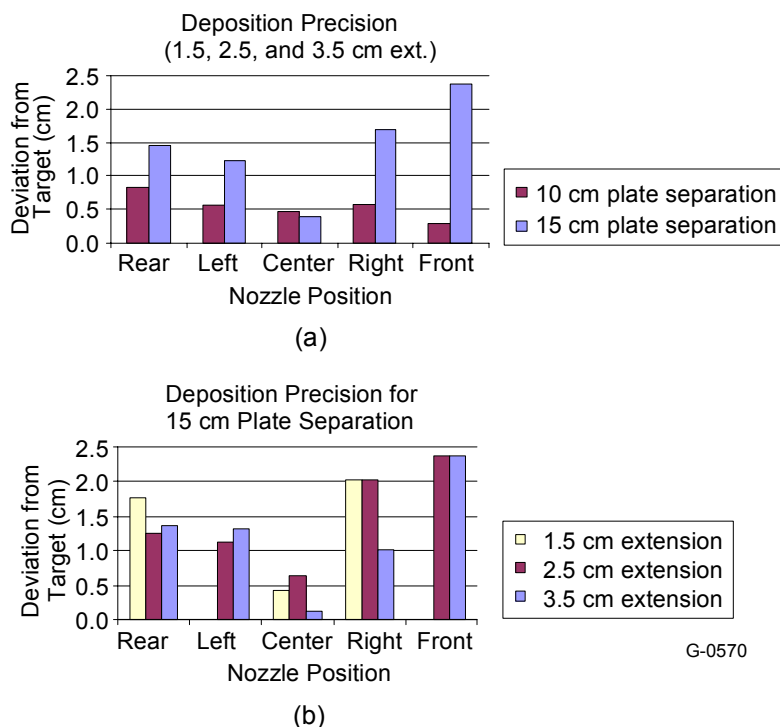


Figure 27. Effect of (a) nozzle position/plate separation and of (b) nozzle position/extension on the precision of depositing the electrospun material

As the plate separation or the nozzle-to-substrate distance decreases, the error in placement of the depositing material also decreases. Shorter deposition distances do not allow time for systematic errors to grow.

The trend shown in both Figures 26(a) and (b) indicate that the center position provides the most precise deposition of material owing to the electric field linearity. The lack of any trend with respect to nozzle extension in Figure 26(b) however is not expected. Our theory would have suggested an improvement in precision with a longer extension due to a shorter working distance. This may in general be true, but experimental error or the magnitude of the extension was not great enough to bear out this relationship.

The final relationship drawn during the single nozzle evaluation was that of applied voltage. Figure 27 demonstrates the variation of this parameter.

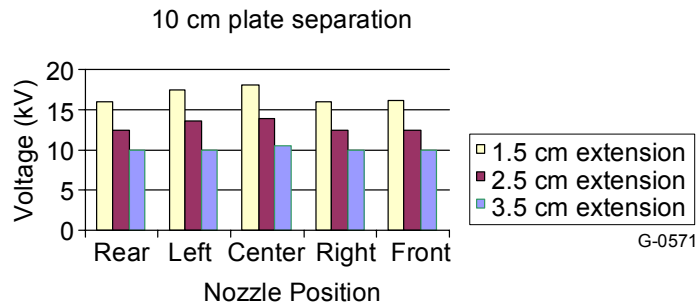


Figure 28. Voltage variation with position for a single nozzle system

As expected the voltage decreases with an increase in nozzle extension. This trend is due to the need to efficiently generate charge at the nozzle tip for electrospinning to initiate. Charge build-up is much easier at a point than a plane (e.g., a lightning rod). The further the nozzle extends from the parallel plate, the less voltage is needed to generate the necessary charge for electrospinning (the more it acts like a point in the electric field).

Summary of a Single Nozzle System

- Spot size increase with time and increased fluid flow rate.
- Deposition precision improves with decreasing plate spacing.
- Generally spot size increases and precision grows worse from center to edge of the nozzle plate.
- Shorter nozzle extensions require higher voltage, have poorer precision and produce smaller spot sizes than larger extensions.

7.2.2 Two-Nozzle System

The analysis of a two-nozzle system required the development of an additional parameter to measure the degree of deposit overlap (or lack of it) when two nozzles are placed side-by-side. During electrospinning, surface charges are developed on the spun fiber. Therefore we expect the fiber ejected from two nozzles side-by-side to electrostatically interfere with each other at close separation distances. The new parameter to measure this effect is coined the “overlap ratio” and is defined in Figure 28 and the following text:

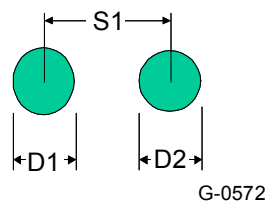


Figure 29. Diagram used to define the overlap ratio for a two-nozzle system

The Overlap Ratio (O.R.) is defined as:

$$\text{O.R.} = \frac{S1}{((D1 + D2) / 2)}$$

where D1 and D2 are the diameters of each spot and S1 is the center-to-center separation distance of the two spots. An overlap ratio > 1 indicates no overlap between the two spots.

A second difference was also investigated with the two-nozzle effort, the use of “dummy” nozzles. These “dummy” nozzles were fabricated from the same material as the electrospinning nozzle and with the same geometry, however no fluid was fed to them. These nozzles were placed near the active nozzles to try and adjust the electric field patterns of the system. Figure 29 below shows a setup with two active and two dummy nozzles. The active nozzles are the inner two nozzles with brass fittings near the top of the photo. The outer two dummy nozzles were extended further towards the substrate in this particular configuration.

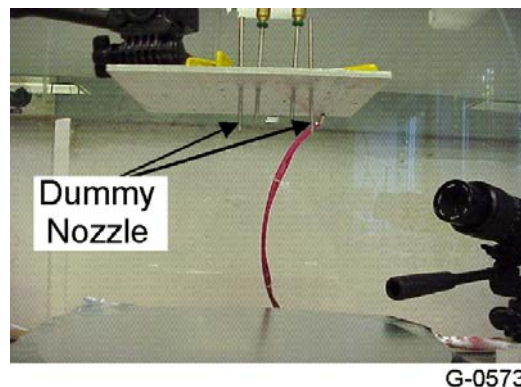


Figure 30. A two-nozzle system with two dummy nozzles

Similar experiments were run with the two-nozzle system as that of the single nozzle. Figures 30(a), (b), and (c) show the trends found for the two-nozzle set-up. The dummy nozzles were always placed linearly to the outside of the active nozzles (as shown in Figure 29).

Figure 30(a) shows three important trends: the overlap ratio 1) becomes worse at closer plate spacings, 2) shows little variation with nozzle extension, and 3) approaches unity at 10 and 15 cm plate spacings. None of these trends are surprising based upon our single nozzle results.

There are also three main trends seen in Figure 30(b): 1) the additions of dummy nozzles require higher voltages for initiating electrospinning, 2) the further the dummy nozzles are extended the higher the applied voltage needs to be, and 3) shorter distances between nozzles require higher voltages. This trend was seen both with and without the dummy nozzles present. In a few cases we were actually unable to electrospin stably using small nozzle separations.

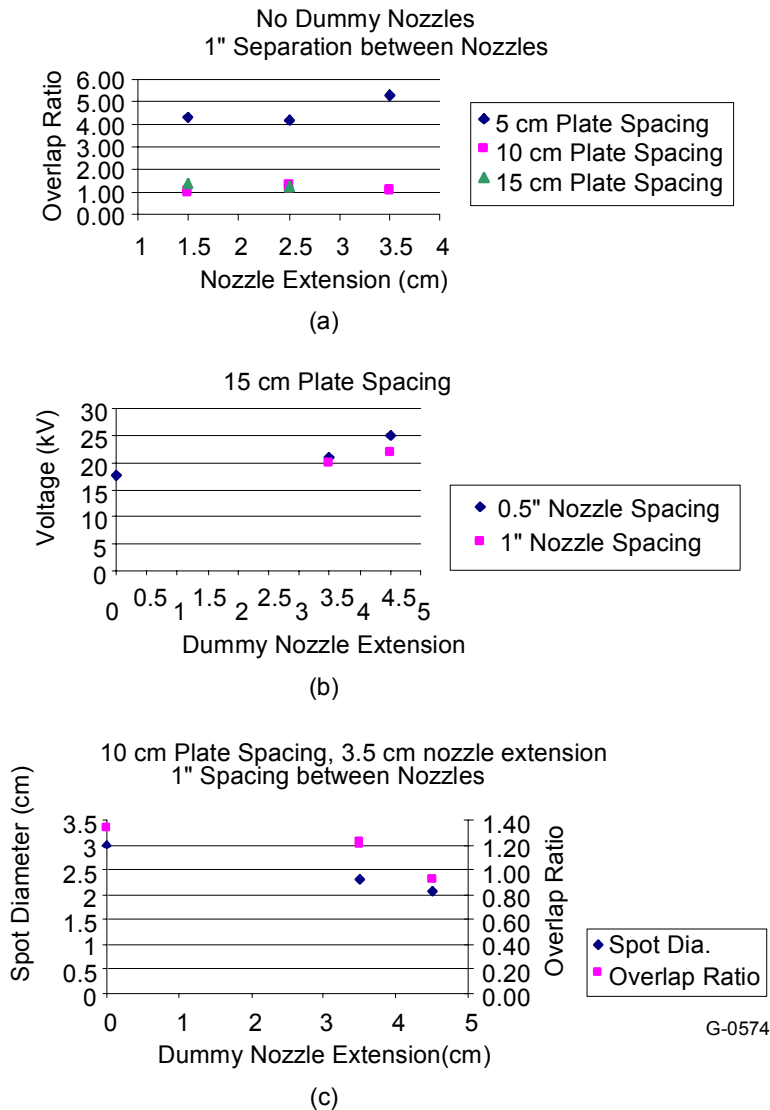


Figure 31. Various characteristics of a two-nozzle electrospinning system

It appears that there is some amount of time to build up the necessary charge in each nozzle for electrospinning to commence. Once the electrospinning begins an initial spike of current (charge) is delivered to ground. If one nozzle starts to electrospin, the available charge in the circuit will flow through this path to ground, leaving the second nozzle without enough charge to initiate flow. Once equilibrium is reached with the first nozzle, the second nozzle can initiate spinning, however the initial charge surge usually affects the first nozzle and may stop it from electrospinning or slow it down. This process proceeds until the system comes to equilibrium. The effect is particularly noticeable in systems with close nozzle spacings.

And finally, in Figure 30(c) an extremely encouraging trend is shown. The dummy nozzles are capable of decreasing the spot size and the overlap ratio (to < 1) by adjusting their amount of extension. This would allow more nozzles per unit area and thereby increase the

deposition rate. Additionally, the ability to overlap deposition patterns could provide a more uniform deposit, reducing or eliminating mounding of the material.

Summary of Two Nozzle Experiments

- Best overlap ratio requires use of dummy nozzles.
- Dummy nozzles decrease spot size and overlap ratio.
- Overlap ratio and spot size decrease with decreased plate spacing.
- Space charge repulsion of the spinning fibers results in limiting overlap.
- Larger nozzle spacing is more easily stabilized and controlled.

7.2.3 Three-Nozzle System

For the three-nozzle evaluation, the flow rate was fixed at 1 ml/hour and the active nozzle extension at 3.5 cm. We evaluated two different configurations of nozzles: a linear array and a triangular array. For the linear array we also looked at two different nozzle spacings: 1 in. and 1/2 in. A picture of the triangular array is shown in Figure 31 below:

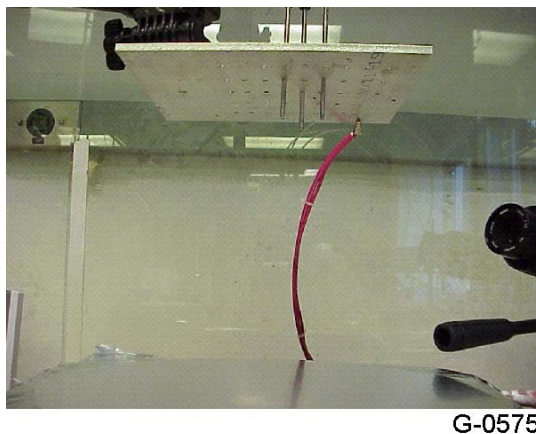


Figure 32. Triangular nozzle array

The nomenclature used to identify the geometry of the arrays is as follow:

7.2.3.1 Linear 0.5 or 1.0

- Linear array of three nozzles with either 0.5 or 1.0 in. spacing between adjacent nozzles
- Overlap ratio is calculated using averages of the three diameters and the two spacings (Left-Center and Center-Right).

7.2.3.2 Triangular 1.0

- Nozzles configured in the shape of a triangle with the base and height equal to 1.0 in.
- Overlap ratio calculation is similar to the two-nozzle system using the spots formed at the base of the triangle.

Based upon our experience to this point, the 3.5 cm active nozzle extension was decided upon due to the lower voltage required for initiating electrospinning (Figure 27) allowing more latitude for stable operation. Dummy nozzles were again evaluated in these systems to help linearize the electric fields and improve the deposition control. For the linear systems they were again located linearly to the outside of the outermost active nozzles. For the triangular array, the dummy nozzles were located to the left and right of the base points of the triangle. These arrangements are depicted in Figures 32(a) and (b).

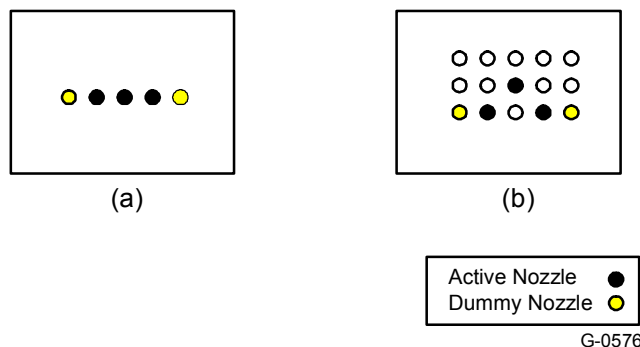


Figure 33. Top view of nozzle arrangements for (a) linear and (b) triangular three-nozzle systems

Figures 33(a), (b), and (c) display the results of our experiments. There is some information missing from these charts, in particular for the linear arrays. This was due to instabilities in the electrospinning system. These instabilities were similar to the two-nozzle system and are linked to the difficulty in obtaining charge equilibrium simultaneously across all active nozzles.

From Figure 33(a) the triangular array requires a noticeably smaller voltage for operation. This should be expected since the distance between any active nozzles is 1 in. or more. The lack of dependency on the use of dummy nozzles is however unexpected and at present unexplained.

Figure 33(b) shows the improvements again made with the dummy nozzles with respect to the overlap ratio. Although the triangular geometry exhibited the worst behavior with no dummy nozzles, an overlap ratio approaching 1 was obtained with dummies employed in the array. Further improvements may be possible with additional dummies placed near the apex of the triangle.

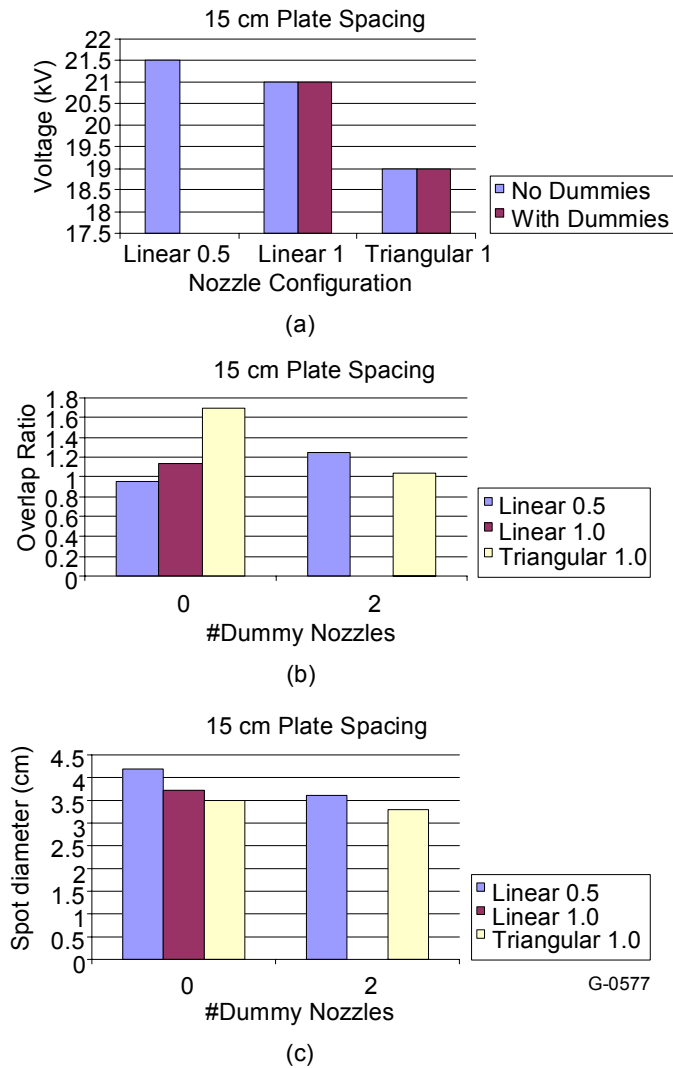


Figure 34. Various characteristics of a three-nozzle system

Figure 33(c) shows a decreasing spot diameter trend with the number of dummy nozzles similar to the two-nozzle system. Here again the triangular system appears to form the smallest spot size.

Three-Nozzle Summary

- The triangular nozzle geometry requires the least amount of voltage to operate.
- The overlap ratio improves and the spot diameter decreases with the use of dummy nozzles.
- Charge instabilities similar to the two-nozzle system made linear arrays marginally unstable depending upon the process conditions.

7.2.4 Capillary Tube Evaluation for Electrospinning

Experiments were run to evaluate the use of glass capillary tubing as means for self-regulated flow in the electrospinning process. Two different capillary tubes were utilized: one with an ID of 0.5 mm, and one with an ID of 1.35 mm.

The polymeric solution that was used in the evaluation was a 17% Estane (#58245) in a 90/10 DMF/NMP with the following characteristics:

<u>Viscosity (cP)</u>	<u>Solution Conductivity</u>
2125 cP	4.3 μ S/cm

From a viscosity prospective, this solution seemed “middle-of-the-road” for our applications with PAN and CP2 solutions in the 5 to 200 cP range and the Pall Filter solution above 9000 cP. It also allowed a slow enough flow rate for accurately performing the measurements taken.

The equilibrium height that liquid could theoretically achieve in a capillary is based upon the following equation,

$$H_{eq} = 4 \times \gamma \times \cos(\theta) / \rho \times g \times D$$

where γ is the surface tension (~ 36 dyne/cm, DMF=35.2 and NMP=45.8), θ is the contact angle (assumed 0 deg for our initial calculation), ρ is the density of the solution (0.97 g/cm^3), and D is the capillary diameter. For the two different diameter tubes, the heights were calculated to be

<u>Tube ID</u>	<u>H_{eq}</u>
0.5 mm	30.0 mm
1.35 mm	11.2 mm

The higher fluid level in the smaller diameter capillary allows longer capillary tubes to be used. This makes practical implementation of the technology more favorable from both a mechanical fixturing and a fluid-monitoring standpoint. As such, the experiments that follow focused on using the smaller ID capillary tube. The larger ID tubing was used to verify general trends.

The experiments were constructed around determining the fluid flow rates and ultimately whether stable electrospinning could be achieved. For flow rate determination, the typical experimental setup included inserting a capillary tube vertically into a 20 ml vial filled with the Estane solution. A ruler was placed next to the tube so capillary height measurements could be taken. No special preparation was done to the capillary tubing prior to use (i.e., used right out of the box). The capillary was inserted such that a 5 mm length of the tube was below the vial's fluid level. The total tube length was approximately 5 cm except where noted. The capillary fluid would slowly rise inside the tube once inserted. When the capillary was filled to the level

of the vial's fluid, a stopwatch was started. The capillary fluid's height above the vial's fluid level was recording against time in order to get a sense of the flow rates involved.

The electrospinning setup was constructed with a metal wire inserted into the glass capillary (see below). The assembly was then was placed into a vial filled with the Estane solution similar to above. The wire was moveable and generally the tip was placed level with the top of the capillary as a starting point. An aluminum weighing dish was placed directly above the capillary at various distances to evaluate initiation and stability of the electrospun deposit. The capillary wire was connected to the positive voltage of the DC supply with the aluminum dish grounded. Voltage was slowly increased on the wire until electrospinning was seen. If no response was observed, the wire would be moved up or down until electrospinning characteristics were initiated.

7.2.4.1 Experiment #1

Four different trials were done to evaluate fluid flow within a 0.5 mm ID capillary. The first trial was run as indicated above, simply recording capillary height vs. time. The second and fourth trials were run with a 375 μm OD and a 100 μm OD stainless steel wire respectively inserted into the tube: all the way to the end of the capillary. The third trial used the same tube as trial two except with the wire removed and the polymer solution drained only down to the 0.6 mm mark. The results are shown below in Figure 34.

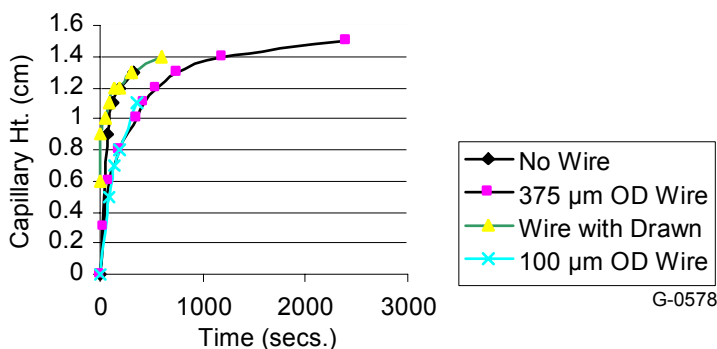


Figure 35. Capillary height vs time for 0.5 mm diameter capillary

Several characteristics are noted in the data:

- An exponentially decreasing flow rate
- A wire inserted in a capillary tube appears to decrease the equilibrium height of the tube
- The equilibrium height, as calculated for this tubing, appears incorrect
- Data appears repeatable, albeit a small sample size.

Falling short of the theoretical equilibrium height and the decrease in height with a wire inserted into the tube can both likely be attributed to the assumption of a zero degree contact angle. Visually it was observed that this angle was indeed non-zero and likely changed with a metal wire inserted.

7.2.4.2 Experiment #2

Trial 1 of experiment #1(no wire) was repeated using a 1.35 mm ID tube. The results are compared against those of the 0.5 mm capillary used in Experiment 1 above. See Figure 35.

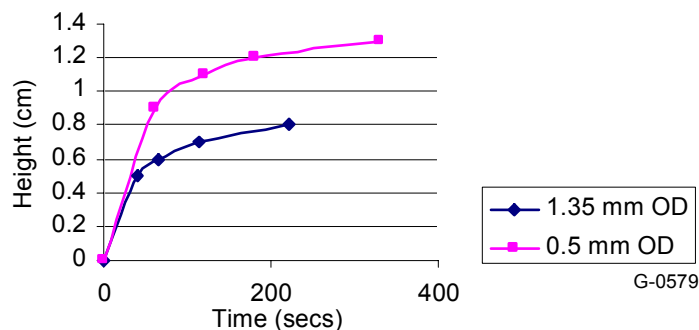


Figure 36. Comparison of capillary height vs time for a 1.35 mm and 0.5 mm diameter capillary

The trend is as expected for the larger diameter capillary. Both the equilibrium height and the flow rate appear to be lower (the H_{eq} is again lower for the reasons stated in experiment #1).

7.2.4.3 Experiment #3

In order to move towards higher and more controllable flow rates, a shorter capillary was tried. As such a 0.5 mm ID capillary was cut into 1 cm long tubes. This length was still reasonable to mechanically handle. The time it took to reach the 1cm mark with and without a 100 μ m OD SS wire inserted was recorded. This experiment was then repeated in a second trial. See Figure 36.

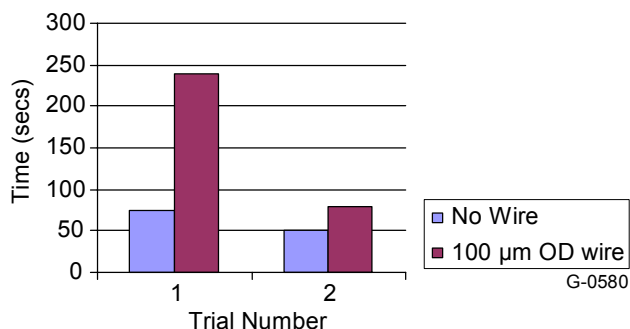


Figure 37. Time to reach 1 cm height in a 0.5 mm ID capillary

Although the trend is the same in the above data as previously noted, i.e., slower flow rates for the capillaries with an inserted wire, the repeatability for the wire-inserted capillaries had a large variation. One observation regarding this issue was that in the slowest flow capillary, more of the inserted wire was resting directly against the glass tubing than was noted in the other capillary. This possibly created more resistance to flow.

Assuming a linear flow through the 1 cm capillary, the best-case flow rate through a capillary with an inserted wire for our data would be,

$$\frac{\pi \times R^2 \times L}{t} = 0.09 \text{ ml / hour}$$

using $R=0.025$ cm, $L=1$ cm, and $t=75$ seconds. This flow still falls significantly short of our typical electrospinning rates of 0.25 to 1.0 ml/hour.

7.2.4.4 Experiment #4

Electrospinning was attempted from a 1 cm long, 0.5 mm ID capillary tube using a 100 μm OD SS wire. The target distance from the tip was 4 cm. The voltage was increased slowly to ~ 30 kV at which point some sporadic “spitting” of solution occurred. No sustainable cone was formed.

A copper wire (250 μm OD) was inserted in place of the SS wire without success: no electrospinning was observed. It was noticed that the end of copper wire was “mushroomed”, likely due to cutting. The wire end was lightly sanded to remove the debris and subsequently re-tried. Although sporadic electrospinning was seen, no improvement over the SS wire was achieved.

7.2.4.5 Conclusions

The equilibrium value calculated for the height of the capillary was never reached due mainly to the assumption of a zero degree contact angle. Indeed it was visually noted to be nonzero. It is also likely that the contact angle is responsible for the apparent reduction in height when a metal wire was inserted into the capillary.

An exponentially decreasing fill rate was observed in all cases. This characteristic is validated in the technical literature, e.g., by Schaffer and Wong (Phys. Rev. Letters April 6, 1998). This paper additionally describes a phenomenon called “pinning” or “contact line pinning”. This effect is similar to a drop of water on a window that appears to flow erratically enduring a stick-slip process on the way towards the ground. A variety of sources have been linked to this phenomenon including cleanliness, humidity, and glass surface roughness. These sources could account for the variation seen in Experiment #3 above.

The inability to generate a stable cone is troubling. Certainly one reason would be the low flow rates obtained even with the shortened nozzle length from Experiment #4. The effect of not having the ability to form a sessile drop at the end of the capillary due to surface tension effects may also limit the operation.

It therefore does not appear that this technique of self-regulated flow is viable for electrospinning.

8. Issues Affecting Scaleup

Our goal at this time was to investigate the factors necessary for scaling-up the electrospinning process. In particular the electrospinning of Estane was determined to be the weakest link and therefore was the focus of our efforts.

Estane solutions were electrospun using a range of nozzle diameters to determine the optimal size for producing fine, droplet free fibers. The finest nozzle used, 0.006 in. ID, produced the smallest droplets, but it did not eliminate them. Additional process parameters were evaluated for their effect on droplet count: voltage, distances between the target and nozzle, and solution flow rates. While the voltage and distance together had a strong influence on the deposition rate and the appearance of the fibers, they did not seem to affect the number of droplets created. It was concluded that low flow rates are useful for reducing droplet generation and for reducing fiber diameters. However, as noted in previous reports, a low flow rate makes scale-up to adequate production rates more difficult.

Our next approach was to incorporate polyaniline-camphorsulfonic acid (PANi-CSA) into the Estane solution in an attempt to reduce the fiber diameter and increase the flow rate. Approximately 0.6% PANi-CSA was dissolved in an Estane solution and electrospun to produce droplet free fiber mats where the fiber diameter was on average 40% finer than the un-modified Estane solution.

Tasks Completed and Reported

1. Develop ESD-safe syringe pump
2. Optimize electrospinning nozzle diameter
3. Optimize electrospinning distance, voltage and flow rate
4. Evaluate alternative pumping method
5. Evaluate effect of electrical conductivity.
6. Quantified relationship between flow rate and droplet concentration
7. Produced samples for moisture permeability testing by DMPC
8. Performed mechanical testing on electrospun membranes.

8.1 Develop ESD-safe Syringe Pump

The syringe pumps currently used for electrospinning at PSI are sensitive to high electric fields and ESD, so must be connected to the electrospinning nozzle via a long plastic tube. They also cannot be used with highly conductive solutions where a high voltage can be present in the syringe. To overcome these limitations, I built a simple syringe pump that has no sensitive electronics and is made almost entirely of non-conductive materials. This pump can be used directly to dispense the Estane solution into the electrospinning nozzle, thus eliminating several feet of tubing from the system. It is also safe to use with conductive solutions and can be operated in the presence of voltages as high as 25 kV. It can dispense between 1.2 and 65.6 ml/hr, so it cannot run at the low rates often used with the other syringe pumps. A motor with a higher gear ratio could be used to drop the rate if necessary.

8.2 Optimize Electrospinning Nozzle Diameter

To date, all electrospinning of Estane at PSI has been done with approximately 0.050 in. ID stainless steel nozzles. No effort had yet been made to evaluate the effect of nozzle diameter on electrospun fibers, so this was undertaken in the beginning of this report period. Two inch long dispensing needles from McMaster Carr in the following sizes (Table 3):

Table 3. Nozzle Gauges and Diameters

Gauge	ID (inches)
5	0.189
10	0.106
15	0.054 (closest to PSI nozzles)
20	0.0235
25	0.016
30	0.006

These needles have luer-lock fittings and the tubes are cut normal to the tube axis and deburred – not beveled and sharpened like injection needles. The Estane solution flows through all gauges, but quite a bit of pressure is necessary to force it through the 30 gauge needle.

Four samples of Estane were electrospun from a solution of 19% Estane in a mixture of 90% dimethylformamide (DMF), 10% n-methylpyrrolidone (NMP) using the following conditions (Table 4). The products were then inspected in the SEM to look for relationships between needle diameter and electrospun fiber morphology.

Table 4. Conditions of Sample Production

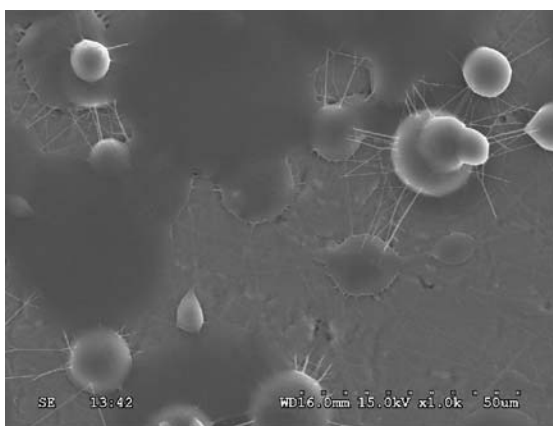
Sample	Needle (Ga)	Voltage (kV)	Distance (cm)	Pump Flow Rate (ml/hr)
1	15	15	20	1.78
2	20	12	20	1.78
3	25	12	20	1.78
4	30	12	20	1.78

As much as possible, the voltage, distance and flow rate were held constant. The larger needle seemed to produce a stable Taylor cone at 15 kV instead of 12 kV as used for all other sizes. Also, the flow rates are calculated from the motor rotational speed. This does not account for mechanical deflection of the pump mechanism or syringe plunger – this is assumed to be constant across all needle gauges. It was found in later experiments that the syringe deflection is significant at smaller diameters. It is estimated that the actual flow rate for the 30ga needle is closer to 1.2 ml/hr.

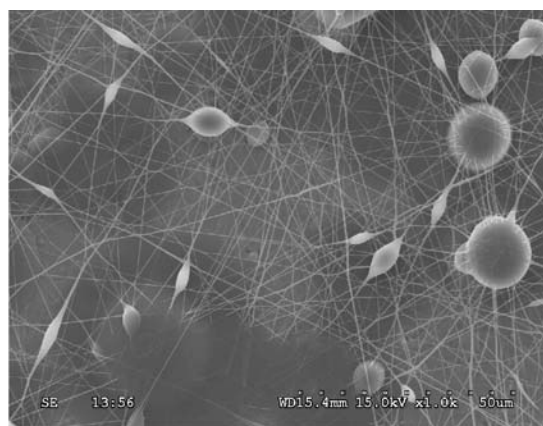
A 5 ml syringe was loaded with 1.5 ml solution and the samples were all produced within the following hour.

Observations from SEM inspection of electrospun samples shown in Figure 37.

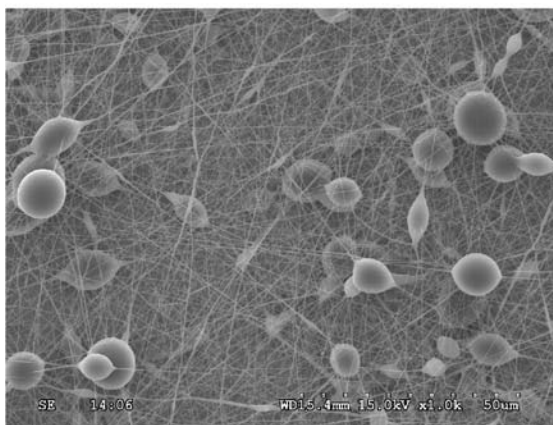
1. The number of droplets seems to be directly related to nozzle size.
2. The droplet size may be directly related to needle size, see Figure 38.
3. The coarsest needle produced a polymer film – very few droplets and even fewer fibers were produced. Perhaps this was more of a spray – the droplets have a much lower surface area to volume ratio, so they probably did not get the chance to dry enough before hitting the target surface.
4. The fiber diameters in all samples were between 50 nm and 1000 nm, most fibers were between 100 nm and 300 nm. There appears to be no correlation between nozzle diameter and fiber diameter. Some dimensional measurements of the fibers and droplets were taken on the 1000x SEM images using NIH ImageJ (<http://rsb.info.nih.gov/ij/>).



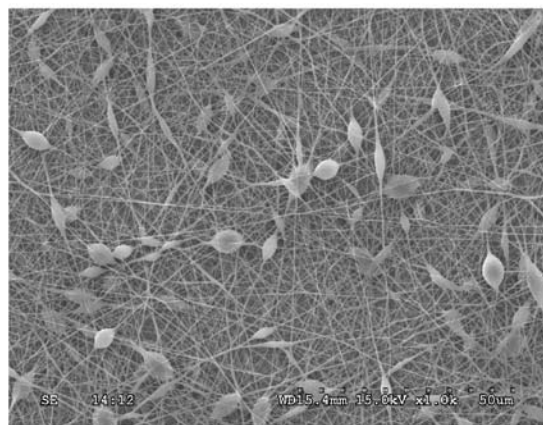
Sample 1. 15 Ga Needle



Sample 2. 20 Ga Needle



Sample 3. 25 Ga Needle



Sample 4. 30 Ga Needle

G-6427

Figure 38. SEM images of electrospun Estane showing effect of nozzle diameter

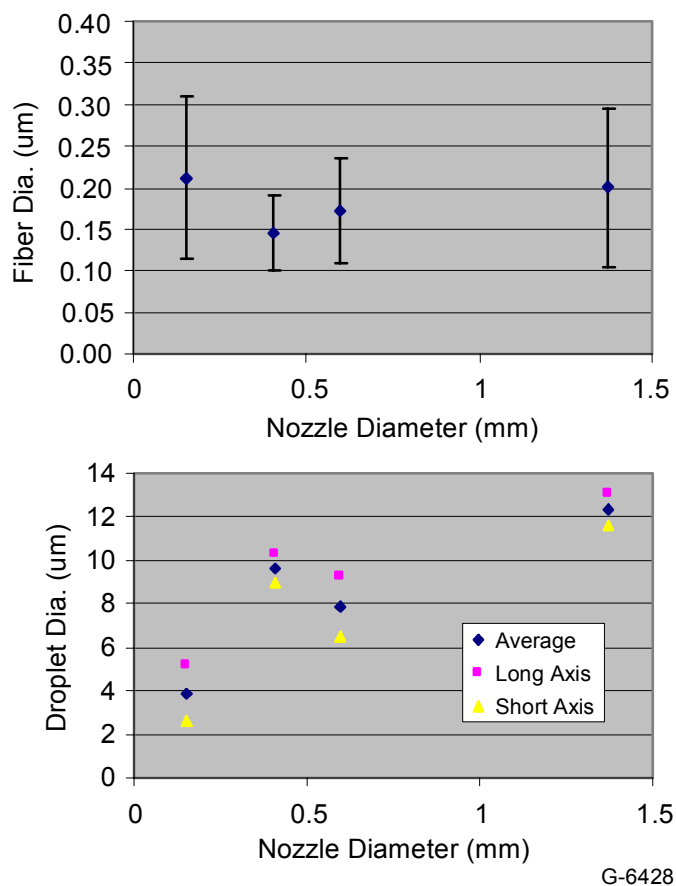


Figure 39. Relationships between nozzle, fiber and droplet diameters

Error bars in the Figure 38 diameters represent ± 1 standard deviation. Note the decrease in droplet aspect ratio, indicated by the difference between the long axis and short axis diameters. As the nozzle diameter decreases, droplets become spindles. Smaller nozzle diameters may produce finer spindles and possibly no spindles or droplets at all. However, due to the high viscosity of the Estane solution pumping through finer nozzles may not be practical.

Optimize Voltage, Distance and Flow Rate

The effect of voltage, distance and flow rate was studied to identify optimal operating conditions. The above nozzle diameter experiment was not performed under optimal conditions, so improvements in electrospun deposit morphology was anticipated.

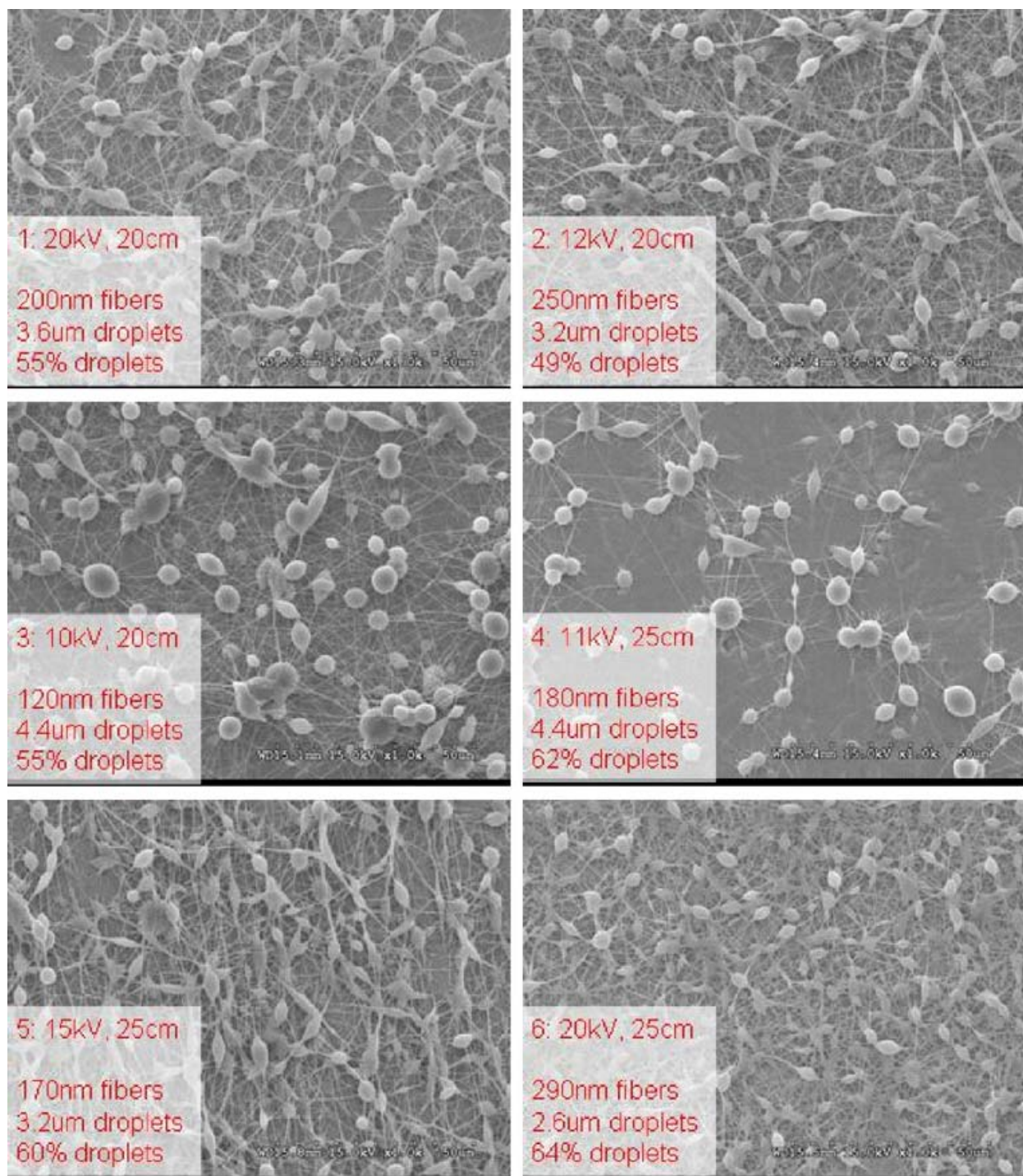
A solution of 19% Estane in a mixture of 90% dimethylformamide (DMF), 10% n-methylpyrrolidone (NMP) was prepared and filtered to 10 microns. The solution was then loaded into a 5 ml syringe fitted with a 30 gauge syringe needle. The following conditions were used to produce samples which were inspected by SEM (Table 5). Samples are shown in Figures 39 through 41.

Table 5. Process Optimization Sample Conditions

Sample	Voltage (kV)	Distance (cm)	Flow (ml/hr)	Observations
1	20	20	1.2	Multi-fiber, arcing to pump
2	12	20	1.2	Small stable cone at nozzle
3	10.2	20	1.2	Large stable cone at nozzle
4	11.3	25	1.2	Large stable cone at nozzle
5	15	25	1.2	Arcing to camera, unknown nozzle condition
6	20	25	1.2	Arcing to camera, visibly unstable at nozzle
7	8.8	15	1.2	Large stable cone at nozzle
8	14	15	1.2	Small stable cone at nozzle
9	19.4	15	1.2	Multi-fiber, arcing to pump
10	20	20	1.5	Same electrospinning behavior as seen with samples 1-9. Syringe plunger deflecting substantially, indicating actual flow rate is lower than set rate.
11	12	20	1.5	
12	10.2	20	1.5	
13	11.3	25	1.5	
14	15	25	1.5	
15	20	25	1.5	
16	8.8	15	1.5	
17	14	15	1.5	
18	19.4	15	1.5	

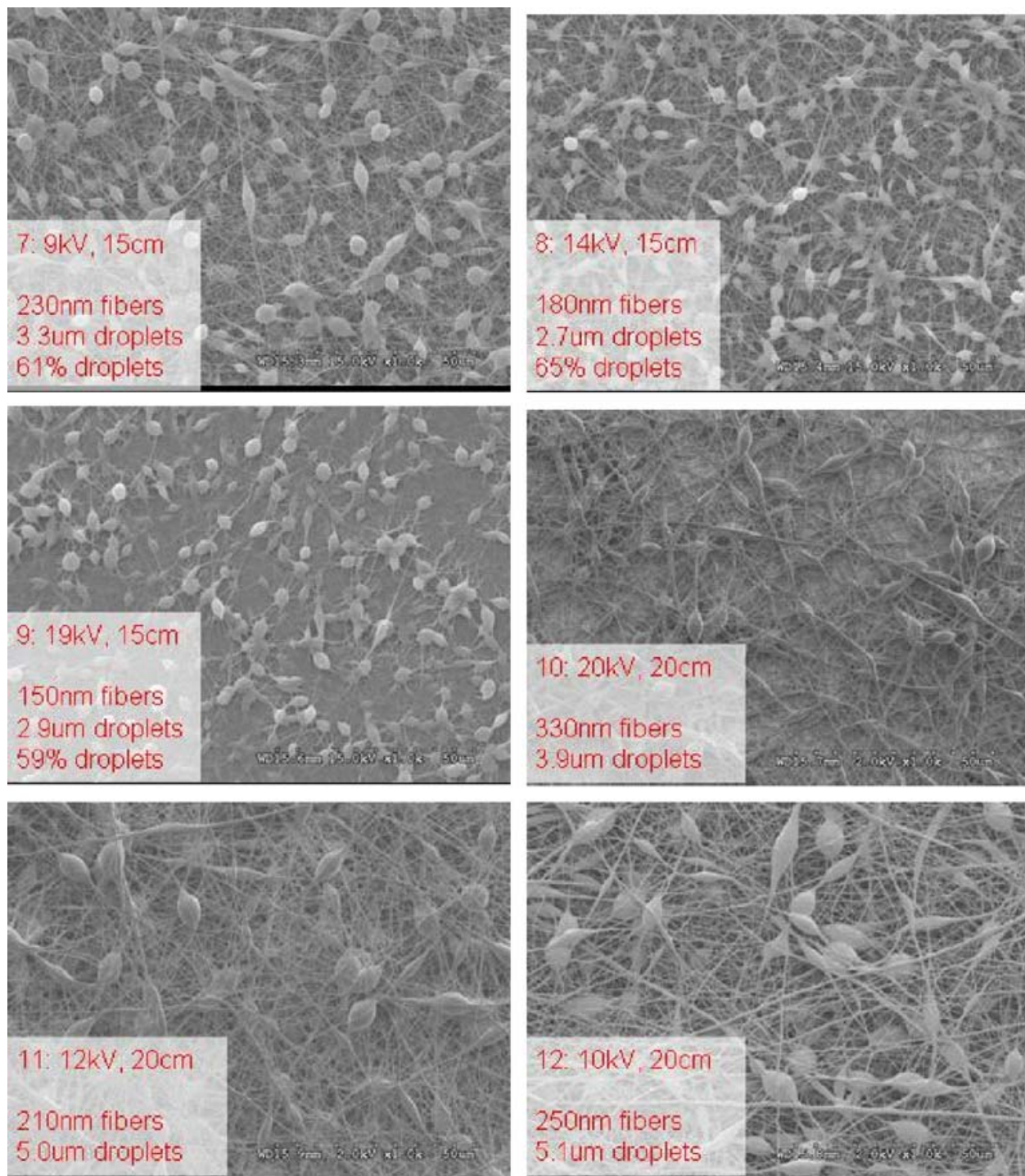
All samples were measured for droplet diameter (short axis) and fiber diameter using ImageJ. When possible, samples were also measured for area ratio of fibers to droplets. For this measurement, the images were thresholded to eliminate the background. The number of image pixels on fibers and droplets were counted as roughly the visible surface area of the deposited fibers and droplets. The image was then eroded to eliminate the fibers, leaving only droplets. Again the pixels were counted, and the ratio of droplet pixel count to the pixel count of droplets and fibers was calculated.

Samples 1 to 9 and 12 were gold coated prior to SEM inspection. All other samples were not coated in an effort to reduce sample preparation time. Slight charging in SEM was seen on uncoated samples. Images of uncoated samples could not be evaluated by same image analysis method to determine droplet area concentration.



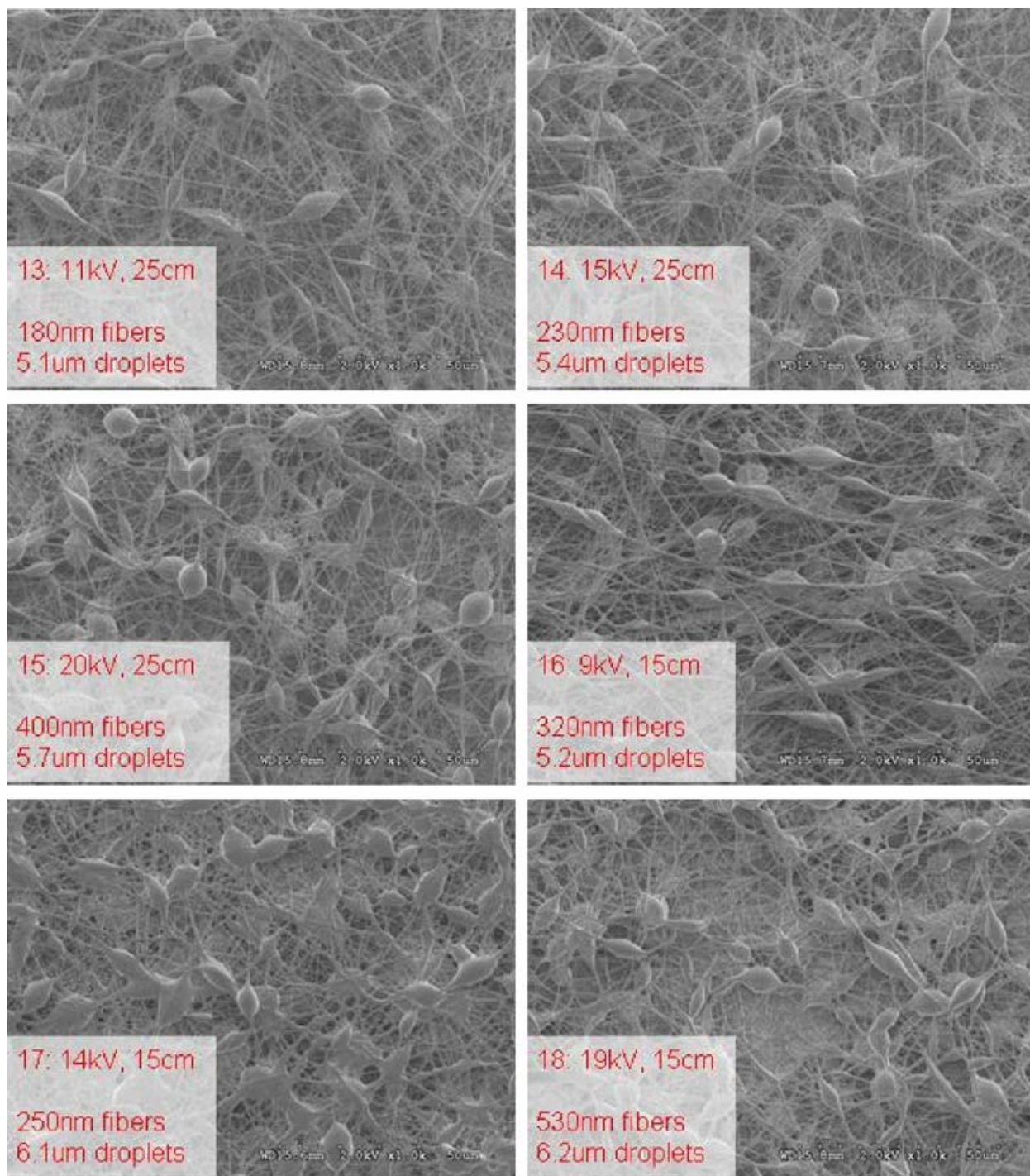
G-6429

Figure 40. Samples 1 through 6



G-6430

Figure 41. Samples 7 through 12



G-6431

Figure 42. Samples 13 through 18

Summary of SEM Observations, graphically represented in Figure 42.

- All samples had unacceptable amounts of droplets.
- Droplets in samples 10 to 18 were larger, indicating that *higher flow rate promotes droplet growth*.
- Lower field strength may result in finer fibers.
- Lower field strength may result in more consistent fiber diameters.

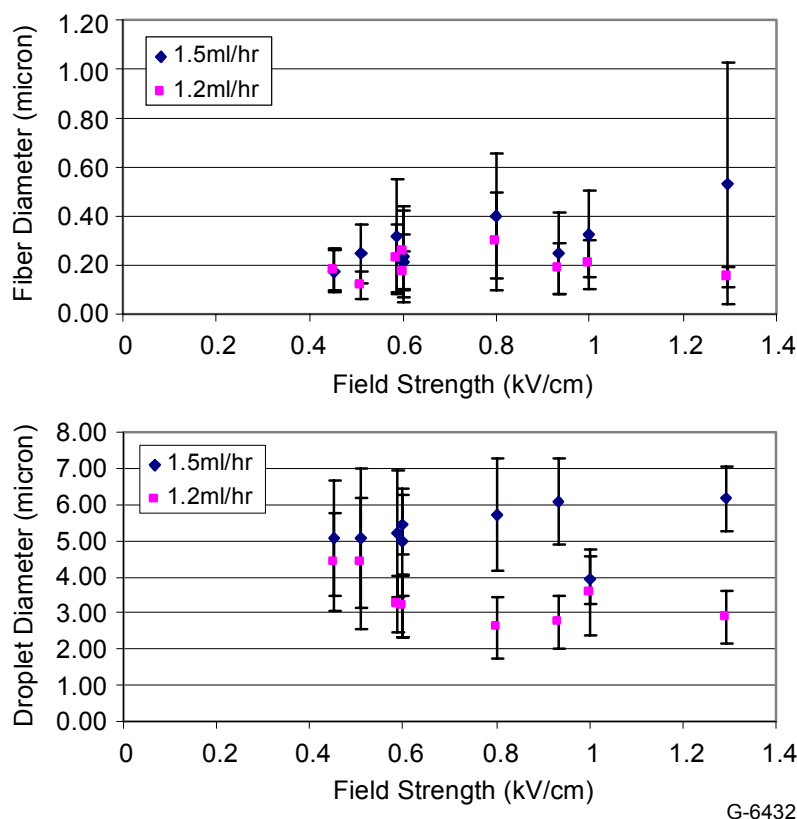


Figure 43. Relationships between field strength, droplet diameter, and fiber diameter

8.3 Evaluate Alternative Pumping Method

Based on these results, samples produced at lower flow rates were made and evaluated. The pump used in the above experiments can not run at less than 1.2 ml/hr, so the actual flow rate used in this experiment is not known. The solution was pressurized by operating the pump for less than 10 seconds at 1.2 ml/hr. Residual pressure was observed as the growth of a droplet at the end of the nozzle. A positive pressure was observed for at least 20 min after the pump was turned off. Samples were made for 20 min, during which the fiber spinning appeared stable, however no Taylor cone was visible. The fiber appeared to be spinning from a point within the nozzle.

As expected, the number of droplets was dramatically reduced by a large decrease in flow rate as shown in Figure 43. However, the nozzle conditions were not ideal; there was no visible Taylor cone and occasionally fibers were produced from multiple simultaneous jets (multi-jet mode). Further optimization of the electrospinning conditions were necessary, but limitations of the pump method called for modifications. The problems with syringe pumping of solution are:

- Sensitive electronics in commercially available pumps incompatible with high voltages used in electrospinning
 - Long tubing connecting syringe pump to nozzle is difficult to clean and further reduces maximum flow rate due to viscous drag.
 - Highly conductive solutions, such as PANi-filled solutions still present high voltage arcing problem, even with long tubing separating nozzle from pump.
- Custom-made pump not capable of pumping at very low flow rates
- Syringe plunger deflects at low to moderate flow rates, high flow rates impossible for viscous solutions such as used in this program.

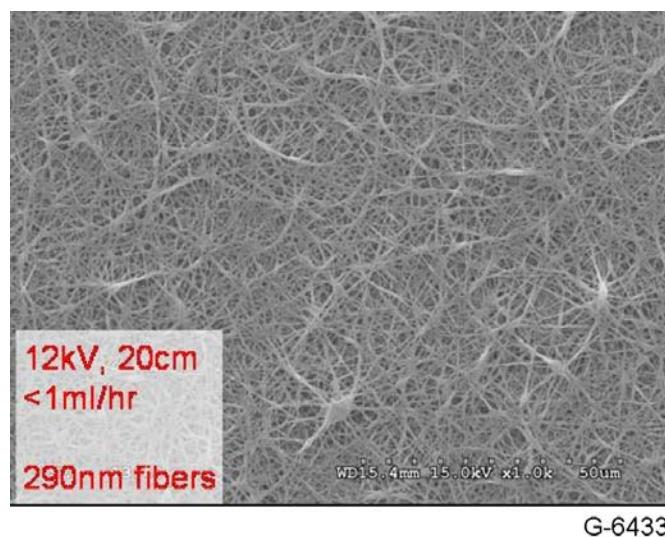
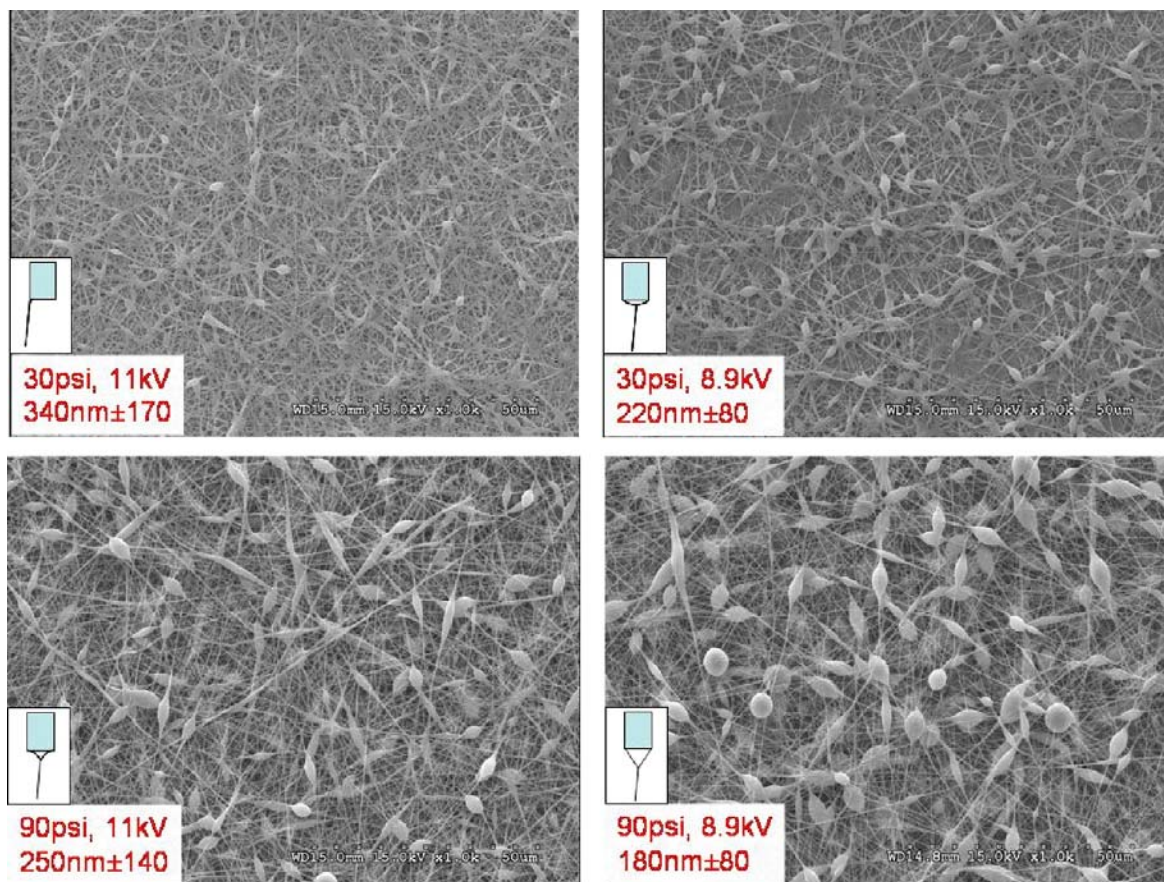


Figure 44. Low droplet concentration at very low flow rate

An alternative to the syringe pump was identified and evaluated in the following experiments. Instead of using a syringe pump, a pressure fitting is attached to the top of the syringe barrel which can supply 0 to 100psi of dry nitrogen. There are no conductive parts to which arcing can occur, making this system capable of operating at over 25 kV. For scale-up, it will be necessary to carefully control the solution viscosity as the flow rate is now strongly dependent on solution viscosity.

First, an evaluation of the effect of nozzle conditions on the electrospun product was performed. The distance was held at a constant value of 20cm, and the voltage and pressure were varied to control the shape of the solution drawn from the nozzle tip. The above experiment showed that a complete lack of a visible Taylor cone resulted in a low droplet concentration. This was confirmed as shown by Figure 44.



G-6434

Figure 45. Effect of electrospinning jet initiation shape

As the size and shape of the electrospinning cone approached that of a traditional Taylor cone, the size and number of droplets increased. While it is encouraging to be able to reproducibly create fibers with few or no droplets, there is some concern that the necessary nozzle tip condition is inherently unstable and unamenable to scale-up.

8.4 Evaluate Effect of Electrical Conductivity

A set of samples were produced of Estane + polyaniline-camphorsulfonic acid (PANi-CSA) to evaluate the effectiveness of PANi in reducing droplet size and count. It has been shown in numerous papers that solution conductivity is a strong factor in determining fiber diameter. It has also been shown that conductivity is an important factor in determining droplet size in electrospraying. PANi has been used extensively in this lab to control electrical conductivity with very low (<1%) concentrations. Table 4 contains the results of conductivity measurements taken on solutions prepared in this experiment. Note the nearly 30x increase in conductivity of the Estane solution due to the addition of less than 1% PANi-CSA.

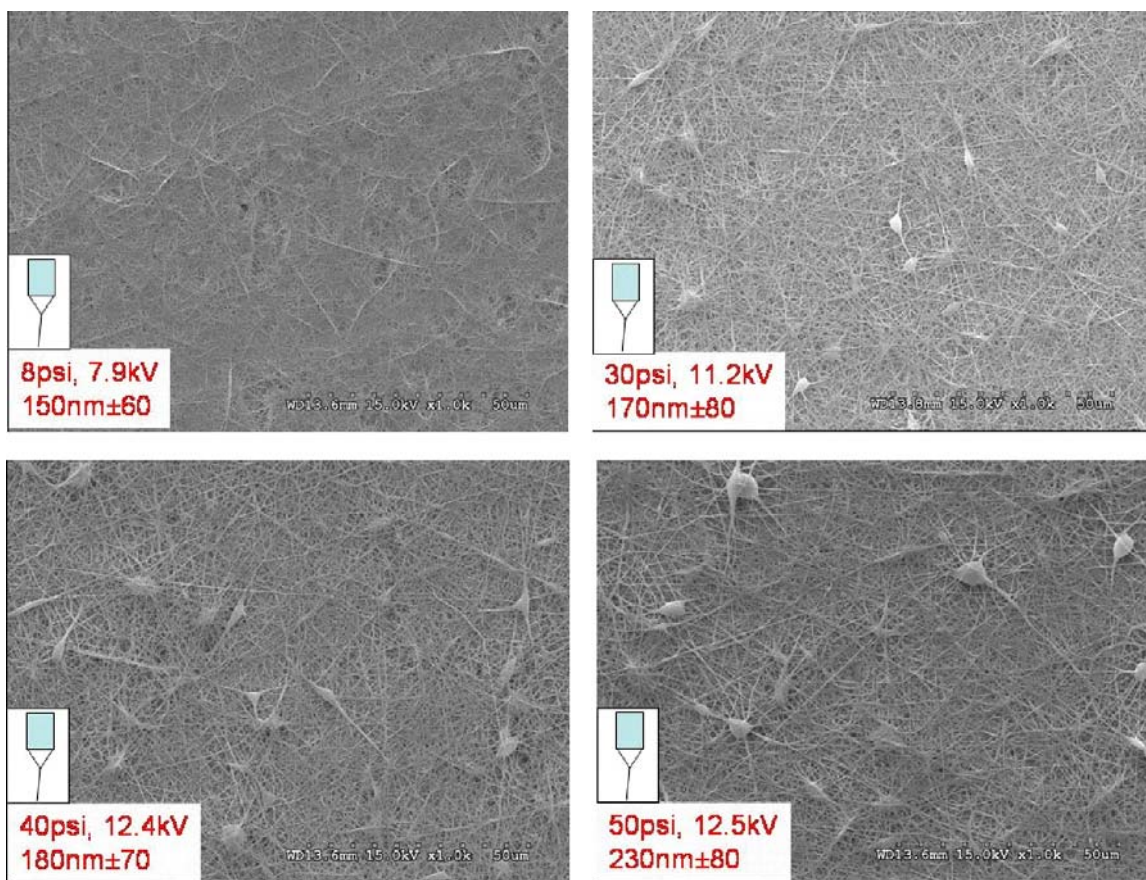
Table 6. Comparison of Electrical Conductivity

Solution	Conductivity ($\mu\text{S}/\text{cm}$)
19% Estane	6.7
0.26% PANi	27
0.6% PANi-CSA	451
19% Estane + 0.6% PANi-CSA	187

PANi has a very low solubility in DMF and NMP, PANi-CSA typically is even less soluble. The preparation method used in this experiment was designed to optimize solution concentration and conductivity but took several days to complete. First a 90% 100g of DMF/10%NMP with 1% by weight PANi was mixed in for 24 hours at room temperature with a magnetic stir bar. An unknown amount of PANi dissolved, leaving a dark blue solid residue of the remaining PANi. The solution was filtered through glass wool, a 5 micron filter and finally through a 1 micron filter. Two grams of the remaining dark blue solution was poured into a tared aluminum weighing dish and dried in a 100°C vacuum oven over night (>14 hours). The dish and blue residue (PANi) were re-weighed to determine the PANi concentration of the filtered solution. A 100 g, 16.6% by weight solution of CSA in the same DMF/NMP solvent mixture as above was prepared and filtered to 1 micron. Next a 1.3:1 weight ratio of CSA to PANi was added drop-wise to the stirring PANi solution and allowed to mix for 4 hours. Finally 19% by weight Estane was added to the PANi-CSA mixture and stirred overnight.

For the following samples, the PANi concentration was 0.26%. This translates to 0.076 g PANi in 30 g of solution. At 1.3:1 CSA: PANi, 0.099 g CSA was required. Using a 16.6% CSA stock solution, 0.596 g of solution was added. Approximately 3 ml was decanted for a measurement of its conductivity. Finally, 6.3 g of Estane was added to the remaining 26.9 g of PANi-CSA solution and mixed overnight. The final product was a transparent blue-green solution. Two milliliters of the solution were carefully dispensed into a 5 ml syringe which was then fitted with the pressure adapter and a 30ga nozzle. The samples were produced by 20 min of electrospinning. In all cases, the process was extremely stable. There were no visible changes or fluctuations in the nozzle condition observed during the entire 20 min. SEM images of the samples are provided in Figure 45.

As in previous experiments, higher flow rates promoted larger droplets; however it appears that PANi-CSA strongly inhibits droplet creation, even with a large Taylor cone. This will be of particular benefit when using the pressure controlled flow. The shape and size of the Taylor cone can be used as the control parameter for regulating the pressure. Samples produced without the PANi-CSA were only fiber-free when there was no visible Taylor cone. In this regime an actual measure of the solution flow would be necessary. As in the case of the syringe pumps, this type of measurement is complicated by the presence of very high voltages.



G-6435

Figure 46. Electrospun Estane-PANi solution

8.5 Quantified Relationship Between Pressure, Flow Rate and Droplet Concentration

Seven samples were electrospun onto tared aluminum weighing dishes, 6 cm in diameter. The spinning solution was 19% Estane 58245, 0.6% Pani-CSA in 90% DMF, 10% NMP. The samples were then weighed and inspected by SEM. Measurements were done with ImageJ (NIH) to determine droplet counts, and fiber and droplet sizes. The results are shown in Table 7 and Figures 46 through 48.

Table 7: Description of Samples

Pressure (psig)	Time (hr)	Deposition Rate (g/hr)	Fiber Diameter (μm)	Fiber Diameter stdev (μm)	Droplet Count	Droplet Diameter (μm)	Droplet Diameter stdev (μm)
30	1.00	0.0074	0.210	0.086	123	3.161	0.358
40	0.51	0.0113	0.220	0.077	58	4.467	0.656
60	0.50	0.0170	0.236	0.112	131	4.853	0.856
90	0.50	0.0258	0.258	0.092	129	6.107	1.372
20	1.60	0.0047	0.212	0.093	56	2.895	0.641
30	1.50	0.0075	0.178	0.054	75	3.473	0.544
40	1.13	0.0097	0.233	0.071	73	3.948	1.049

Two results to note are deposition rate seems to increase linearly with pressure, and the rate of increase of droplet cross sectional area increases with solution pressure. It is expected that the presence of droplets in a coating is detrimental to its breathability performance, so this effort has been directed towards lower droplet concentrations. This effort has also been driving towards higher deposition rates, so it appears it will be necessary to find a compromise between process throughput and permeability. However, it should be noted that the relationship between permeability and droplet concentration needs to be verified with experimental data.

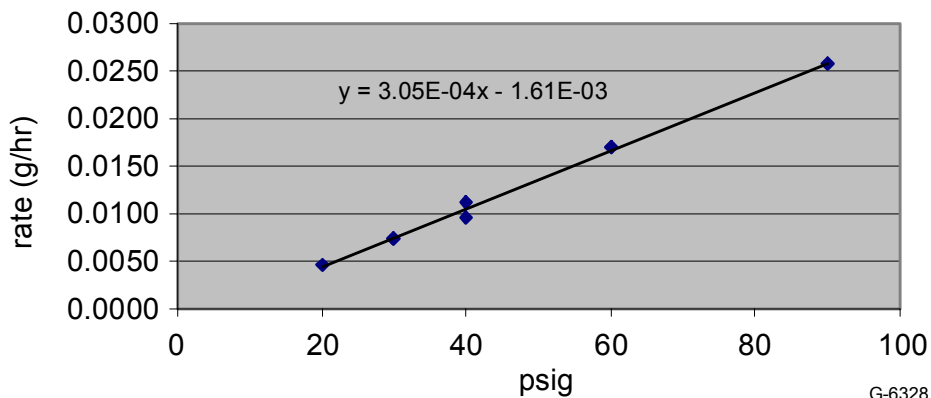


Figure 47. Deposition rate versus solution pressure

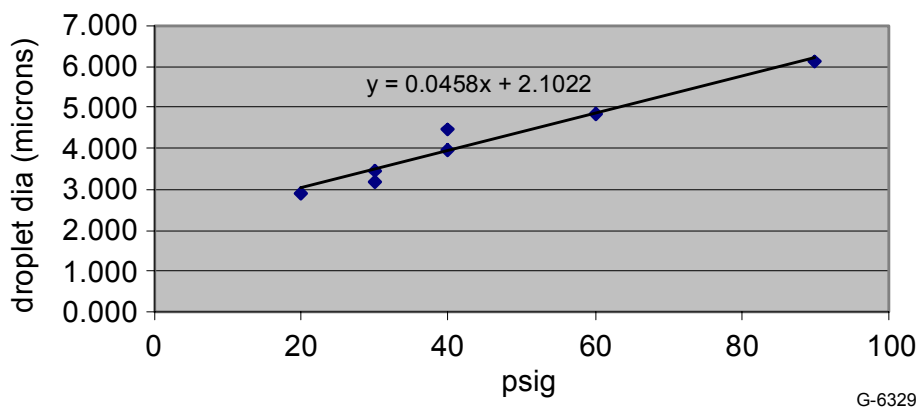


Figure 48. Droplet diameter versus solution pressure

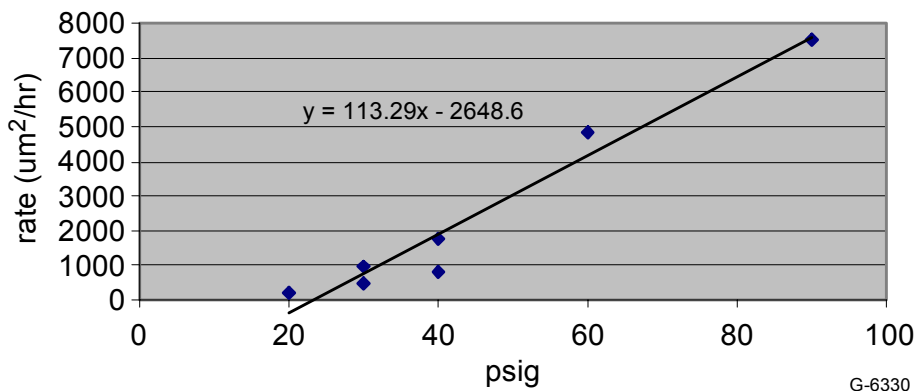


Figure 49. Droplet deposition rate versus solution pressure

8.6 Produced Samples for Moisture Permeability Testing

In the interest of scaling up the electrospinning process, a determination of control settings and tolerances was necessary. Control parameters of interest for this task were: solution pressure, voltage and time. Other factors such as the distance between the electrospinning tip and target and the polymer solution concentration and composition were not varied as they have been studied previously in this program.

Solution pressure, voltage and time could all easily be actively controlled by an automated, large-scale process, however it was not known what tolerances would be acceptable for the control system. Because moisture permeability is the most important product parameter, a comparison of process parameters and permeability performance would be most useful in determining the optimal parameter settings and tolerances. Additionally, as the permeability is most likely dependent on the morphology of the material, this data will be useful in the future if optimization of the polymer solution is necessary. SEM comparison of these samples versus future samples may enable prediction of permeability performance based on their morphology.

The samples listed in Table 8 were produced on 6 cm diameter aluminum weighing dishes and delivered to Dr. Heidi Schreuder-Gibson on 5/2004 for evaluation by Dynamic Moisture Permeability Cell (DMPC). The following pages of this section provide SEM images at 1,000x and 10,000x magnification of the samples prior to DMPC testing.

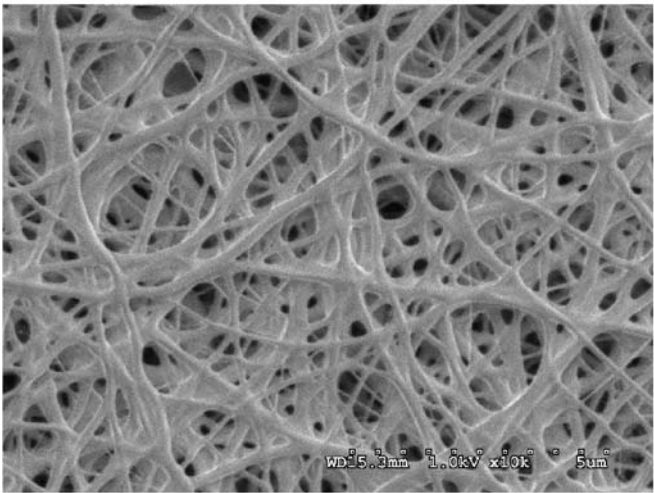
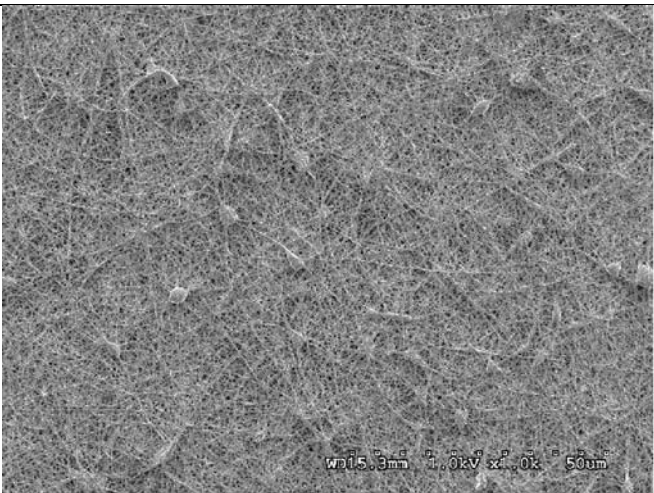
Table 8. List of Samples Prepared for Moisture Permeability Testing

Sample	Electrospinning Conditions				Droplet Diameter μm	Total Droplet Area μm^2	Fiber Diameter nm	Voltage kV	Distance cm	Pressure psig
	Voltage kV	Area Density g/m^2	Coating Weight g	Droplets/g $\mu\text{m}^2/\text{g}$						
1	14.6	20	20	3:09	6.8	0.019	49001	2.9	946	210
2	15.0	20	20	6:18	13.7	0.039	49001	2.9	1891	210
3	15.0	20	20	12:35	27.3	0.077	49001	2.9	3778	210
4	17.0	20	40	1:20	6.9	0.020	81307	4.2	1596	220
5	16.9	20	40	2:40	13.9	0.039	81307	4.2	3191	220
6	16.9	20	40	5:20	27.8	0.079	81307	4.2	6383	220
7	18.9	20	60	0:51	7.3	0.020	285089	4.9	5844	240
8	18.7	20	60	1:41	10.7	0.030	285089	4.9	8638	240

1	
Voltage (kV)	14.6
Distance (cm)	20
Pressure (psig)	20
Time (hr:min)	3:09
Area density (g/m ²)	6.8
Weight (g)	0.019
Droplets/g (μm ² /g)	49001
Droplet diameter (μm)	2.9
Total droplet area (μm ²)	946
Fiber diameter (nm)	210

Comments:

This is the lowest area density sample and has the lowest droplet concentration. Samples 2 and 3 were produced with the same droplet concentration, but for much longer times to yield higher area densities. Samples 4 and 7 have similar area densities to this sample.



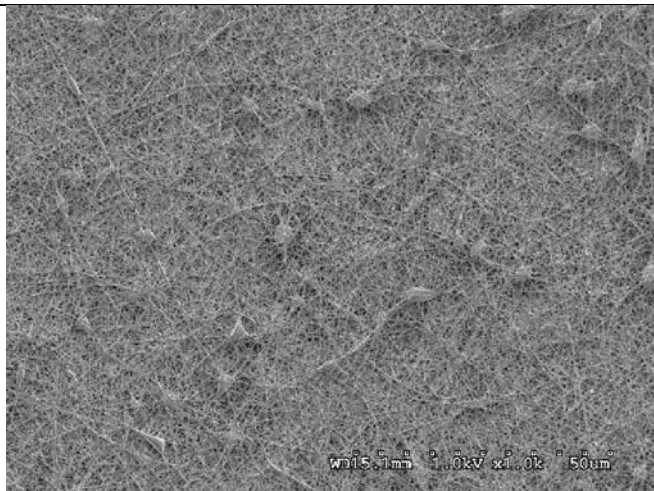
G-6331

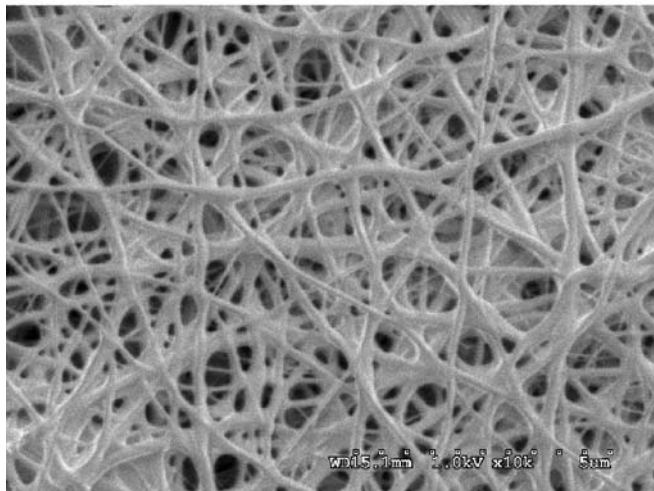
G-6331

2	
Voltage (kV)	15.0
Distance (cm)	20
Pressure (psig)	20
Time (hr:min)	6:18
Area density (g/m ²)	13.7
Weight (g)	0.039
Droplets/g (μm ² /g)	49001
Droplet diameter (μm)	2.9
Total droplet area (μm ²)	1891
Fiber diameter (nm)	210

Comments:

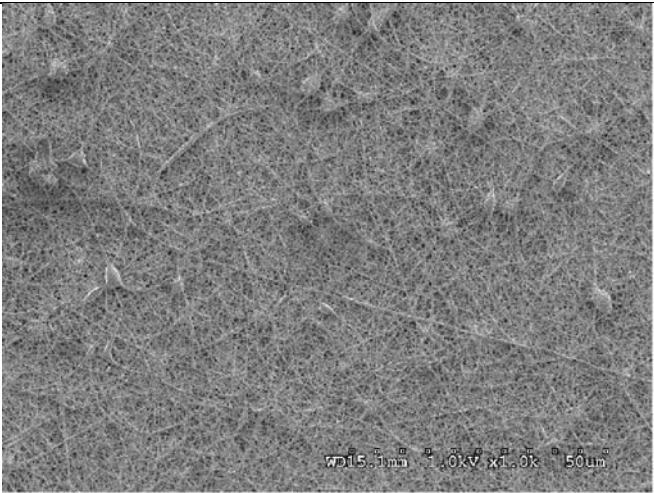
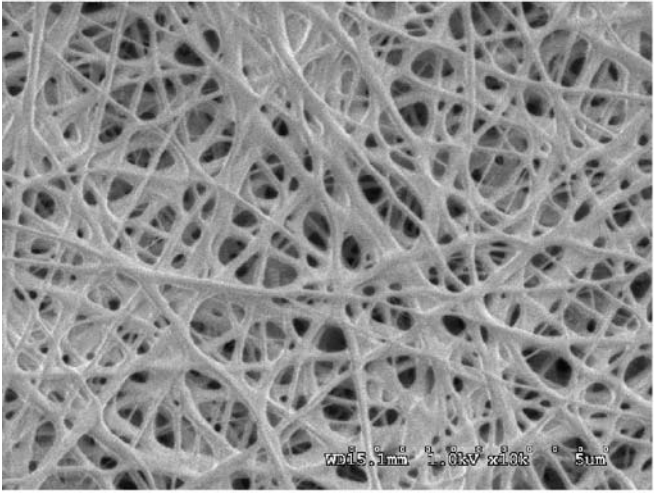
Used same conditions as for samples 1 and 3. This area density is as close as possible to samples 5 and 8.





G-6332

G-6332

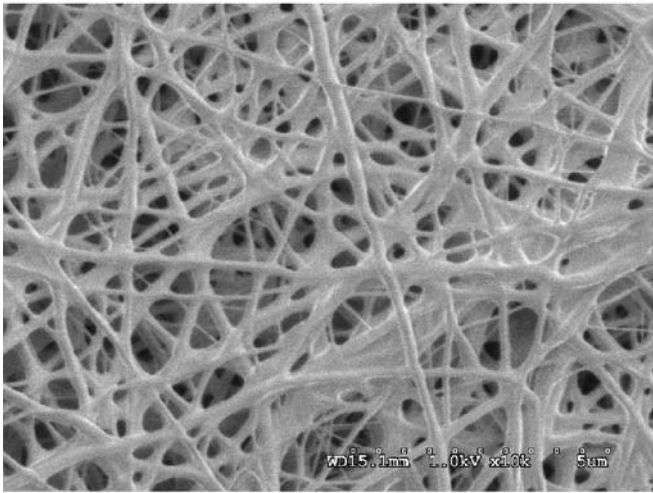
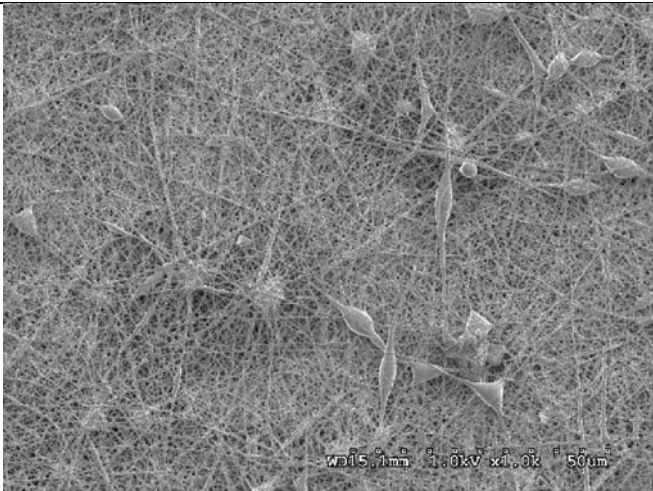
3		
Voltage (kV)	15.0	
Distance (cm)	20	
Pressure (psig)	20	
Time (hr:min)	12:35	
Area density (g/m²)	27.3	
Weight (g)	0.077	
Droplets/g (μm²/g)	49001	
Droplet diameter (μm)	2.9	
Total droplet area (μm²)	3778	
Fiber diameter (nm)	210	
Comments: This sample was produced with the same conditions but for a longer time than for samples 1 and 2. Sample 6 has a similar area density to this sample.		

G-6333

4	
Voltage (kV)	17.0
Distance (cm)	20
Pressure (psig)	40
Time (hr:min)	1:20
Area density (g/m ²)	6.9
Weight (g)	0.020
Droplets/g (μm ² /g)	81307
Droplet diameter (μm)	4.2
Total droplet area (μm ²)	1596
Fiber diameter (nm)	220

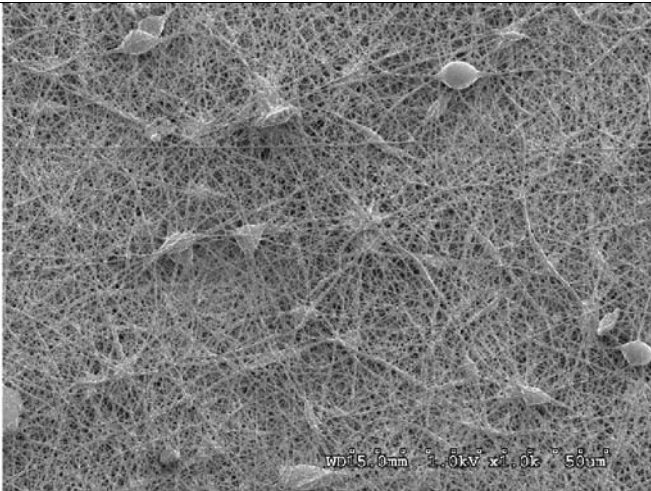
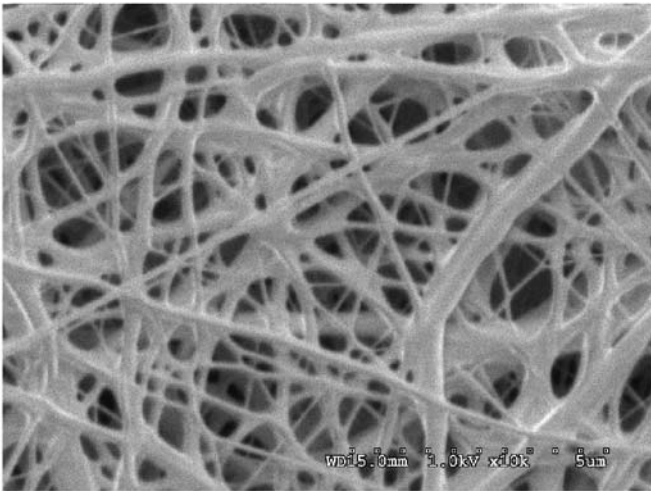
Comments:

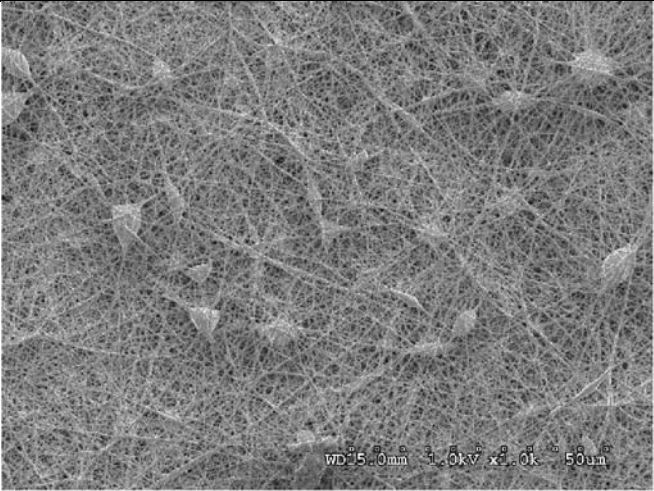
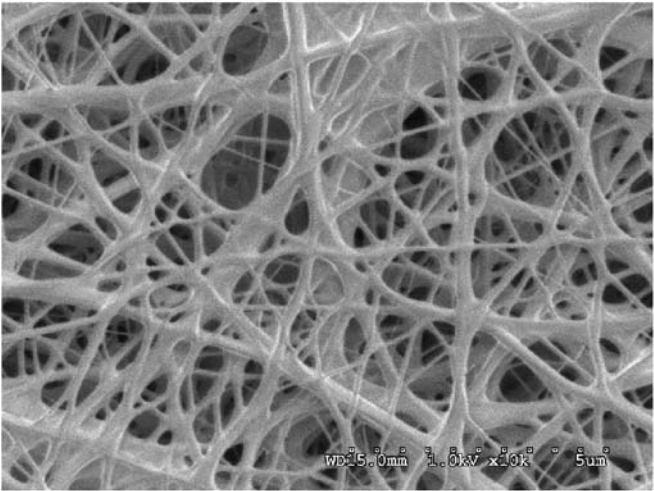
Samples 4, 5 and 6 were produced to contain a medium concentration of droplets. Samples 1-3 have low concentrations, and samples 7 and 8 have high concentrations. For each set of samples, the droplet deposition rate was constant, i.e., the fraction of droplets to fibers is constant.



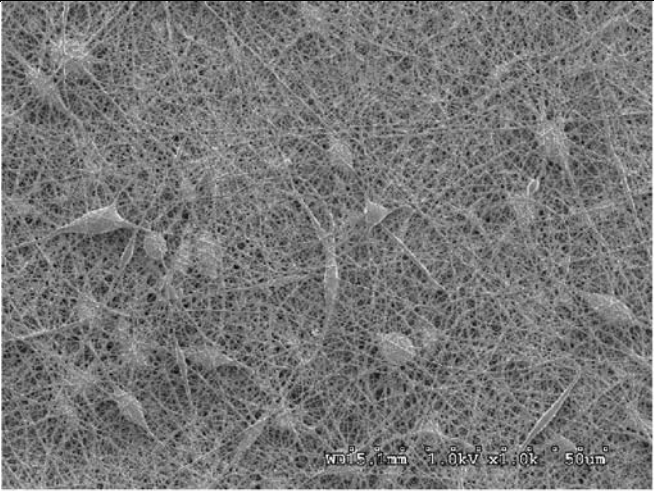
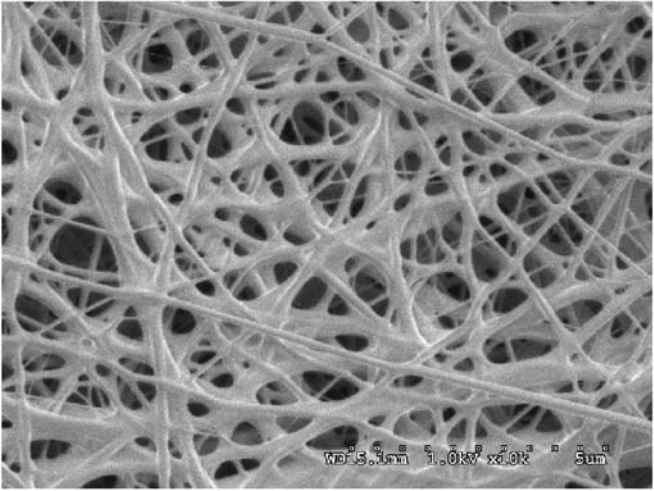
G-6334

G-6334

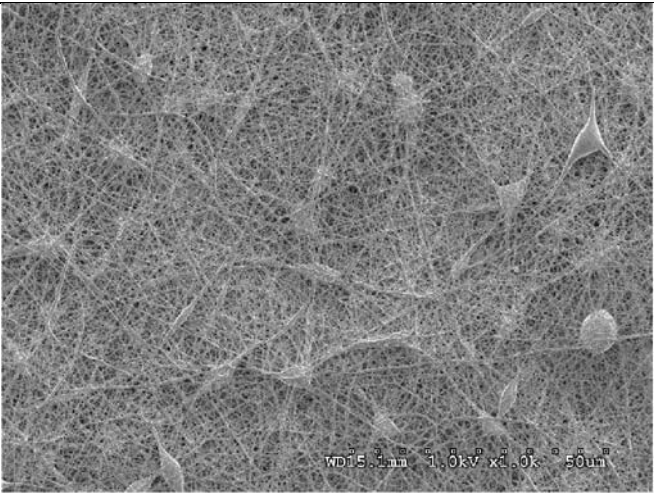
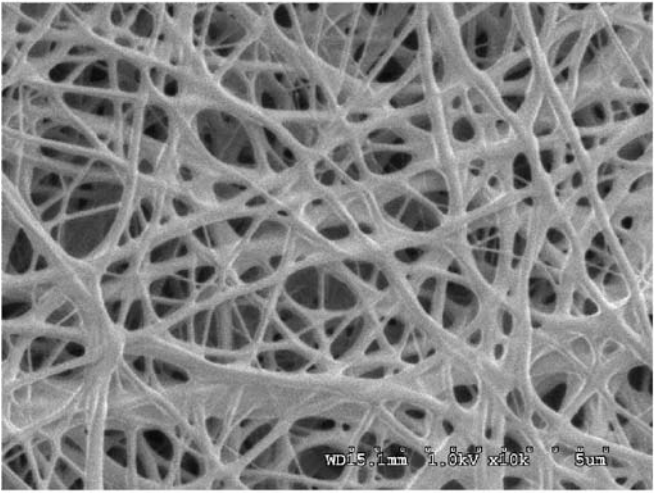
5		 
Voltage (kV)	16.9	
Distance (cm)	20	
Pressure (psig)	40	
Time (hr:min)	2:40	
Area density (g/m ²)	13.9	
Weight (g)	0.039	
Droplets/g (μm ² /g)	81307	
Droplet diameter (μm)	4.2	
Total droplet area (μm ²)	3191	
Fiber diameter (nm)	220	
Comments: See comments for sample 4.		G-6335

6		
Voltage (kV)	16.9	
Distance (cm)	20	
Pressure (psig)	40	
Time (hr:min)	5:20	
Area density (g/m ²)	27.8	
Weight (g)	0.079	
Droplets/g (μm ² /g)	81307	
Droplet diameter (μm)	4.2	
Total droplet area (μm ²)	6383	
Fiber diameter (nm)	220	
Comments: See comments for sample 4.		

G-6336

7		
Voltage (kV)	18.9	
Distance (cm)	20	
Pressure (psig)	60	
Time (hr:min)	0:51	
Area density (g/m ²)	7.3	
Weight (g)	0.020	
Droplets/g (μm ² /g)	285089	
Droplet diameter (μm)	4.9	
Total droplet area (μm ²)	5844	
Fiber diameter (nm)	240	
Comments: This is the lowest area density sample with the highest droplet concentration. Samples 7 and 8 were produced using the same conditions.		

G-6337

8		
Voltage (kV)	18.7	
Distance (cm)	20	
Pressure (psig)	60	
Time (hr:min)	1:41	
Area density (g/m²)	10.7	
Weight (g)	0.030	
Droplets/g (μm²/g)	49001	
Droplet diameter (μm)	4.9	
Total droplet area (μm²)	8638	
Fiber diameter (nm)	240	
Comments: This is a medium area density and droplet concentration sample. This set of 8 samples should provide sufficient information on the effects of area density and droplet concentration on the vapor permeability of electrospun Estane. A high area density and droplet concentration sample was not produced for this reason.		
		G-6338

8.7 Perform Mechanical Testing on Electrospun Membranes

An additional set of eight samples were produced using the same conditions used to produce the samples in Task 2. A ninth sample using the same conditions as for samples 1-3 was produced with a higher area density to further define the relationship between mechanical properties and area density. Two pieces of tape were placed across each sample, with the tape strips 9 mm apart. The samples were then each cut into six 8 mm wide, 9 mm long tensile specimens as shown in Figure 49.

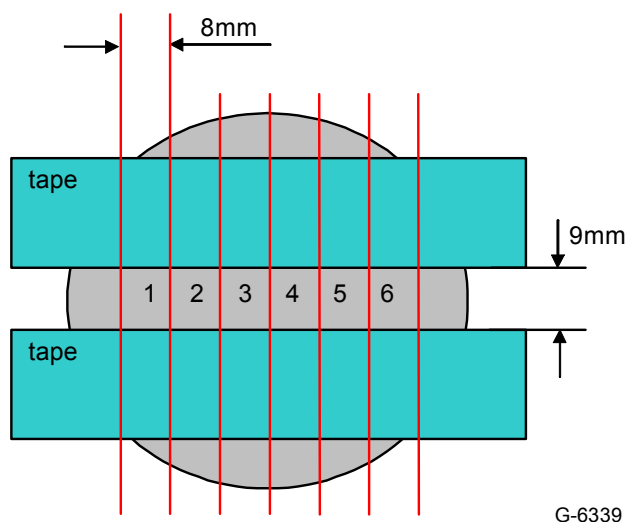


Figure 50. Tensile sample preparation

For tensile testing, manually operated grips were used to hold the taped sections of the samples in an Instron 4442 UTS. A strain rate of 5 mm/minute was used for all samples. Sample thicknesses were estimated as equivalent to a void-free film based on the coating weight, area and the density of Estane 58245 (1.21 g/cc). Results are provided in Table 9.

Table 9. Tensile Testing Samples

Sample	Coat Wt (g)	Avg. Max Elongation (mm)	Avg. Max Load (N)	Strength (kPa)	Area Density (g/m ²)	% Elongation
1	0.0234	17.18	5.47	9.91	8.3	91
2	0.0344	17.78	6.55	8.07	12.2	98
3	0.0732	14.97	11.71	6.78	25.9	66
4	0.0140	14.52	1.86	5.63	5.0	61
5	0.0417	16.94	4.71	4.79	14.8	88
6	0.0834	14.68	9.89	5.03	29.5	63
7	0.0204	16.24	2.17	4.50	7.2	80
8	0.0401	19.56	9.17	9.70	14.2	117
9	0.0958	12.22	12.19	5.40	33.9	36

Figures 50 and 51 show a dependence of strength and elongation on area density and droplet concentration. Strength and elongation of low droplet coatings decreases with coating thickness. Medium droplet concentration films show little dependence between area density and strength and elongation. High droplet concentration coatings show increasing strength and elongation with increasing area density. Perhaps the droplets reinforce the membrane by providing a greater number of connections between the fibers. To maintain adequate CBD protection, tears must be prohibited from propagating. These relationships indicate that there may be an optimal droplet concentration and/or size for mechanical performance. The above data also indicates that this material must be supported by a higher stiffness and strength material to prevent this material from elongating beyond approximately 50%.

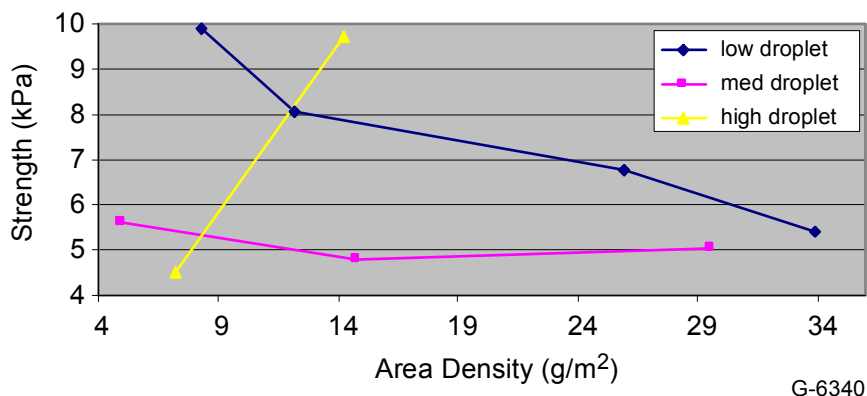


Figure 51. Coating tensile strength versus area density

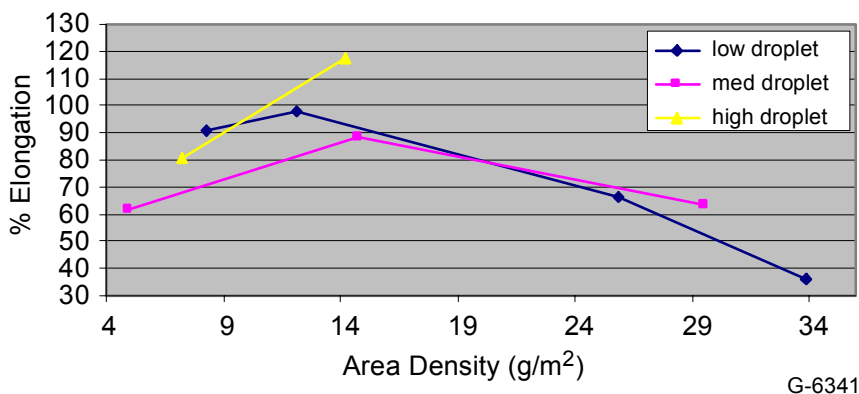


Figure 52. Percent elongation of coatings versus area density

8.8 Summary

The effects of several process variables on electrospun fiber diameter and beading were explored. It was found that:

- The nozzle diameter primarily affects the size of the beads and not the fiber diameters.
- Higher solution flow rates tend to increase the number of droplets.
- Addition of poly(aniline) doped with camphorsulfonic acid (CSA) increases the conductivity of the solution and inhibits the formation of droplets.
- The mechanical properties of electrospun membranes are strongly influenced by beading in the membrane.

These findings will help to refine the electrospinning process as we move ahead to scale up the process to coat larger areas.

9. Gas Permeation and Particle Filtration

A theoretical study was performed to better understand gas permeation and particle filtration for non woven fabrics. That study is presented below.

9.1 Gas Permeation

The gas transport through a porous medium can be described by Darcy's Law:

$$v_o = -\frac{k}{\mu} \nabla p$$

where v_o is the facial velocity, k is the fluid permeativity, μ the gas viscosity and ∇p is the pressure gradient. Davis¹ has derived for porous fibrous media an alternative form for the facial velocity given by

$$v_o = \frac{d_f^2}{\mu t f(\alpha)}$$

where t is the fabric thickness, d_f the fabric fiber diameter, $f(\alpha)$ is a function derived by Davis^{1,2} and $(1-\alpha) \equiv \epsilon$ is the fabric porosity.

An effective circular capillary pore size, D_e , can be defined using Hagen-Poiseuille flow as

$$D_e = \frac{d_f}{\left[\sqrt{2(1-\alpha)^2 \alpha^{1.5} (1+56\alpha^3)} \right]} \quad (1)$$

The net flow per fabric area, Q/A , is given by

$$Q/A = \frac{\epsilon^2 D_e^2}{32\mu} \frac{\Delta p}{t} \quad (2)$$

where Δp is the pressure drop across the fabric. This relation allows one to compute gas flow rates through a fabric with fiber diameter, d_f , as a function of fabric thickness and pressure drop across the fabric.

The effective fabric pore size is a function of fabric porosity, Figure 52 shows the ratio D_e/d_f , the ratio of the effective hydrodynamic diameter to the fiber diameter. At small values of fiber filler fraction ($1-\epsilon$), the hydrodynamic radius is substantially larger than the fiber diameter. At fill factors $> \sim 0.35$ the value of D is fairly close to the fiber diameter.

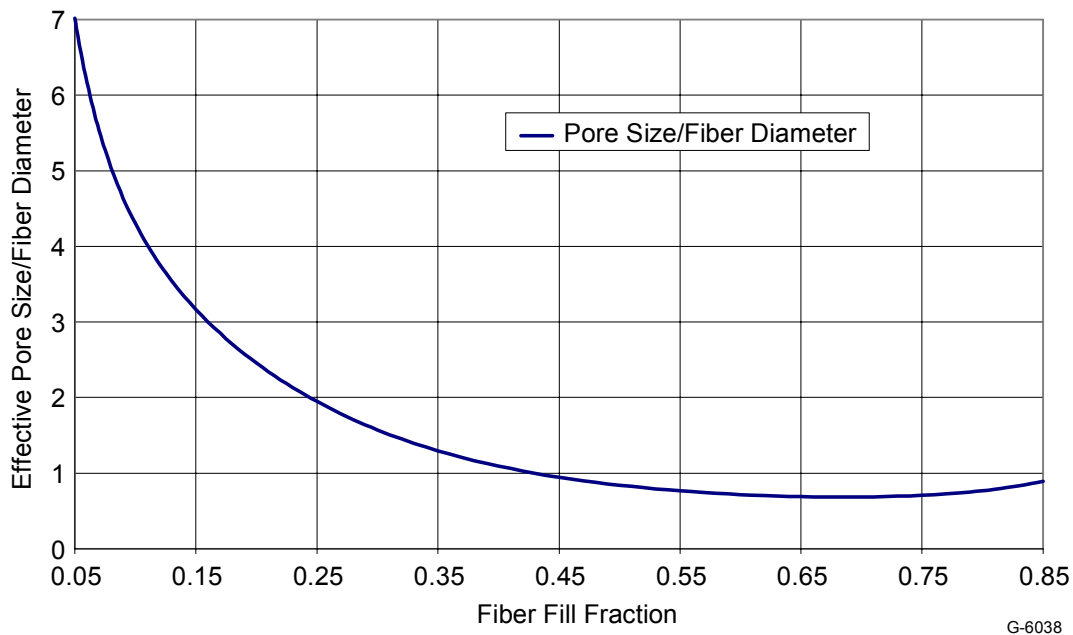


Figure 53. Ratio of effective hydrodynamic diameter to fiber diameter as a function of fiber fill fraction

The utility of these relations is that for a given fabric an effective pore diameter can be computed and used to compute the relationship between flow rate through a filter (or fabric) and the pressure drop. The pressure drop can then be used to compute energy for filtration.

9.2 Filtration Model

The filter capture efficiency, E , is given by the following equation:¹

$$E = 1 - e^{-E_s S}$$

where E_s is the single fiber capture efficiency and S is the fiber projected area which is given by the following relation:

$$S = \frac{4t\alpha}{\pi d_f}$$

where as before t is the fabric (filter) thickness, $1 - \alpha = \varepsilon$ is the fabric porosity and d_f is the fiber thickness.

The single fiber capture efficiency is written as the sum of two terms

$$E_S = E_R + E_D$$

where E_R is the capture efficiency from fiber-particle interception and E_D is the capture efficiency from diffusion.

Interception occurs when a particle following an airflow streamline transports a particle within contact range of a fiber. The particle becomes attached to the fiber. Diffusion is a removal process that dominates for particles smaller than $0.1 \mu\text{m}$ diameter. Brownian motion is significant for these particles and they randomly traverse areas much greater than their diameters moving along gas flow streamlines. Removal by diffusion depends on gas velocity. Lower velocities increase removal by diffusion.

An additional removal mechanism is impaction. Impaction occurs when the particle momentum is great enough so that the particle crosses velocity streamlines. Typically, this process is not significant for normal filter velocities and $< 10 \mu\text{m}$ particle sizes.⁴

The expression for the capture efficiency by diffusion, E_D , is given by:

$$E_D = 1.6126 \left(\frac{1 - \alpha}{F_K} \right) \text{Pe}^{-2/3}$$

where F_K is the Kuwabara hydrodynamic factor, and Pe is the Peclet number. The Peclet number is given by

$$\text{Pe} = \frac{u d_f}{D}$$

where u is the face velocity and D is the particle diffusion coefficient. the Kuwabara factor is:

$$F_K = \alpha + (\alpha^2 + 2 \ln \alpha + 3)/4$$

where (as before) α is the fiber fill fraction equal to $(1 - \varepsilon)$ where ε is the fabric porosity.

The value of E_D is proportional to $D^{2/3}$. The particle diffusion coefficient decreases rapidly as the particle size increases. This behavior is shown in Figure 53. The consequence is that diffusion removal (capture) efficiencies are small for larger particles, i.e., $d_p > 0.5 \mu\text{m}$.

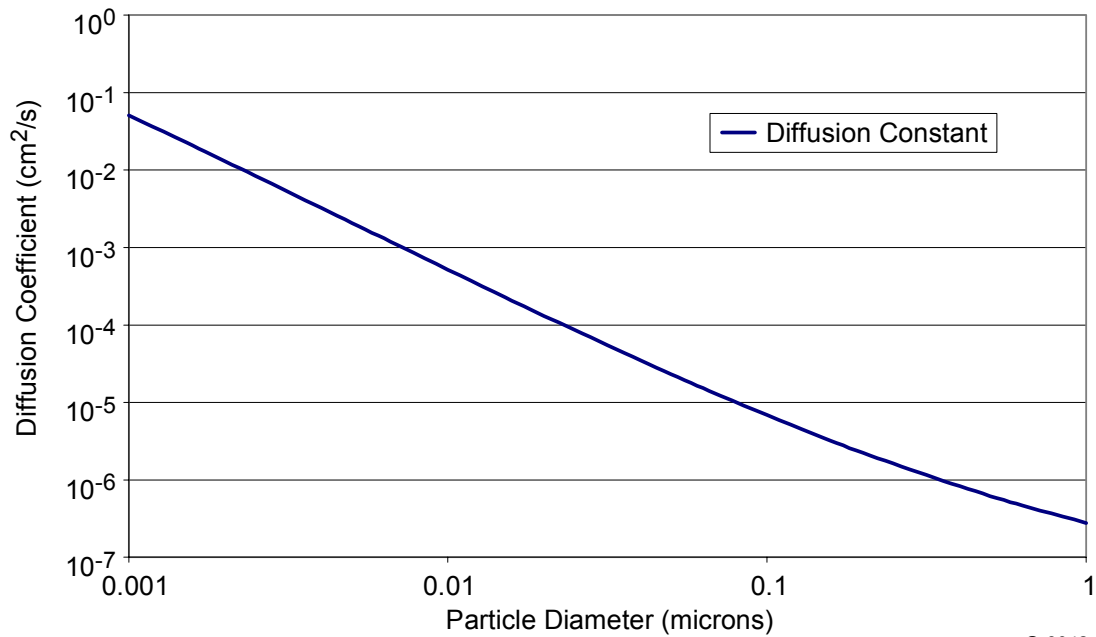


Figure 54. Diffusion coefficient as a function of particle size

The single fiber interception capture efficiency, E_R , is given by⁵

$$E_R = \frac{1}{\varepsilon} \left(\frac{1 - \alpha}{F_K} \right) \left(\frac{N_R^2}{1 + N_R} \right)$$

where ε is a numerical correction factor usually taken equal to 1.6, F_K is the Kuwabara factor, and N_R is given by

$$N_R = d_p/d_f$$

and is the ratio of particle to fiber diameters. Figure 54 (from Ref. 6) shows the single fiber capture efficiency behavior as a function of particle size. At small particle sizes ($< 0.5 \mu\text{m}$) diffusion capture dominates and at large particle sizes ($> 1 \mu\text{m}$) interception dominates. The relative capture efficiency has a minimum value in the 0.1 to 0.4 μm particle diameter range depending on fiber size, fill factor and other filter characteristics.

Calculations of penetration depths of particles were performed for filters of different fiber diameters, filter porosities, and face velocities.

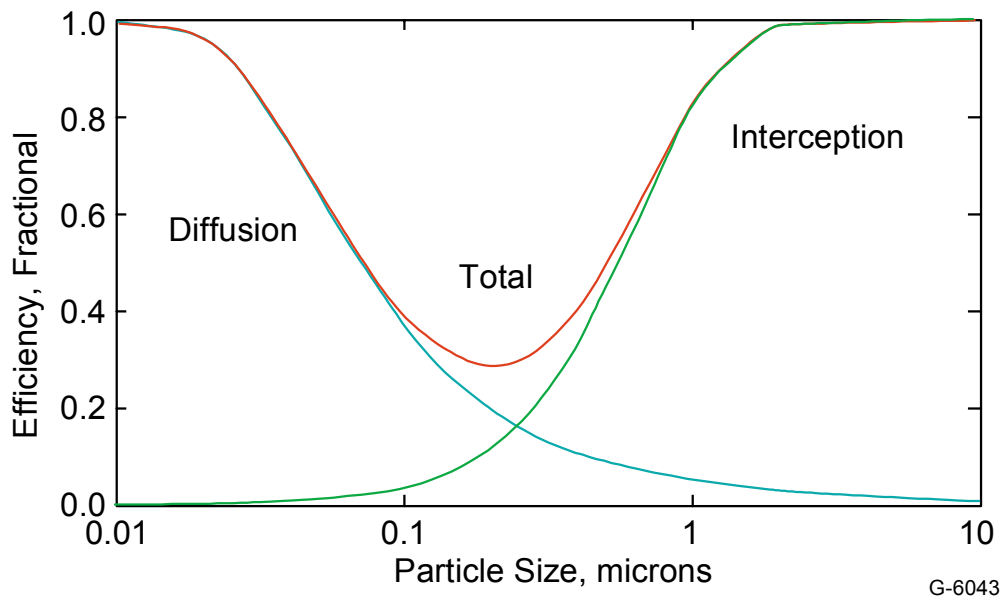


Figure 55. Generalized comparison of the contribution to total filter efficiency due to diffusion and to interception (Ref. 2)

Figure 55 shows the e-folding distance into filters containing 500 nm diameter fibers with differing porosities (or fill factors). The e-folding distance is defined as the filter thickness at which $(1 - 1/e)$ of the particles are captured. The face velocity was taken to be 1 cm/s in all cases shown here. The penetration depth is lowest for the smallest and largest particles where the capture efficiencies are largest. Decreasing the fabric porosity increases the e-folding

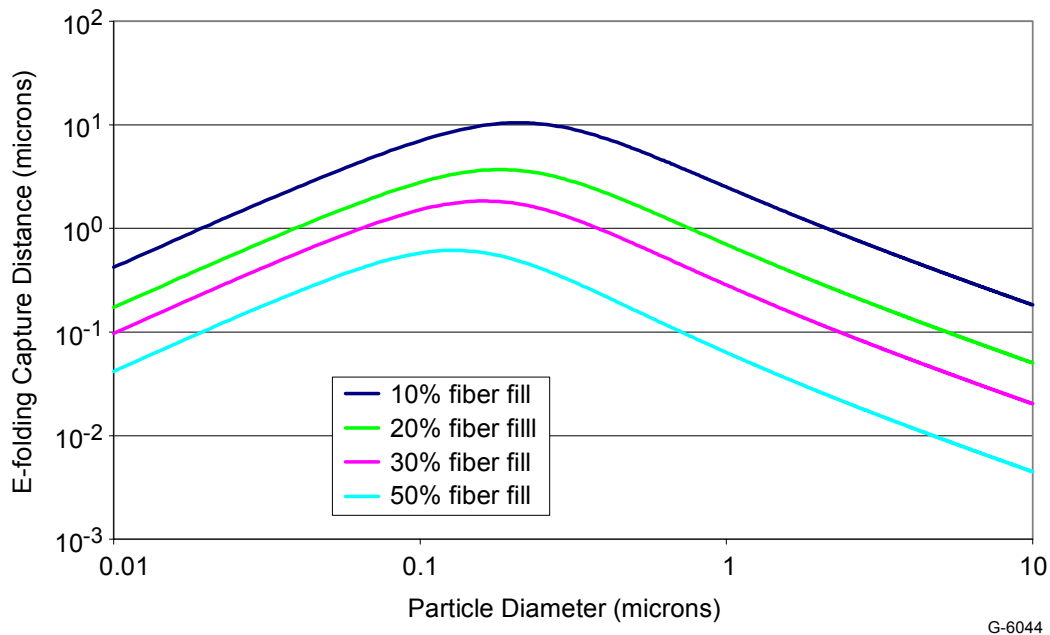


Figure 56. E-folding penetration distances into 500 nm fiber diameter filters; 1 cm/s face velocity

penetration distances. The increase is proportional to the inverse porosity so that the product of the penetration depth and porosity is approximately equal between 10 and 50% fabric porosity. The shift in the penetration depth maximum is due to the variation of the Kuwabara factor with fiber fill. The particle diameter for maximum penetration depth (or minimum capture efficiency) shifts from 0.13 μm at 50% porosity to 0.22 μm at 90% porosity.

Figure 56 shows e-folding penetration depths for filters with 500 nm fibers, 50% porosity, and varying gas face velocities. The gas face velocities vary between 1 and 100 cm/s. The diffusion capture efficiency depends on the face velocity via the Peclet number. The dependence is

$$E_D \sim v^{-2/3}$$

so that E_D decreases with higher face velocities. Consequently, the e-folding penetration distance increases at higher velocities. This is readily seen in Figure 7 for smaller sized ($< 0.1 \mu\text{m}$) particles. For larger sized particles ($\geq 0.3 \mu\text{m}$) there is no significant dependence of the penetration depth on face velocity. This is because for $> 0.3 \mu\text{m}$ particles interception capture dominates and this mechanism does not depend on face velocity.

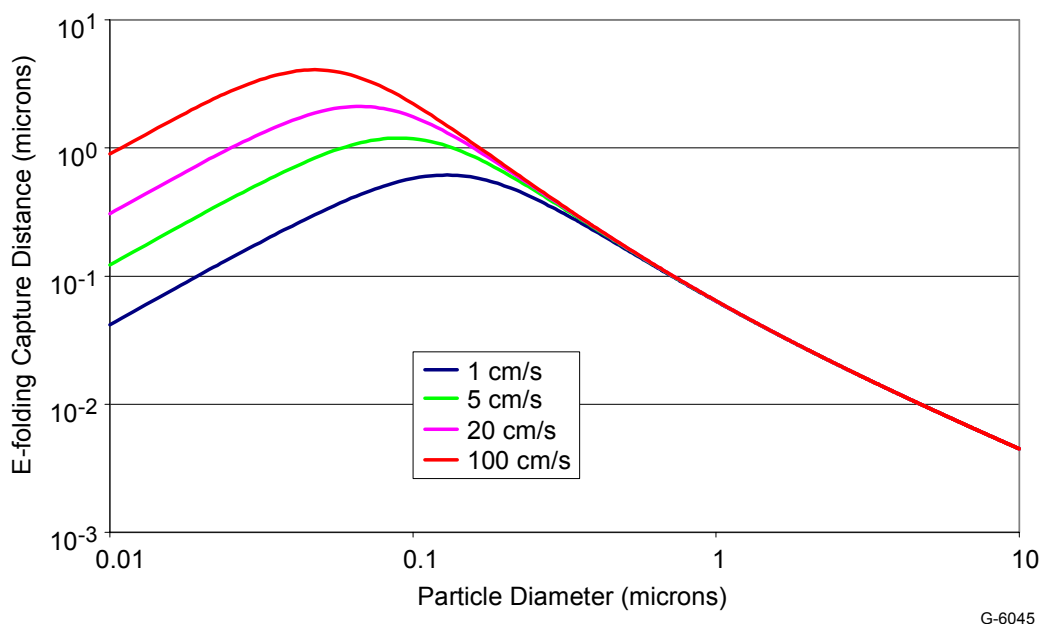


Figure 57. E-folding penetration distances into 500 nm fiber fabrics; 50% fabric porosity

Figure 57 shows the variation of e-folding penetration depth with fiber diameter for fixed fabric porosity (50%) and face velocity (1 cm/s). Two features are readily seen. The e-folding penetration distance increases rapidly as fiber diameter increases especially for larger particles which are captured according to the interception mechanism. Second, the peak in the e-folding penetration distance increases to larger particle diameters as the fiber size increases. Our primary interest is for spore-like particles with $\sim 1 \mu\text{m}$ diameters. We will first consider larger particles $d_p > 0.5 \mu\text{m}$.

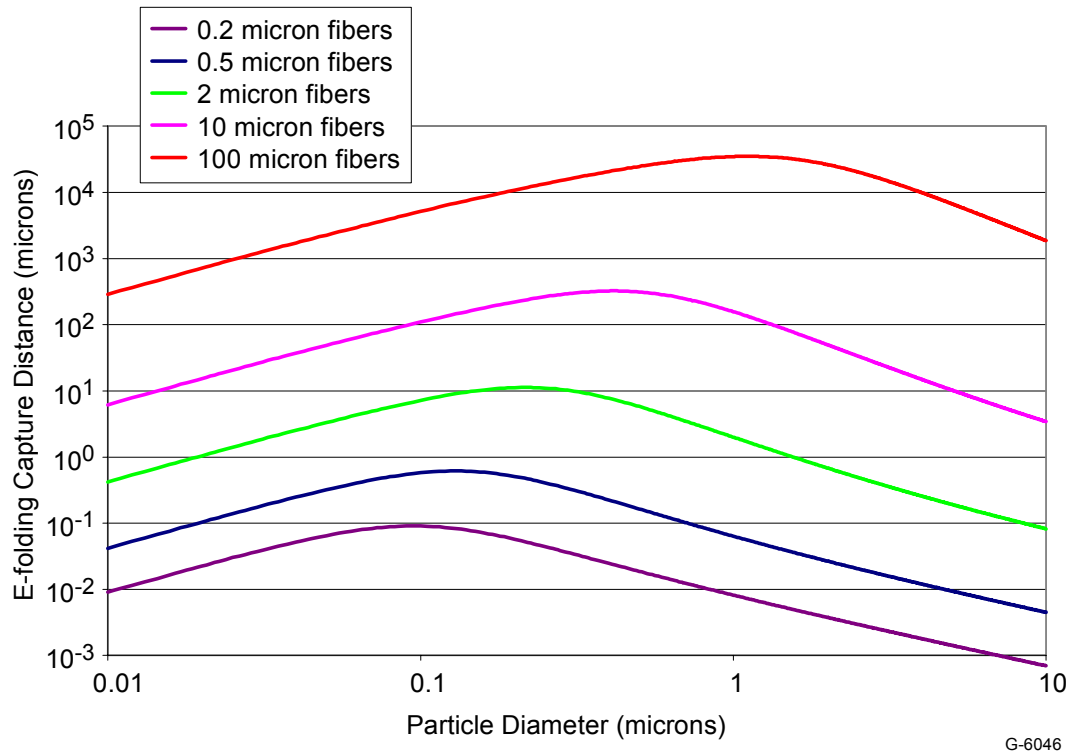


Figure 58. E-folding penetration distances in fabric; 500 nm fiber, 50% porosity

For $d_p > 0.5 \mu\text{m}$ the interception mechanism is dominant

$$E \sim E_R \sim \frac{N_R^2}{1 + N_R} = \frac{(d_p / d_f)^2}{1 + (d_p / d_f)} .$$

For thin fibers $d_p/d_f \gg 1$

$$E \sim E_R \sim d_p / d_f \sim 1 / d_f$$

so that the capture efficiency is inversely proportional to the fiber diameter. Simply put, thinner fibers are much more mass efficient for particle capture. For a $1 \mu\text{m}$ particle, the e-folding thickness of a $100 \mu\text{m}$ fiber filter is a factor of 10^6 greater than that for a $0.2 \mu\text{m}$ fiber filter. For a $0.1 \mu\text{m}$ particle the e-folding ratio is reduced to a factor of $\sim 10^5$.

For smaller particles for which diffusional capture dominates,

$$E \sim E_D \sim d_f^{-2/3}$$

and capture efficiency increases, albeit more slowly, as fiber diameter decreases.

Figure 58 shows the filter thickness required to capture 99.99% of particles of a varying sizes. Such high capture efficiencies are required to filter bioagents. The 99.99% penetration distances are the filter thicknesses required to remove 99.99% of a given size particle. A filter to remove a 1 μm particle, approximately the size of an anthrax spore, made from 100 μm fibers must be about 10 cm thick. An equivalent filter of made from 0.2 micron fibers will be about 0.1 μm thick. Of additional significance is that the smaller fiber filters will have lower pressure drops across their filter beds.

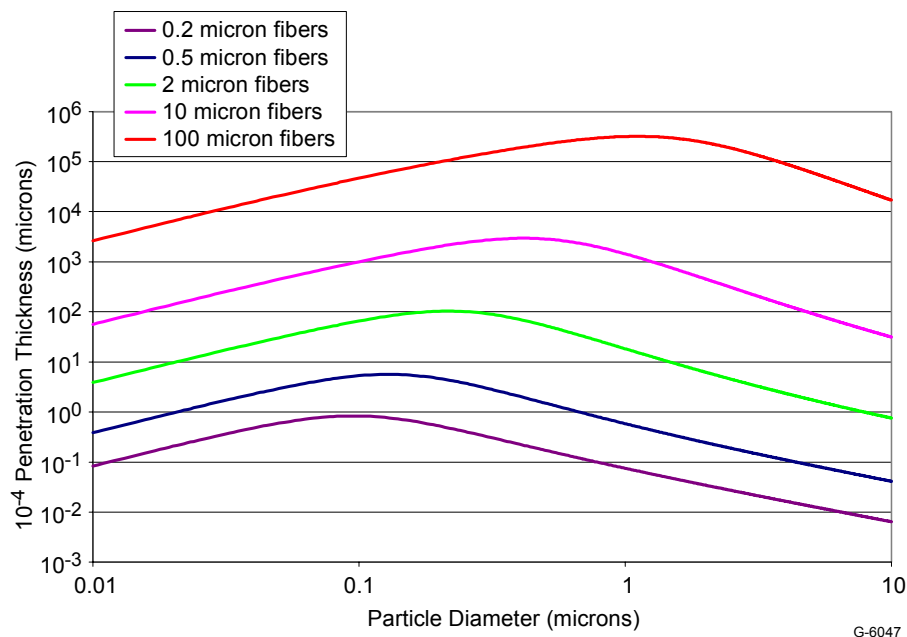


Figure 59. 99.99% capture penetration depths; 50% porosity, 1 cm/s face velocity for varying particle diameters

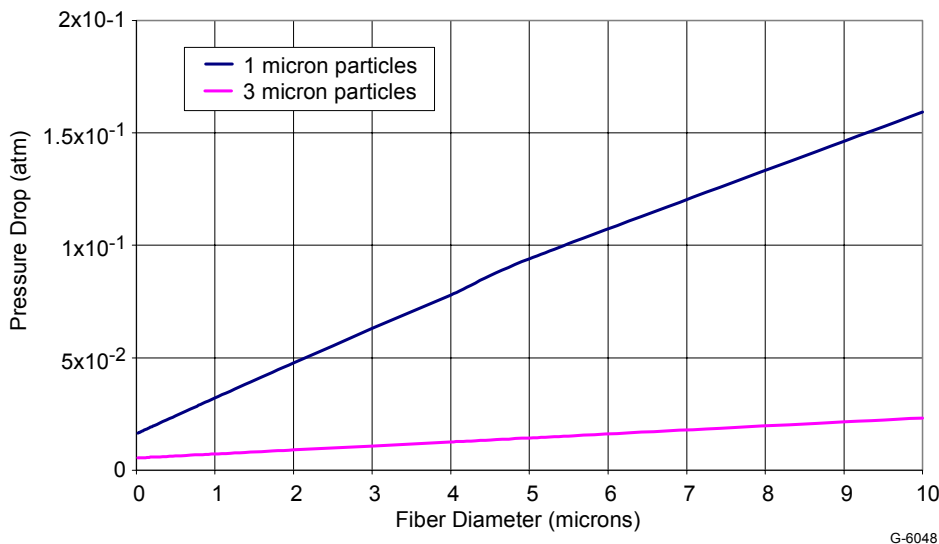


Figure 60. Pressure drop across filter bed of varying fiber diameters. Gas velocity = 10 cm/s, 80% porosity and filters are designed to remove 99.99% of 1 or 3 micron particles

Figure 59 shows the computed pressure drop across filter beds designed to remove 99.99% of 1 and 3 μm particles. The calculations are shown for varying fiber diameter. The filter bed has 80% porosity and the flow rate through the filter bed is 10 cm/s. The pressure drop to remove a 1 micron particle from a 0.2 μm fiber diameter filter is 0.019 atm whereas from a 2 μm filter bed the pressure drop is 0.048 atm, approximately a factor of three more. The pressure drop across a filter made of 10 micron fibers is 0.16 atm, almost an order of magnitude higher than for the 0.2 μm fiber filter. To remove 99.99% of 3 μm particles, the pressure drop is 0.006 atm across a 0.2 μm fiber diameter and 0.009 atm across a 2 μm fiber diameter filter.

The energy requirements to drive these filters can be computed from the pdV work required to provide the necessary pressure gradient. We assume the system is isothermal.

Figure 60 shows the energy/volume required to remove 99.99% of 1 micron particle through filters as a function of filter fiber size. Increasing from 0.1 to 5.0 μm increases the processing energy a factor of 5. Nano fibers ($< 0.1 \mu\text{m}$) clearly reduce filtration energy requirements.

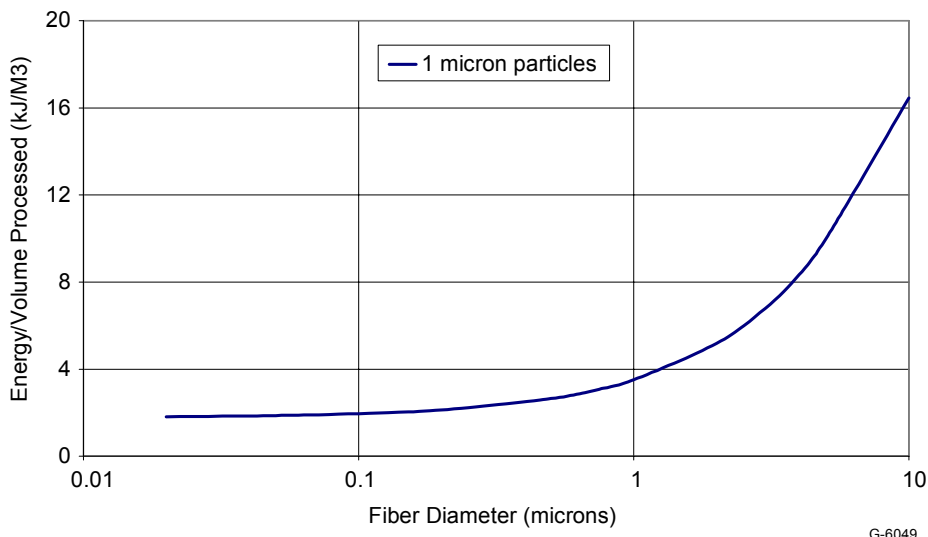


Figure 61. Energy required to transport gas across filters of varying fiber sizes: 10 cm/s velocity, 80% porosity, and 99.99% removal of 1 micron particles.

Figure 61 shows the computed pressure drop across a filter bed with 50% porosity designed to remove 99.99% of 1 and 3 μm particles. The gas velocity equals 10 cm/s. The behavior is similar to that shown in Figure 59. Filters with smaller fibers have significantly lower pressure drops. Pressure drops are larger for higher porosity. Figure 62 shows the pressure drop across a 50% porosity filter for 99.99% removal of 1 and 3 μm particles. In this case the gas velocity equals 100 cm/s. The variation of the pressure drop as a function of fiber size is similar to the cases shown in Figures 59, 61, and 62. However the magnitude of the pressure drop is an order of magnitude greater in this case because of the higher velocity.

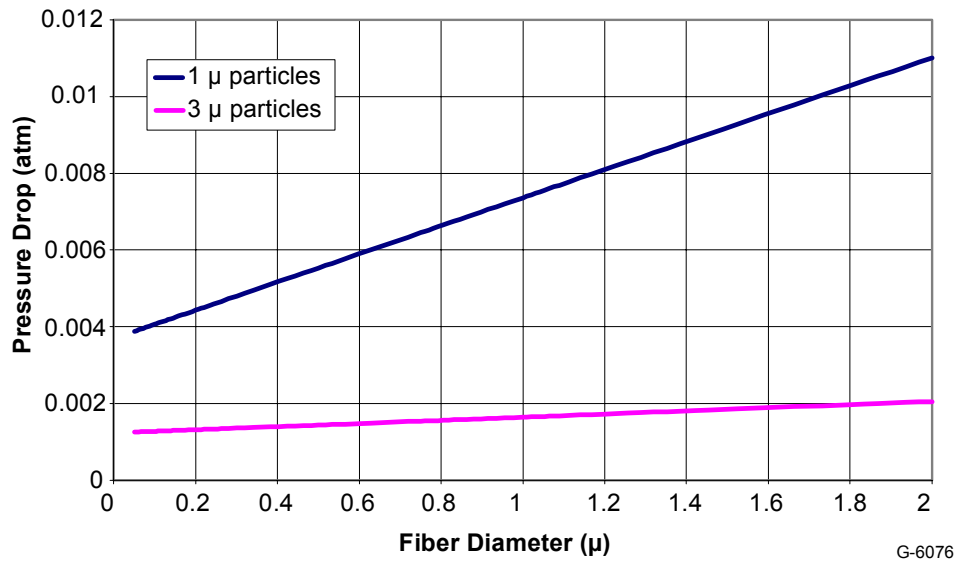


Figure 62. Pressure drop across filter beds of varying fiber diameters. Gas velocity = 10 cm/s, 50% porosity and filters are designed to remove 99.99% of 1 or 3 μ m particles

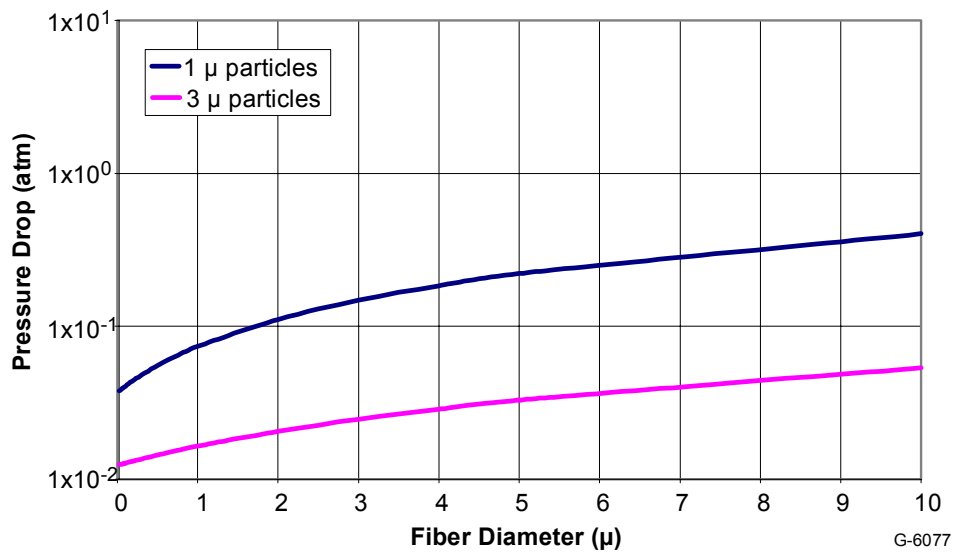


Figure 63. Pressure drop across filter beds of varying fiber diameters. Gas velocity = 100 cm/s, 50% porosity and filters are designed to remove 99.99% of 1 or 3 μ m particles

Figure 63 and 64 show the energy/volume required to remove 99.99% of 1 μ m particles from 50% porosity filters at flow velocities of 10 and 100 cm/s respectively. The qualitative behavior is similar at both velocities. Energy/volume increases as fiber size increases. However, the energy/volume increases by at least an order of magnitude as the gas velocity increases an order of magnitude from 10 to 100 cm/s. Comparison with Figure 60 shows that decreasing the porosity from 80% to 50% reduces the process energy by about a factor of four.

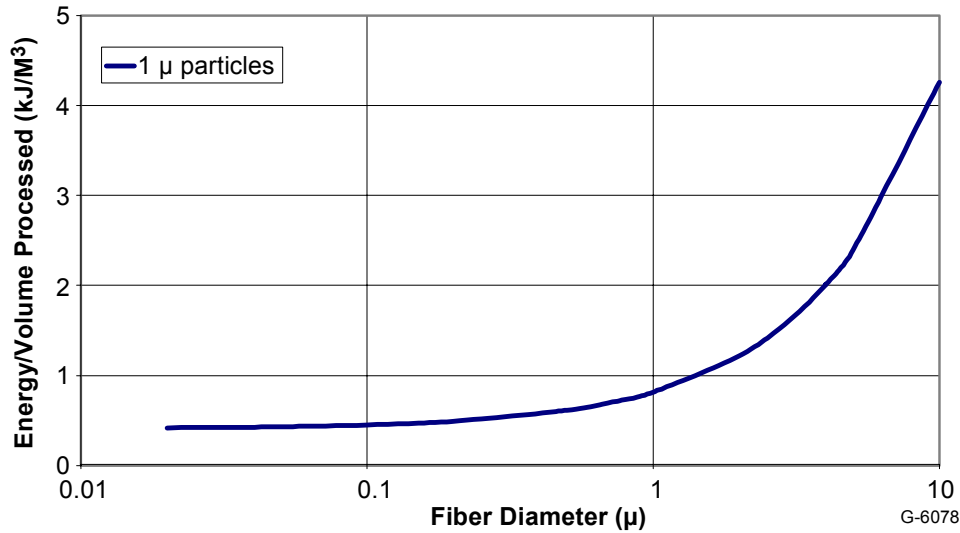


Figure 64. Energy required to transport gas across filters of varying fiber sizes, 10 cm/s velocity, 50% porosity and 99.99% removal of 1 μ m particles

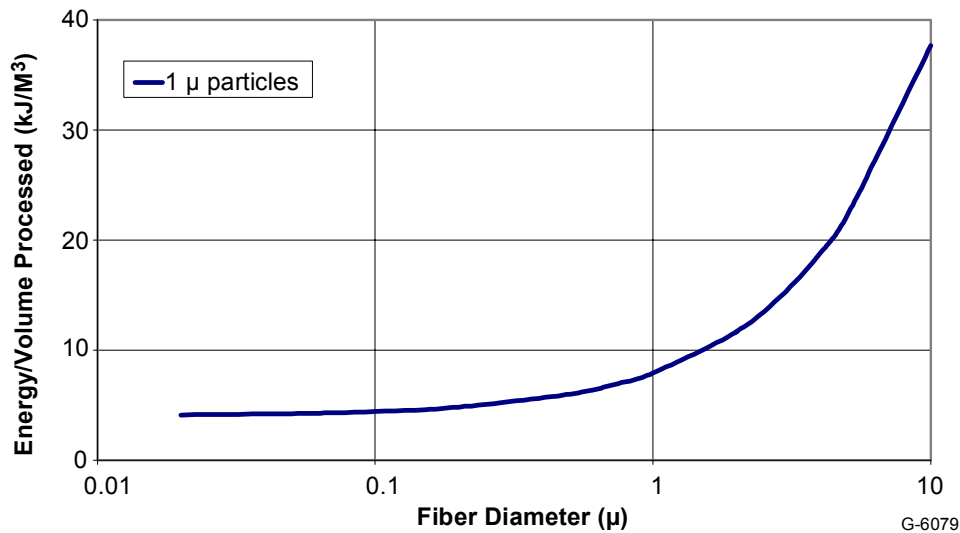


Figure 65. Energy required to transport gas across filters of varying fiber sizes, 100 cm/s velocity, 50% porosity and 99.99% removal of 1 μ m particles

9.3 Summary

The effects of fiber size and membrane porosity on gas permeation and particle filtration have been modeled. These have allowed us to calculate membrane thicknesses required to achieve any desired capture efficiency given known fiber diameters and membrane porosity. These models also allow predictions of pressure drop across the membrane for a given fiber size. As we move into filtration efficiency testing, these models will allow us to relate results with predictions.

10. Filtration Efficiency Testing

To determine the filtration efficiency of an electrospun membrane, we devised an apparatus which allowed for the entrainment of polystyrene latex spheres (Polysciences, Inc.) into a gas stream which flowed through the electrospun membrane, or test filter. Particles passed by the test filter were collected on a second, cellulose nitrate, filter, or collection filter. For improved detection, fluorescent polystyrene latex spheres were used, and observation of particles on the collection filter was performed using a fluorescence microscope.

10.1 Experimental Apparatus

The entrainment of particles is performed using a Collison nebulizer (BGI, Inc.), shown in Figure 65. The details of nebulizer operation are described in May [7]. A dilute suspension of fluorescent polystyrene spheres is placed inside the nebulizer and upon the application of sufficient gas pressure to the gas inlet nebulization occurs. Nebulization forms a very narrow size distribution of 2 micron diameter water droplets, some of which will contain particles; this is controlled by the particle concentration of the suspension. Our tests used 1 micron YG spheres and we were able to determine a concentration where few to no occurrences of multiple particles per droplet were observed. These droplets evaporate prior to reaching the test filter which enables a stream of dry entrained particles. The glass jar holding the particle suspension is typically placed in an ice water bath during operation to minimize evaporation (non-droplet water loss).

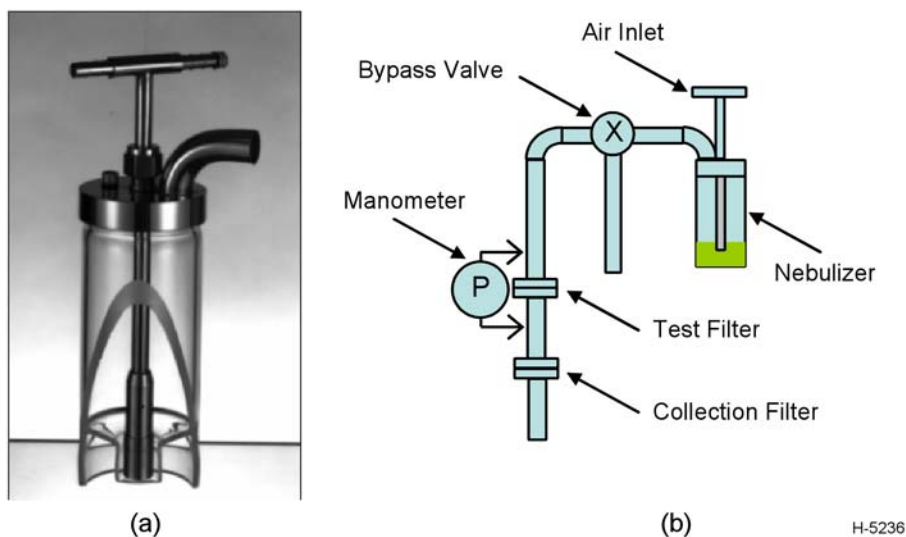


Figure 66. a) Cutaway view of a Collison nebulizer from BGI, b) Schematic of apparatus

20 PSI of clean, dry, air was used to operate the nebulizer and the volumetric flow speed of the gas was measured using a mass flow meter. The test filter was supported in QF-40 flanges. The pressure drop across the test filter was measured using a manometer with sub-in H_2O resolution (Dwyer Mark II). Commercially available 0.45 micron pore size cellulose nitrate filters were used as collection filters and were analyzed using a Leica DM IRB fluorescence

microscope. A bypass valve is placed just after the nebulizer exit which allows the gas/particle flow to bypass the test filter at startup, thus avoiding the effects of any startup transients. The collection filter is a 0.45 micron cellulose nitrate filter held in a commercially available polypropylene filter holder with a 1/4" NPT fitting.

10.2 Device Operation

The theoretical particle flux delivered by the apparatus described above can be calculated from the concentration of particles in solution and the rate of droplets exiting the nebulizer. This second value is an experimentally determined value of 5.25×10^9 droplets/minute and is calculated by periodically weighing the nebulizer (containing water only) for some set of conditions and determining the mass delivery rate attributable to water droplets. Some of the water loss will be in the form of evaporation of water vapor and some in the form of water droplets. May gives an approximate value of 1/3 of the mass delivery being in the form of droplets [7].

10.2.1 Droplet Rate

We measured this mass delivery rate at 6.4 liters/minute of clean, dry air at 20 PSIG at the nebulizer using all three nebulizer jets and with only a single jet producing droplets (but the unused two still allowing air flow to maintain the flow rate). The three-jet case delivers 9.04 g/hour of water. Using May's estimate of 1/3 of this mass being droplets, and assuming a monodisperse distribution of 2 micron diameters, the droplet delivery rate should be approximately 1.2×10^{10} droplets/minute for all three jets, or 4×10^9 droplets/minute/jet.

We then blocked the water intake of two nebulizer jets; this stops their droplet formation but allows air to pass. To a first approximation the same amount of evaporation should take place in this scenario, and the only change should be from eliminating droplet formation from two nozzles. In this case, 6.41 g/hour of water are delivered. The difference between the three-jet and the single-jet should be the contribution from the two blocked nozzles which should be entirely in droplet form. Therefore, the mass delivered in droplets for each nozzle should be $(9.04 \text{ g/hour} - 6.41 \text{ g/hour})/2 = 1.32 \text{ g/hour/jet}$ which equals 5.25×10^9 droplets/min/jet. This is slightly more than what was predicted using May's approximation, but remains in good agreement with predictions.

10.2.2 Particle Entrainment

We purchased a suspension of 1-micron diameter polystyrene-latex spheres from Polysciences with a reported concentration is 4.55×10^{10} particles/ml. We sought to determine the number of particles that would be in each droplet in order to dilute the initial particle suspension to minimize multiple particles per droplet. The number of droplets per particle as a function of dilution volume ratio is plotted in Figure 66a. The particle delivery rate for a nebulizer operating with only a single jet at 6.4 L/min is calculated by dividing the droplet rate above (5.25×10^9 droplets/min) by the number of droplets per particle, and appears in Figure 66b. A dilution ratio of 1:1000 (1 ml of suspension diluted to 1000 ml total volume) gives 1 particle for every 5240 droplets exiting the nebulizer for a rate of 9.95×10^5 particles per minute.

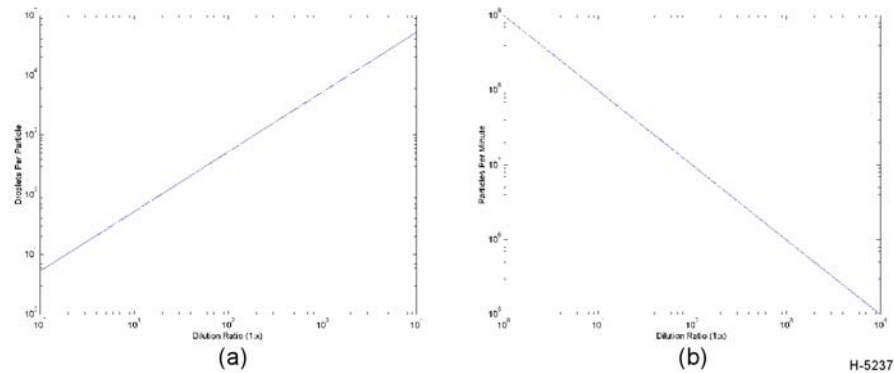


Figure 67. a) Droplets per particle vs. particle dilution.
b) Particles per minute vs. particle dilution

We investigated the presence of multiple particles per droplet by performing very short (10 second) tests with the system (Figure 65b) using dilutions of 1:200, 1:1000, and 1:2500 of the Polysciences suspension. No test filter was used, and the collection filter was analyzed using a fluorescence microscope at 50x magnification. Four images were collected: one in the center of each filter and one in each quadrant. The images were analyzed using software which returned a fit of the size of each particle. Histograms of these data appear in Figure 67. These data support the selection of a 1:1000 dilution ratio for filtration testing purposes

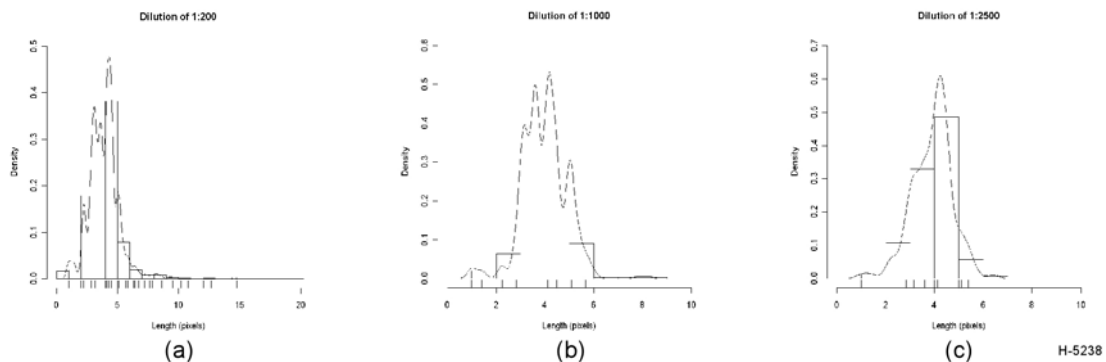


Figure 68. Histograms of “object size” on collection filter to look for the presence of multiple particles per droplet. A 1 micron particle is approximately four pixels in diameter.
a) 1:200 dilution. b) 1:1000 dilution. c) 1:2500 dilution

From Figure 66b we make the observation that the particle density should follow a $1/x$ relationship with the dilution ratio. Figure 68 plots the log of the particle density found on the images of the collection filters versus the log of the dilution. This fitted line has a slope of -1.2 which is close to the expected slope of -1 and our assumptions of the operation of our particle entrainment apparatus appear to be largely correct.

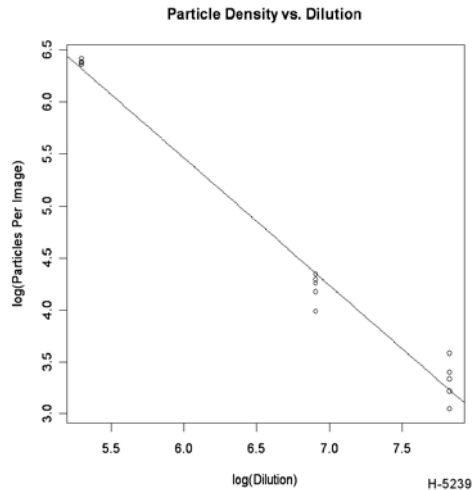


Figure 69. Plot of the log of the observed particle density vs. the log of the dilution ratio showing the linear fit with slope of -1.2. The theoretical slope for this plot is -1

10.2.3 Actual Particle Delivery Rate

We determine the actual particle delivery rate by operating the apparatus for longer times with no test filter in place and more extensively characterizing the collection filter. We selected the 1:1000 dilution ratio and operate for 60 seconds. The particles are collected on a 4.2 cm diameter portion of a 4.7 cm diameter filter and are analyzed at 100x in the fluorescence microscope having a CCD camera which captures a 1.48 mm^2 image at this magnification. Each collection filter is sampled in the center (5x), at $r = R/2$ (8x), and at $r = R$ (8x). These data are then mathematically fit and integrated to determine a total number of particles.

Figure 69 shows the areal density of particles for this test and a corresponding visualization of the areal particle density. The Gaussian profile is likely due to the flow restriction in the plumbing of the collection filter holder. Integration of this profile results in a total particle count of $6.47 \times 10^5 + 1.32 \times 10^5 - 1.31 \times 10^5$ particles. This is approximately 65% of the value predicted above. This is likely attributable to the actual particle concentration in the Polysciences suspension being lower than claimed as a result of particle aggregation and flocculation as the apparatus is sealed and the pore size of the collection filter is smaller than the particles used in the test.

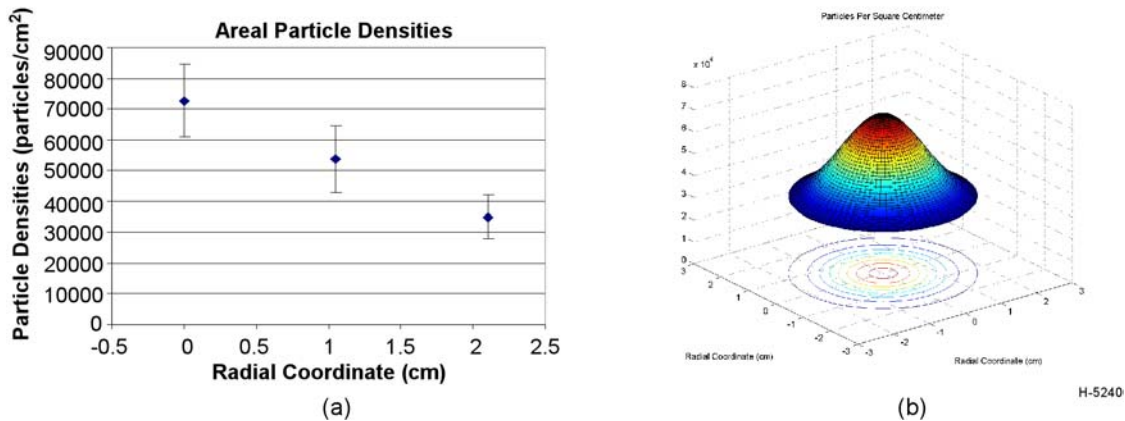


Figure 70. a) Areal particle density of particles on the collection filter and b) a surface view of the Gaussian fit to the mean data

10.3 Filtration Efficiency Testing

Using the apparatus described above and the 1:1000 dilution of 1 micron spheres suspension, we evaluated the filtration efficiency of electrospun membranes spun onto fabric substrates. The fabric/membrane filter was clamped between QF40 flanges supported by a centering ring, which ensured a seal. The inside of the flange where the centering ring is seated was coated with a silicone caulk to ensure a seal between the fabric and the caulk. Electrospun membranes were spun directly onto the fabric (no adhesive) from a 15 wt % solution of Noveon Estane 58245 in 1:1 DMF and CH_2Cl_2 at 4 ml/hour, 20 kV, and with the nozzle 26 cm from the substrate. Filtration efficiency tests were performed for one minute using 1 micron particles at 6.4 L/min of gas flow with one nebulizer jet operating, and the nebulizer suspension cooled to < 1.5 Celcius as before.

10.3.1 Fabric Substrate

We selected a 100% cotton camouflage material as the fabric substrate. Six samples of this material were subjected to testing to evaluate its filtration efficiency. The collection filters for all samples were tested as above and similar analysis performed to calculate the number of particles transmitted, from which the filtration efficiency was calculated. Figure 70 shows a 50x fluorescence microscope image of the front and back of the fabric after testing.

Figure 71 shows the areal density of particles on the collection filter after the fabric. The total number of particles on the filter were $4.79 \times 10^5 + 7.78 \times 10^4 - 8.52 \times 10^4$ for an average filtration efficiency of 26.08%.

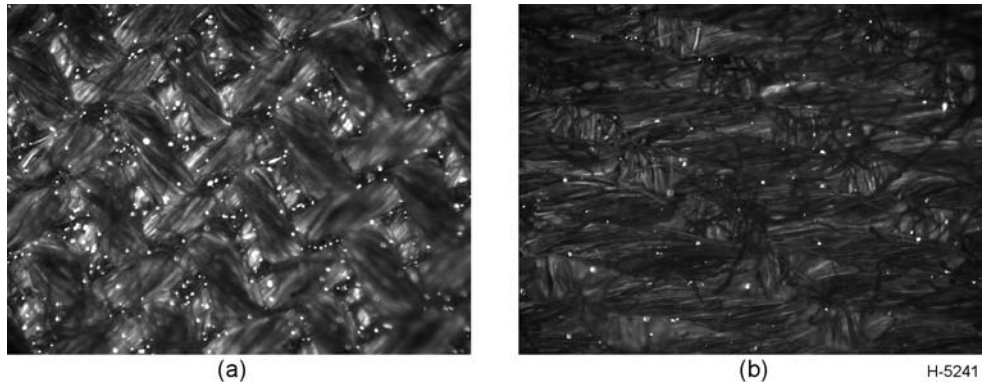


Figure 71. Fluorescence microscope images of a) the front (incident) and b) the back of the fabric after testing

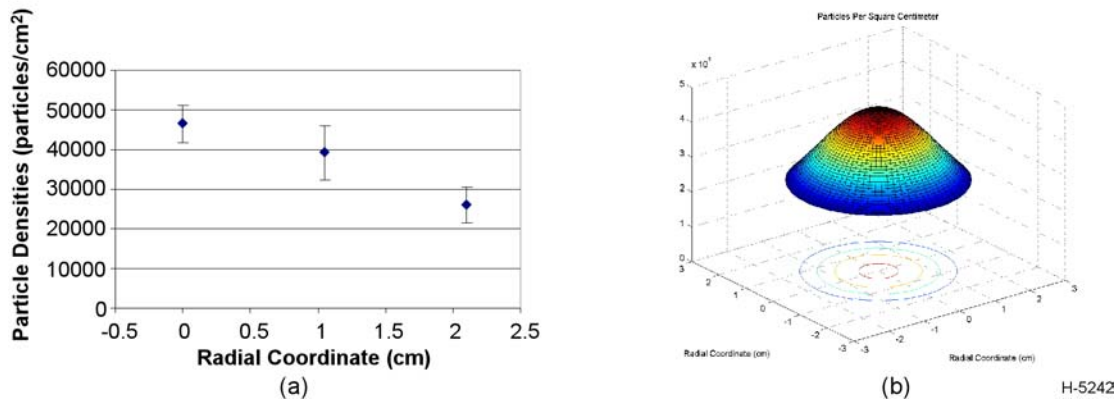


Figure 72. a) Areal particle density of particles on the collection filter and b) a surface view of the Gaussian fit to the mean data

10.3.2 Electrospun Films

Estane membranes were electrospun onto fabric as described above without the need for an adhesive layer. Three samples were created where only the length of the deposition was varied. These were 5, 10, and 20 minute depositions. Each of these was tested as described previously. Figure 72 shows a 500x SEM image and a 50x fluorescence microscope image of an electrospun membrane after filtration testing. The SEM image clearly shows the coexistence of 0.5 and 2-5 micron diameter fibers.

The transmitted particle densities found on the capture filters are plotted in Figure 73. Surface views of Gaussian fits to the mean values are shown in Figure 74. The filtration efficiency results are summarized in Table 10.

The 5 and 10 minute deposition samples each resulted in a 2 order of magnitude reduction in transmitted particles, as seen in Figure 73. The interpretation of the 20 minute sample should be only considered preliminary as only three particles were actually found on the collection filter. In order to get more meaningful test results, we will have to test for longer times.

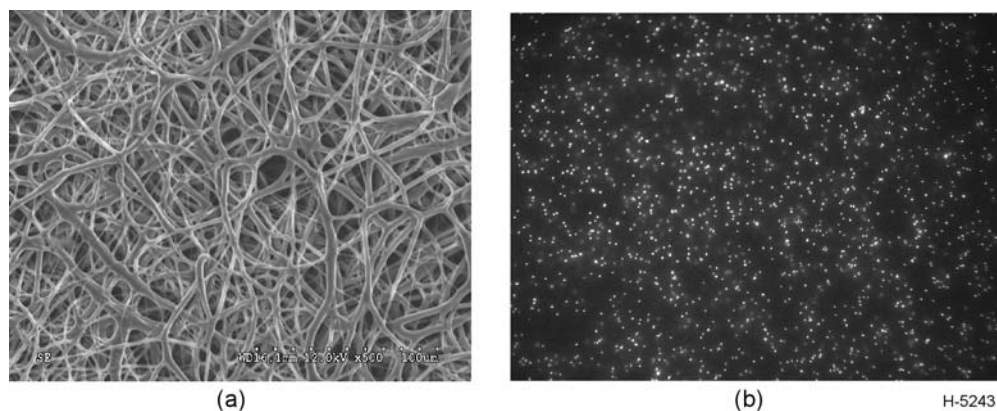


Figure 73. Images of electrospun Estane films after filtration testing. a) 500x SEM image and b) 50x fluorescence microscope image

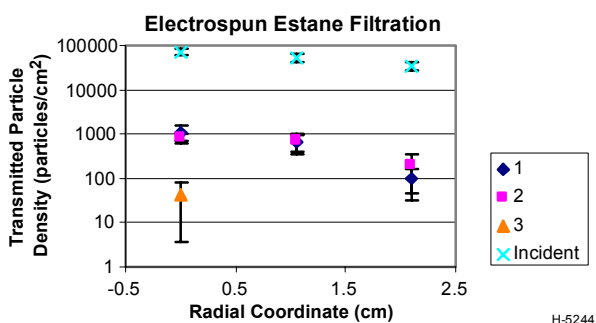


Figure 74. Areal particle density of particles on the collection filter for the three electrospun filters tested

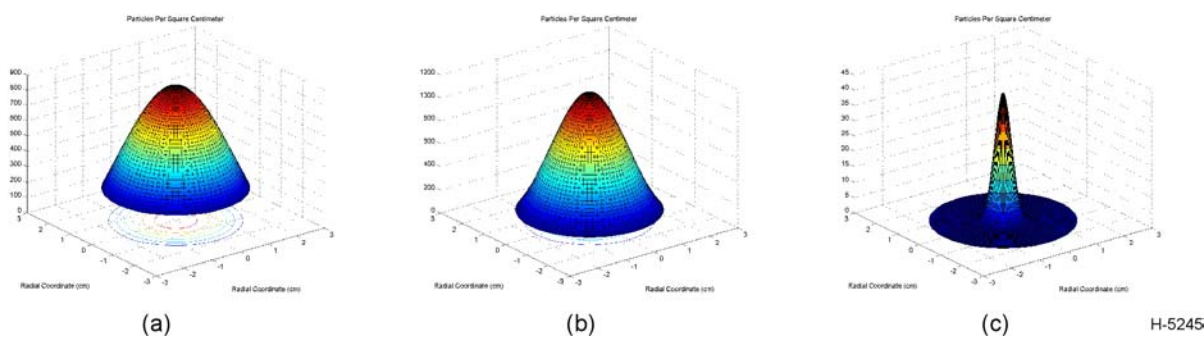


Figure 75. Surface plots of Gaussian fits to the mean values for a) 5 min deposition, b) 10 min deposition, and c) 20 min deposition electrospun samples

Table 10. Summary of Electrospun Estane Membrane Filtration Efficiency Results

Deposition Time (min)	Transmitted Particles			Filtration Efficiency		
	mean	mean + σ	mean - σ	mean	mean + σ	mean - σ
5	6974	10220	3366	98.54%	97.86%	99.30%
10	6358	9051	3671	98.67%	98.11%	99.23%
20	15	29	1	99.997%	99.994%	99.9997%

10.4 Summary

An apparatus for filtration efficiency testing of electrospun membrane filters was devised, modeled, and built using a Collison nebulizer to entrain 1 micron polystyrene-latex spheres. Particles not trapped by the membrane filter under test were collected using a conventional 0.45 micron pore size cellulose nitrate membrane filter which was analyzed using fluorescence microscopy. Electrospun Estane membranes were tested and shown to be upwards of 98.5% efficient against 1 micron spheres. Longer test times will be needed to accurately test the more efficient thicker filters.

11. **References**

1. Davis, C.N., Air Filtration (Academic Press, London, 1973).
2. Tsai, P.P., "Theoretical and Experimental Investigation on the Relationship Between the Nonwoven Structure and the Web Properties," *Int. J. Nonwovens*, Winter 2002, 33 (2002).
3. Brown, R.C., Air Filtration (Pergamon Press, London, 1993).
4. Brown, R.C. and Wake, D., "Air Filtration by Interception - Theory and Experiment," *J. Aerosol Sci.*, 22, 181 (1991).
5. Liu, B.Y.H. and Rubow, K.L., Air Filtration by Porous Media, "Fluid Filtration: Gas," (ASTM, Philadelphia, 1986).
6. Kowalski, W.J., Bahnfleth, W.P., and Whittam, T.S., "Filtration of Airborne Microorganisms: Modeling and Prediction," *ASHRAE Trans.*, 105, 4 (1999).
7. May, K.R., "The Collison Nebulizer. Description, Performance & Application," *J. of Aerosol Science*, 4(3), 235 (1973).

This document reports research undertaken at the US Army Natick Soldier Research, Development and Engineering Center, Natick, MA, and has been assigned No. NATICK/TR-12/011 in a series of reports approved for publication.